Christer Honoré Ersland

Atomistic modeling of failure in iron

Thesis for the degree of Philosophiae Doctor

Trondheim, April 2012

Norwegian University of Science and Technology
Faculty of Engineering Science and Technology
Department of Engineering Design and Materials

NTNU – Trondheim
Norwegian University of
Science and Technology

NTNU
Norwegian University of Science and Technology

Thesis for the degree of Philosophiae Doctor

Faculty of Engineering Science and Technology
Department of Engineering Design and Materials

ISBN 978-82-471-3541-9 (printed ver.)
ISBN 978-82-471-3542-6 (electronic ver.)
ISSN 1503-8181

Doctoral theses at NTNU, 2012:129

Printed by NTNU-trykk

Abstract

This thesis is based on three research papers, all concerning molecular dynamics (MD) simulations of failure properties in pure iron. The first two papers examine iron crystals with cracks deformed in Mode I tensile testing, with different geometrical constraints. In Paper I we have reviewed fracture mechanics in light of atomistic simulations, and shown a possible way to link atomistic and multiscale simulations of cracks to the crack initiation toughness of the material. Stress-intensity factors and effective surface energies were calculated from atomistic penny-shaped cracks and multiscale edge crack simulations. The influence of T-stress/constraint level was examined.

Paper II is devoted to the study of penny-shaped cracks, comparing this geometry with the more commonly studied through-thickness cracks. It was found that the fracture mechanisms in specific crystallographic orientations were similar, but that the penny-shaped crack was able to change shape during loading in order to favor dislocation emission over unstable fracture.

The last paper, Paper III, is a study of size and strain rate effects in compression of nanopillars, where three crystallographic orientations were simulated. A size-strengthening effect was found for pillars compressed along $\langle 100 \rangle$ and $\langle 110 \rangle$ directions, and a lower strain rate was shown to result in lower maximal stress before deformation began.

Preface

This thesis is submitted as part of the requirement for the degree Philosophiae Doctor at the Norwegian University of Science and Technology (NTNU). The study has been performed at the Department of Engineering Design and Materials, where my supervisor has been Professor Christian Thaulow.

The study was done in the period from October 2008 to March 2012, which includes seven months of teaching duty in the course Atomistic Modeling of Materials Failure, as well as courses amounting to a workload of one full semester. The study was funded by the Research Council of Norway ("Arctic Materials" project supported through the Petromaks programme, contract no. 187389/S30) and the industry companies ENI, Statoil, Total, JFE Steel, Nippon Steel Corporation, Miras Grotnes, Scana Steel Stavanger, Brück Pipeconnections, Trelleborg, Bredero Shaw, Aker Solutions, Technip and GE Oil and Gas.

Parts of this work has been done in collaboration with my co-supervisor Dr. Erling Østby from Sintef Materials & Chemistry and with PhD candidate Inga Ringdalen Vatne, who are also co-authors of some of the papers presented in this thesis. My simulations have been run on the high-performance computing (HPC) facilities at NTNU funded through the Notur project.

During the work on this thesis I have had the chance to attend three conferences where I have presented parts of my work: the 18th European Conference on Fracture (ECF) in Dresden, Germany (2010); the Fifth International Conference on Multiscale Materials Modeling (MMM) in Freiburg, Germany (2010); and the Twenty-first International Offshore and Polar Engineering (ISOPE) Conference, Hawaii, USA (2011). I have been fortunate enough to visit Prof. Diana Farkas at Virginia Tech twice, in addition to meeting with Prof. Markus J. Buehler from MIT on several occasions.

In the first part of this thesis an overview of the field, some theoretical background and motivation for the work is given. The second part contains the main results of this research, presented through the three papers I have taken part in during my PhD work.

Christer Honoré Ersland

Trondheim, March 2012

List of papers

Paper I

C. H. Ersland, C. Thaulow, I. R. Vatne, and E. Østby

Atomistic modeling of micromechanisms and T-stress effects in fracture of iron

Engineering Fracture Mechanics, **79**, 180-190 (2012) [1]

In this paper we explore a possible method to couple atomistic modeling of initiation of fracture in iron with displacement constraints taken from continuum considerations. Molecular dynamics is used to examine the effect of a penny-shaped crack, and the quasicontinuum method is used as a platform for performing multiscale analysis. The modified boundary layer approach enables us to examine the influence of constraint (geometry, crack size and mode of loading) on the fracture mechanisms by changing the T-stress (the constant term in the stress series expansion). The results are discussed in relation to how constraint influences upon the crack initiation toughness.

Paper II

C. H. Ersland, I. R. Vatne, and C. Thaulow

Atomistic modeling of penny-shaped and through-thickness cracks in bcc iron

Submitted to Modelling and Simulation in Materials Science and Engineering [2]

Atomistic simulations of penny-shaped embedded cracks in bcc iron are performed using molecular dynamics. The results reveal that the original circular crack geometry can change shape gradually upon loading, depending on the crystallographic orientation. This new geometry generally favors emission of dislocation loops instead of unstable fracture. Comparison is made between through-thickness cracks in six different orientations and penny-shaped cracks on the same crack planes. We find that changes in crack shape and the interaction of events in different directions play an important part in how fracture mechanisms evolve when cracks in full 3D simulations extend, and that dislocation emission and mechanical twins ”win” over unstable crack-growth by bond-breaking.

Paper III

C. H. Ersland and C. Thaulow

Modeling of size and strain rate effects in compression tests of iron nanopillars

Submitted to Computational Materials Science [3]

The size and strain rate effect on the deformation behavior of defect-free bcc-Fe nanopillars is investigated through molecular dynamics simulations. Three crystallographic orientations, four pillar sizes and two strain rates have been simulated in displacement-controlled compression. It is found that deformation mechanisms and stress – strain behavior is highly dependent on the crystallographic orientation of the single crystal. For (100) and (110) pillar orientations there is a clear size-strengthening effect found to be caused by a lack of space to emit dislocations inside the pillars, while for a (111) orientation the effect is less profound. Lower strain rates are found to result in lower stresses and strains before deformation begins.

My contribution to the papers

In Paper I [1] I contributed with the section on simulations of a penny-shaped crack, where I performed all simulations, analysis and writing. I also took active part in producing text and figures in most parts of the paper.

In Papers II and III [2, 3] I contributed substantially to all parts of the papers. I made and performed all simulations, analyzed a majority of the results, made all figures and wrote most of the text.

Contents

Chapter 1

Introduction

Steel is certainly the one of the most widely used structural materials in the world, and with an abundance of existing steels this type of alloy is used in everything from buildings to pipelines. As a first step in order to understand the properties of steel we have focused on pure iron, in order to gain fundamental insight. The ability to withstand large loads and deformations is one of the main benefits of using iron and steels, and the various alloys have yield stress values ranging from typically around 100 MPa (cast iron) up to 700 MPa (high-strength steel).

All real materials have imperfections, and microcracks will always be present within structures. This is not a problem as long as these cracks remain small and the material is not critically loaded. However, if the cracks are loaded beyond a certain level or reach a critical size, they might suddenly grow uncontrollably and cause catastrophic failure of the structure. It is necessary to know when and how this happens, in order to utilize materials in safe and cost-effective ways.

In traditional fracture mechanics research, many continuum equations are used and vast amounts of simulations are done using finite element modeling (FEM). With these approaches, the *process zone* immediately surrounding the crack tip is treated more or less like a "black box" where a certain behavior is assumed. This region contains such high stresses and complicated processes that regular fracture mechanics breaks down, and this is where atomistic modeling can shine a light in the dark. By explicitly considering all atoms around a crack, fracture criteria and mechanisms can be studied and quantified.

When going to such small scales as the atomistic level, the precise lattice structure, crystallographic orientation and crack shape is very clearly visible and will influence the behavior during mechanical loading. These are parameters we have explored extensively in this thesis, and we have thus chosen a "bottom-up" approach: To start studying fundamental, nanoscale properties in order to understand macroscopic effects.

As nanotechnology advances, new equipment and test methods make it possible to access material properties at scales never seen before. The smallest samples tested nowadays are less than 100 nm, and they start approaching the sizes we can simulate atomistically. Local material testing within single grains and with specific crystallographic orientations can be done in the lab, with

conditions ever closer to the "perfect" world of the atomistic modeling. This type of testing is simulated in this thesis.

Outline

In addition to the three research papers found at the end of this thesis, some introductory chapters are included. Chapter 2 gives a more general introduction to iron, the lattice structure, defects and dislocations, while Chapter 3 explains some basic concepts and practical limitations of molecular dynamics (MD) simulations. In Chapter 4 (Paper I and II [1, 2]) and Chapter 5 (Paper III [3]) a motivation for the papers and an outline of the research is given.

Acknowledgements are found in the last chapter of this thesis.

Chapter 2

Material properties and defects

This chapter acts as a brief introduction to some of the properties of iron, bcc structures, defects and dislocation mechanisms, in order to set the stage for the research presented in the papers.

2.1 Iron and the bcc structure

Iron is a material that has been used for several thousand years, and is known as a strong metal with good deformation and alloying properties. The yield stress for high-purity iron has been measured by e.g. Kuramoto et al. [4], which resulted in values in the range of $350 - 425$ MPa at a temperature of 4.2 K.

Metals have their atoms arranged in periodic lattice structures, and iron is of the *body-centered cubic* (bcc) type, shown schematically in Figure 2.1. The strength of a perfect iron crystal will be highly dependent on the crystallographic direction along which one deforms the material, and $\langle 100 \rangle$ directions are found to be the weakest. Clatterbuck et al. [5] performed ab initio calculations to find the *ideal strength* of pure iron, in tension and in shear. The ideal strength is an upper bound to the material strength, and can be calculated by looking at elastic instability in the lattice structure. Uniaxial tension in a $\langle 100 \rangle$ direction resulted in a stress – strain curve with maximum stress of 12.6 GPa at 15% strain. The point of maximum stress was at the elastic instability associated with the bcc $\rightarrow$ fcc (Bain) deformation path and corresponds, physically, to cleavage along a $\{001\}$ plane.

Morris et al. [6] described mechanical behavior of bcc metals in a defect-free world, i.e. with a pure, dislocation-free iron crystal. They cited *ab initio* calculations giving an ideal tensile strength of about 10.5 GPa for pure iron, which is $0.08E_{100}$, where E_{100} is the elastic modulus in the $\langle 100 \rangle$ direction. At a strain of 0.26 along the $\langle 100 \rangle$ direction a bcc cell is transformed into an fcc cell, which corresponds to the above stress if we fit the stress – strain curve with a sinusoid.

Mechanical loading of an iron crystal may result in *brittle fracture*, limited crack growth and/or plastic deformation through emission of *dislocations* (further described in Section 2.3). This will

depend on many factors: Crystallographic orientation of the sample, the mode of loading, strain rate and temperature, to mention some.

As shown in Figure 2.1, the bcc crystal has some preferred cleavage planes and slip systems. Slip in bcc occurs in $\langle 111 \rangle$ directions, which are the closest packed, and the most common slip planes are $\{110\}$, $\{112\}$ and $\{123\}$ [7]. The above slip systems are also found experimentally to be the most active in pure iron and low-alloy steels [8,9]. It is shown experimentally that $\{100\}$ planes are the most likely to cleave, but $\{110\}$, $\{112\}$ and $\{123\}$ planes may also produce cracks [10].

One can theoretically estimate which planes should be the favored cleavage planes in bcc, due to the ranking of surface energies. It is found that it is the $\{110\}$, $\{100\}$ and $\{112\}$ planes [11].

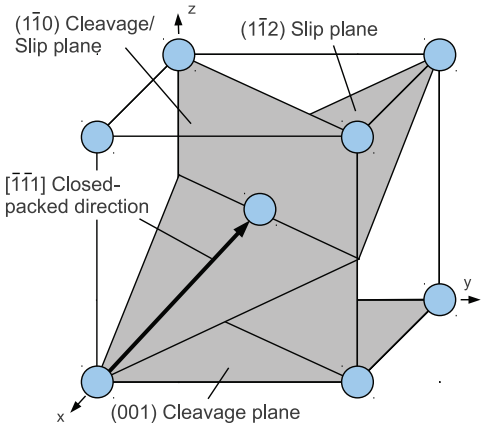

Figure 2.1: Sketch of a bcc crystal, with some possible slip and cleavage planes marked. Figure made by Inga Vatne, used with permission.

2.2 Ductile – brittle transition

Iron and ferritic steels can have a dramatic change in fracture toughness over a small temperature range. At low temperatures the steel is brittle, and fails by fracture. At high temperatures the material is ductile and tears by microvoid coalescence. In the temperature range of the transition both mechanisms are present, and in experiments data will be very scattered in this region. This transition is well described in e.g. the textbook by Anderson [12], and is also introduced in Paper I [1].

The work presented in this thesis only simulate iron at very low temperatures ($1 - 5$ K), so we do not consider the transition between brittle and ductile behavior. We do, however, seek to

investigate brittle behavior in iron, and the conditions that promote or hinder uncontrollable crack growth.

2.3 Defects in iron

Real crystalline materials always contain defects of some kind, which might alter their properties. This includes point defects, line defects, planar defects and bulk defects. Point defects (e.g. vacancies, interstitials and impurities) and bulk defects (e.g. voids and precipitates) have not been topics in our research, and will not be described further. We will instead focus on some defects that have been of major importance in our papers, namely dislocations, twinning and phase transitions. For further reading, the book by Hull and Bacon [13] is suggested.

Dislocations are line defects in a crystalline material at the atomistic level, and they lead to the plastic deformation of metals on the macroscopic level. The two main types of dislocations are *edge* and *screw*, and they are both shown schematically in Figure 2.2.

An important concept when describing dislocations is the Burgers vector **b**, which describes the direction and magnitude of the lattice distortion. This can be found in the following way: First, draw a rectangle in the perfect lattice without the dislocation, encompassing the site where the dislocation will be. Then, introduce the dislocation, something which will make the rectangle change (and normally break one of the sides, leaving it an open geometrical structure). The Burgers vector is then the line segment that will join the rectangle again. As seen in Figure 2.2, an edge dislocation has a Burgers vector perpendicular to the dislocation line, while in the screw dislocation they are parallel.

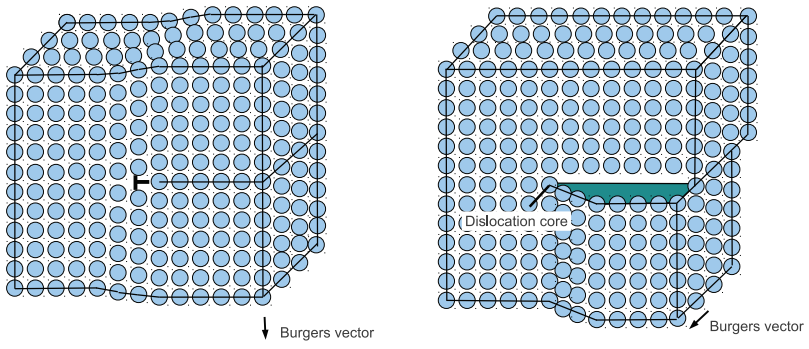

(a) Edge dislocation. (b) Screw dislocation

Figure 2.2: Sketches of edge and screw dislocations in a material, and their Burgers vectors. Figures made by Inga Vatne, used with permission.

Caillard [14–16] investigated the kinetics of dislocations in pure iron by performing TEM in situ straining experiments at temperatures of 110 K, 300 K and in the range between. The main result from [14] is that at 300 K, screw dislocations move steadily, with a velocity depending on their length. This is in accordance with the *kink-pair* mechanism, which is characteristic for bcc metals, where pairs of kinks are formed on the dislocation line, causing it to glide. At a temperature of 110 K, however, the screw dislocations have a "jerky" motion, with quick jumps over several tens of nanometers separated by locked positions that lasts for seconds. This behavior is inconsistent with the kink-pair mechanism, and the author suggests a *locking-unlocking* mechanism which was previously observed in Ti.

In bcc materials dislocation motion is particularly complicated, due to the likelihood of *cross-slip*. As mentioned in Section 2.1, dislocations move in $\langle 111 \rangle$ directions, with slip planes being $\{110\}$, $\{112\}$ and $\{123\}$. In particular, three $\{110\}$, three $\{112\}$ and six $\{123\}$ planes share the same $\langle 111 \rangle$ direction, which makes it easy for screw dislocations to move around on different planes in a very ill-defined manner.

Twinning is a planar defect, and is a process where a region of a lattice locally changes orientation, mirrored over a *twin plane*, due to shear strain. This is shown schematically in Figure 2.3. In bcc metals, twinning happens on the $\{112\}$ planes by twinning dislocations with Burgers vector $\mathbf{b} = 1/6\langle 111 \rangle$, and there is an increased tendency for twinning to occur with increasing deformation rate and decreasing temperature (see e.g [13]). We thus expect to observe twinning in our simulations, since we have very low temperatures and a very high strain rate.

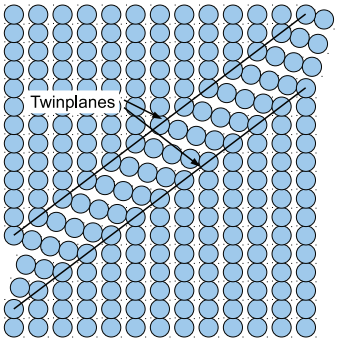

Figure 2.3: Sketch of twinning in a crystal, where a region changes orientation mirrored over a twin plane. Figure made by Inga Vatne, used with permission.

Before ending this chapter we should also mention *phase transformation* from bcc to face-centered cubic (fcc) structure in iron, that might occur in small or large regions at high stresses both in simulations [17–19] and experiments [20,21]. Different types of orientation relationships between the bcc and the fcc structure exist [22–25], but we will not elaborate on this here.

Chapter 3

Modeling and simulation

My contributions to the research presented in Papers I - III are based on molecular dynamics (MD) simulations, and a significant part of my thesis work was spent making, running and analyzing these simulations. It thus seems natural to include this chapter concerning some of the fundamentals of MD simulations, as well as a brief overview of how they are analyzed. The software used for all MD simulations was the Large-scale Atomic/Molecular Massively Parallel Simulator (LAMMPS) [26], a free, open-source code developed and distributed by Sandia National Laboratories, USA. For details regarding this code, the reader is referred to the LAMMPS homepage, `http://lammps.sandia.gov/`.

3.1 Molecular dynamics in a nutshell

The basic idea of MD simulations can be explained in one sentence: **It is a dynamical evolution of a system of atoms by explicitly solving Newton's second equation of motion for all atoms in small, discrete timesteps.** Let us quickly go through how this could be done in practice.

From a system of N atoms with positions $\vec{r}(t)$ and velocities $\vec{v}(t)$ we can find the positions a time Δt later by the Taylor expansion

$$\vec{r}(t+\Delta t) = \vec{r}(t) + \vec{v}(t)\Delta t + \frac{\vec{a}(t)}{2}\Delta t^2 + \frac{\dot{\vec{a}}(t)}{6}\Delta t^3 + \mathcal{O}(\Delta t^4), \tag{3.1}$$

where $\vec{a}(t)$ is the acceleration and $\dot{\vec{a}}(t)$ is the third-order time derivative of the positions. By also performing a Taylor expansion for the previous timestep $t - \Delta t$ and adding the expressions, we can find the future positions as

$$\vec{r}(t+\Delta t) = 2\vec{r}(t) - \vec{r}(t-\Delta t) + \vec{a}(t)\Delta t^2 + \mathcal{O}(\Delta t^4).$$

Dropping the $\mathcal{O}(\Delta t^4)$-term and by the use of Newton's second law $\vec{F}(t) = m\vec{a}(t)$, we can estimate the future postition (with an error of Δt^4) by

$$\vec{r}(t + \Delta t) \approx 2\vec{r}(t) - \vec{r}(t - \Delta t) + \frac{\vec{F}(t)}{m}\Delta t^2, \tag{3.2}$$

where m is the mass of the particle considered. This is the Verlet algorithm [27], and although it is very simple it usually gives the most accurate and stable particle trajectories (see the text book by Frenkel and Smit [28] for an extended discussion regarding stability and reversibility for various algorithms).

A somewhat newer and nowadays more commonly used algorithm is the *velocity Verlet algorithm* [29], which estimates the next position directly from the Taylor expansion, as

$$\vec{r}(t + \Delta t) \approx \vec{r}(t) + \vec{v}(t)\Delta t + \frac{\vec{F}(t)}{2m}\Delta t^2, \tag{3.3}$$

and the velocity for the next timestep is calculated the following way:

$$\vec{v}(t + \Delta t) \approx \vec{v}(t) + \frac{\vec{F}(t + \Delta t) + \vec{F}(t)}{2m}\Delta t \tag{3.4}$$

It can be shown (see e.g. Frenkel and Smit [28]) that using (3.3) and (3.4) is mathematically equivalent to using the original Verlet expression (3.2), but numerically the velocity Verlet algorithm is superior on a computer of finite precision.

In the expressions above the timestep Δt is prominent, and the size of this needs to be chosen carefully. The time resolution must capture the smallest dynamics of the simulated system, which is the atomic vibrations. We thus use timesteps in the femtosecond (10^{-15} s) range, normally between $1 - 2$ fs for simulations of solids. Smaller timesteps could of course be used, but this would require many more timesteps to be run in order to follow the system during a certain real time-period. However, if the timesteps get too large, the simulations will become unstable and unreliable, so there is always a trade-off between computational cost and reliability.

System temperature and pressure

The particle velocities are connected to the temperature through the equipartition theorem, which for N particles of equal mass $m = 1$ reads

$$E_k = \frac{1}{2}m\sum_{i=1}^{N}\vec{v}_i^2 = \frac{1}{2}\sum_{i=1}^{N}(v_{x,i}^2 + v_{y,i}^2 + v_{z,i}^2) = \frac{1}{2}k_B T N_f,$$

where k_B is the Boltzmann constant, T is the temperature and $N_f = 3N - 3 \approx 3N$ is the number of degrees of freedom for a system of N ($\gg 1$) particles with fixed total momentum. We can thus easily find the instantaneous temperature as

$$T = \frac{1}{3Nk_B}\sum_{i=1}^{N}\vec{v}_i^2. \tag{3.5}$$

The system pressure can be calculated through similar expressions, summing up contributions from pairs of atoms.

What we normally want to do is to put certain constraints on our system consisting of N atoms, in order to keep volume (V), pressure (P) or temperature (T) constant during simulation. Depending on which property we wish to keep fixed, this corresponds to either a canonical (NVT) ensemble, or a constant temperature constant pressure (NPT) ensemble. Equations in order to achieve this in a simulation were developed by Nosé [30] and Hoover [31] in the eighties, and has been further improved since then. Today, the equations for evolving a system of atoms in a NVT or NPT regime within LAMMPS come from Shinoda et al. [32], which build upon work by, *inter alia*, Parrinello and Rahman [33].

3.2 Interatomic potentials

A crucial part of moving an atomic system to the next timestep is knowing the forces $\vec{F}(t)$, which are used in expressions (3.3) and (3.4). To find the force that is applied to an atom from another atom, we take the negative gradient of the *potential function*, $\vec{F}(r,t) = -\nabla V(r,t)$. This function (also sometimes called the *force field*) is what describes the interaction between two atoms of specific types, and will to a large degree determine how realistic the simulation results will be.

There are many classes of potential functions to choose from, depending on the type of system one want to simulate, and we will in the following sections present two formulations used in our research.

3.2.1 Embedded atom method (EAM)

This type of semi-empirical potential, made by Daw and Baskes [34, 35], is particularly suited for simulations of metals, as it views atoms as impurities embedded in a "cloud" of the electron densities from the other atoms. It is able to capture relaxation and material response in the case of free surfaces and cracks. In this formalism, the potential function V of the system is a sum over all individual contributions $V_{\alpha,i}$, and the atom types (for example Fe or C) are denoted by indices α and β. One sum is over the embedding functions F_α, which are dependent on local electron densities $\bar{\rho}_i$ of the surrounding atoms. The other sum is over pair-interactions $\phi_{\beta\alpha}$ which are different functions for different combinations of α and β, and they depend only on the interatomic distance r_{ij} between atoms i and j. The full expression reads

$$V = \sum_i V_{\alpha,i} = \sum_i F_\alpha(\bar{\rho}_i) + \frac{1}{2}\sum_{i,j} \phi_{\beta\alpha}(r_{ij}), \tag{3.6}$$

where the density is expressed as

$$\bar{\rho}_i = \sum_j \rho_\alpha(r_{ij})$$

in the regular EAM.

3.2.2 Analytic bond-order potential (BOP)

This potential was originally constructed by Tersoff [36], and further developed by, among others, Albe et al. [37]. Compared to the EAM potential, the *directional bonding* is what makes this potential special. An angular term determines bond strength dependent on the neighbors of an atom, and this enables the BOP to describe several bonding states, and to a certain degree chemical bonding. The potential function V for the system is written as a sum over individual bond energies in the following way:

$$V = \sum_{i<j} f_{ij}^c(r_{ij}) \left[\phi_{ij}^R(r_{ij}) - B_{ij}\phi_{ij}^A(r_{ij})\right] \tag{3.7}$$

Here ϕ^R and ϕ^A are repulsive and attractive pair-potentials, respectively. Their interaction range is controlled by the cut-off function f^c, and the *angularity and three-body contributions* are given by B_{ij}.

3.2.3 Potentials for iron

Most published iron and iron alloy potentials are of an EAM-type [38–47], but several bond-order potentials also exist [48–50]. The EAM potentials are normally preferred because they are significantly less computational intensive and give good correspondence to real materials. In cases where very high accuracy is needed, or special cases like magnetism, phase transitions or high-temperature conditions, the BOP are needed.

Several of the above iron potentials [38–40,48] were used in qualitative fracture simulations in one of our conference papers [51], and for most crack orientations very little difference was observed. Other papers (e.g. [52, 53]) also explore the influence of potentials.

In Papers I, II and III the so-called "Mendelev II" potential from [38] is used. This potential is one of the few known to correctly predict the sixfold symmetry of screw dislocation cores, as calculated by DFT calculations [54, 55], so we chose it since (both edge and screw) dislocations were expected to be of importance in our simulations. In one of our conference papers [56] a BOP by Müller et al. [48] was used to study semi-infinite cracks, since we simulated smaller systems that could afford using a more computationally intensive potential.

3.3 Limitations in both time and space

As mentioned in Section 3.1 we need to compute all forces for all atoms in our system, and it must be done in timesteps in the order of femtoseconds. These requirements severely limits the time window available for simulation, and the size of our simulated systems. Most of the MD simulations presented in Papers I – III last only a fraction of a nanosecond and have sizes ranging from $5 - 60$ nanometers.

These limitations give simulation conditions far from lab experiments, but the gap between these two worlds becomes smaller each year. In the labs at NTNU nanopillar compression experiments are now done with sizes down to a few hundred nanometers[1], and in recent literature samples smaller than 100 nm are used for material property testing [57]. Faster supercomputers and more efficient codes, combined with the development of more sophisticated lab equipment, might soon close the size gap.

The time domain is where the big gap lies, with a factor of about 10^9 difference in strain rates. Our "slowest" MD simulations have strain rates of about 10^6 (most of them use 10^8), while most experiments use $10^{-3} - 10^{-1}$. From both simulations and experiments we know that many material properties are strain rate dependent (see e.g. [3, 58–61]), but we expect MD simulations to at least qualitatively present a realistic picture of material behavior and the effect of crystallographic orientations, geometries and sizes.

3.4 Analysis tools

As an MD simulation is running, huge data files with atom coordinates and properties are produced. In order to make sense of these data, several tools are used. Most important of all to us is the Open Visualization Tool (OVITO) [62], an open-source, free visualization software made by Alexander Stukowski. Within OVITO large files can be visualized, and multiple selections can be added and deleted in order to study specific parameters of the simulations.

One of the most important tools for characterizing the deformation and fracture mechanisms in simulations is the common neighbor analysis (CNA) [63,64], which analyses the atomic structure and identifies a number of different lattice structure types. This enables us to closely study dislocation movement in our systems, and also detect lattice transformations and twinning. Another way to see dislocations is to remove all atoms below a certain value of potential energy. This will leave only free surfaces, dislocations and other highly stressed regions (for instance in front of a crack-tip), but will not provide us the detailed lattice structure information that CNA does. Examples of images produced by using CNA and by selecting atoms according to potential energy are shown in Figure 3.1.

In addition to the methods mentioned above, the Dislocation Extraction Algorithm (DXA) made by Stukowski and Albe [65] has been used on some simulations in order to better analyze dislocations. This algorithm is able to detect dislocations in a lattice, turn them into line segments and further determine their Burgers vectors.

[1] These are ongoing experiments, and are not yet published.

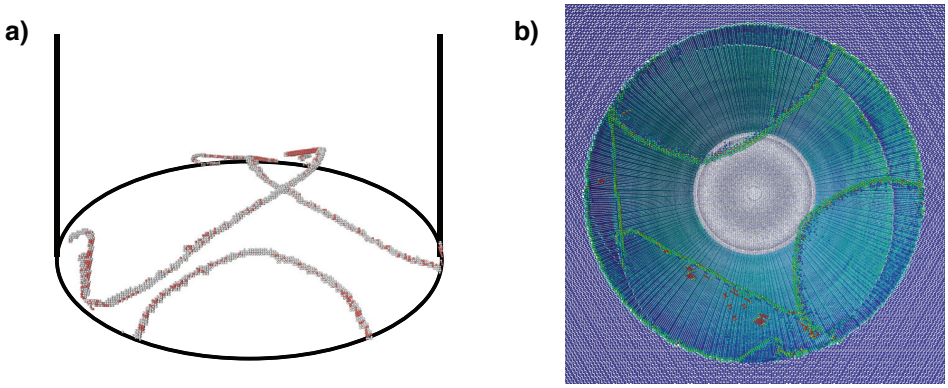

Figure 3.1: Example of the different images possible to make by the use of the analysis methods mentioned above. Both images are from simulations of nanopillar compression, presented in Paper III [3]. a) shows the results of CNA, where all bcc atoms and atoms on the pillar surface have been removed in order to view the dislocation loops inside the pillar. White atoms are of unknown lattice structure, and red atoms are screw/mixed dislocations. The black lines are added to show the sides and bottom of the pillar. b) shows only atoms with a high potential energy, and we view the pillar from below. Only surface atoms and dislocations are visible, and the coloring is done according to the von Mises stress (red is high and blue is low stress).

Chapter 4

Fracture in iron

This chapter gives a motivation for Papers I and II [1, 2], and touches upon some of the results of this research. A basic introduction to the necessary fracture mechanics theory is followed by a small review of literature on iron fracture simulations. Finally, more specific motivation for the papers is presented.

4.1 Some fracture mechanics

4.1.1 Material properties

Linear elastic fracture mechanics (LEFM) is the most basic type of fracture mechanics, dealing with linear elastic materials. These materials have a linear relationship between stress and strain, and are idealized materials which are easier to treat analytically than real materials. The assumption of linear behavior implies that the material will return to its original state once the stress is removed, and no yielding is considered. Many metals and plastics will behave in an approximately linear elastic way for small loads and deformations, so up to a certain threshold the linear elastic treatment could provide good results. The linear relation between stress, σ, and strain, ε, is

$$\sigma = E\varepsilon, \tag{4.1}$$

where the linear constant E is the *Young's modulus* for the given material. (E will be equal in all directions for isotropic materials.) Another important parameter for linear elastic materials is the *Poisson ratio* ν, which gives the ratio of deformation in directions perpendicular to an applied load, relative to the deformation in the load direction. More about LEFM can be found in any standard fracture mechanics textbook, e.g. [12].

An important feature of iron is that it is *anisotropic*, which means that it will give different response depending on which crystallographic direction you load along. This results in values of E varying with the loading direction, as seen in all our three papers. From e.g. the book by

Dieter [66] we have the generalized Hooke's law for the stress and strain tensors σ_{ij} and ε_{ij}

$$\sigma_{ij} = C_{ijkl}\varepsilon_{kl} \qquad \Longleftrightarrow \qquad \varepsilon_{ij} = S_{ijkl}\sigma_{kl} \tag{4.2}$$

where C_{ijkl} and S_{ijkl} are the elastic constants and compliance tensor, respectively, which can be derived from each other. In simulations we normally know C_{11}, C_{12} and C_{44} values for the potential used, and can convert them into the corresponding S_{ij} values.

Having obtained the values of the compliance constants, the modulus of elasticity in a given direction can be found by

$$\frac{1}{E} = S_{11} - 2\left[(S_{11} - S_{12}) - \frac{1}{2}S_{44}\right](l^2m^2 + m^2n^2 + l^2n^2), \tag{4.3}$$

where l, m and n are the directional cosines. The last parenthesis sums up to 0, 1/4 and 1/3 for $\langle 100\rangle$, $\langle 110\rangle$ and $\langle 111\rangle$ directions, respectively. Elastic moduli calculated from potential values can then be compared with the measured E_{ijk} values from the simulations.

Materials can be mechanically loaded in different ways, usually divided into Mode I, II and III (or combinations of these). Mode I is uniaxial tension, Mode II is in-plane shear and Mode III is out-of-plane shear loading, and these three modes might affect the material response significantly. The research presented in this thesis consist solely of Mode I material loading, in order to keep some parameters fixed. This is also the most used testing mode in experiments, for instance in the single-edged notched tension (SENT) configuration (see e.g. [12] for details).

4.1.2 The stress intensity factor K

A material loaded in Mode I, II or III can be analyzed analytically, assuming that we have an isotropic linear elastic material. A very general expression for the stress field tensor σ_{ij} in such a material, using a polar coordinate system with origin at the crack tip, is [67]

$$\sigma_{ij}(r,\theta) = \left(\frac{k}{\sqrt{r}}\right) f_{ij}(\theta) + \sum_{m=0}^{\infty} A_m r^{m/2} g_{ij}^{(m)}(\theta), \tag{4.4}$$

where r is the distance from the crack, f_{ij} and g_{ij} are dimensionless angle-dependent functions, A_m is the amplitude for higher-order terms and k is a constant. Close to the crack tip, $r \to 0$, the $1/\sqrt{r}$ term will dominate, as this term is singular at the origin, and this will describe the stress in this region.

Depending of the loading mode (I, II or III), the amplitude of the singularity will be different, yet they all produce a singularity at the crack tip. The convention in fracture mechanics is to replace the constant k in (4.4) with the so-called *stress intensity factor* K, which is expressed as $K = k\sqrt{2\pi}$. Thus, close to the crack tip we will have

$$\sigma_{ij} \propto \frac{K}{\sqrt{2\pi r}} f_{ij}(\theta), \tag{4.5}$$

where K should be replaced by K_I, K_{II} or K_{III}, depending on the loading mode.

One can derive closed-form solutions for K in some simple geometries, where the value of K will depend on the external load σ and the crack size. For instance, for a semi-infinite plate loaded in tensile stress with a through-thickness crack of half-length a, the Mode I stress intensity factor K_I will be $K_I = \sigma\sqrt{\pi a}$.

Another important quantity in LEFM is the *energy release rate* $\mathcal{G}$, which describes the energy released by extending a crack an increment. This can be linked to K_I in linear elastic materials as

$$\mathcal{G} = \frac{K_I^2}{E'}, \tag{4.6}$$

where $E' = E$ for plane stress and $E' = E/(1-\nu^2)$ for plane strain, ν being the Poisson ratio of the material.

4.1.3 Surface and unstable stacking fault energy, and link to fracture parameters

It is of importance to know the surface energy (per unit area), γ_s, of relevant crack planes in α-iron, in order to compare simulation results with the Griffith criterion $\mathcal{G}_{\text{Gr}} = 2\gamma_s$, which links γ_s to the energy release rate $\mathcal{G}_{\text{Gr}}$. This expression implies that the surface with the lowest γ_s will be the preferred cleavage plane.

The value of the surface energy will, of course, vary for the different crack planes, but it is also different when changing the interatomic potential used in the calculations. A good potential should reproduce the "correct" surface energy values (although it is difficult to know what is the correct value, due to several definitions and quite varied results). Of greater importance, however, is the *ranking* of the surface energy, since the Griffith criterion predicts that cleavage on the plane of lowest surface energy. Surface energies for iron are presented in e.g. [11,68], and in a majority of the calculations the ranking of planes due to the value of γ_s is (110) < (100) < (111), with only a small difference between the (110) and (100) planes.

Another quantity, defined by Rice [69], is the *unstable stacking fault energy* γ_{us}, which is a measure of a material's intrinsic resistance to dislocation emission. This can be measured by shearing two semi-infinite material blocks: The unstable stacking fault energy is then the maximum energy barrier passed as the adjacent atomic layers shear against each other. An expression similar to the Griffith criterion can be formulated, $\mathcal{G}_{\text{emit}} = \gamma_{us} Y$, where the energy release rate $\mathcal{G}_{\text{emit}}$ for dislocation emission is a function of γ_{us} and the geometric factor Y defined by the slip system relative to the crack plane and crack growth direction.

By comparing the expressions presented above we can now find the competition between dislocation emission and crack growth, and if $\mathcal{G}_{\text{emit}} < \mathcal{G}_{\text{Gr}}$, the crack is expected to blunt.

4.1.4 The T-stress

In (4.4) there is a series of higher-order terms that are normally neglected due to the dominance of the $1/\sqrt{r}$-term close to a crack. The first of these terms is constant, and is a stress parallel with the crack plane, called the *T-stress*. By changing the value of T one can model various *constraint* levels, which could qualitatively be equivalent to simulating different experimental conditions.

A simple but effective way of introducing a T-stress in a simulation is by using a *modified boundary layer* (MBL) approach, where the boundaries of a simulation systems are moved according to analytic displacement equations. The inside of the system is allowed to react and move freely, thus by using this method we effectively simulate a semi-infinite crack system. In Paper I [1] multiscale simulations using an MBL approach was used, and both stress-intensity values K_I and values of the T-stress were used as input in the displacement equations. From the resulting critical K_I-values, an effective surface energy γ_{eff} was estimated, and turned out to change with the T-stress. For further results the reader is referred to the paper.

4.2 Fracture simulations in iron

During the last decades many atomistic simulations of Mode I loading of cracks in α-iron have been performed. Thorough reviews on this topic are included in the Introduction sections of Papers I and II [1,2], so we only present some key results here. A variety of edge crack orientations have been examined in the literature, but the most commonly studied are cracks on {110} and {100} planes with different crack front directions. In the following, (...) and {...} denote crack planes, while [...] and ⟨...⟩ denote the *crack front direction* (normal to the crack growth direction). A typical example of a crack orientation is shown in Figure 4.1.

A (001)[110] edge crack is known to extend by bond-breaking [19,52,70,71], sometimes accompanied by twinning in the "easy twinning" slip system $\{112\}\langle 111\rangle$ or by bcc $\rightarrow$ fcc transformation. In the same plane also lies the (001)[010] crack, which is observed to extend, but on {110} planes $\pm 45^\circ$ with respect to the original crack plane [19].

Looking at the (110) plane, we get brittle crack growth with a [010] crack front [19, 52, 72], also sometimes accompanied by phase transformation. With a $[1\bar{1}0]$ crack front, however, dislocation emission in the $\{112\}\langle 111\rangle$ slip system is seen in almost all cases [19, 52].

The (111) plane is more rarely simulated, since its high surface energy makes it more unlikely to be a cleavage plane. At least one study has been performed [52], and here dislocation emission in a $\{110\}\langle 111\rangle$ slip system was observed for a $\langle 112\rangle$ crack front. With a $\langle 110\rangle$ crack front, twinning started spreading along {112} planes normal to the crack-tip.

With all this and many more references using edge cracks, it is time to have a look at what new revelations a more three-dimensional crack geometry like the penny-shaped crack has to offer.

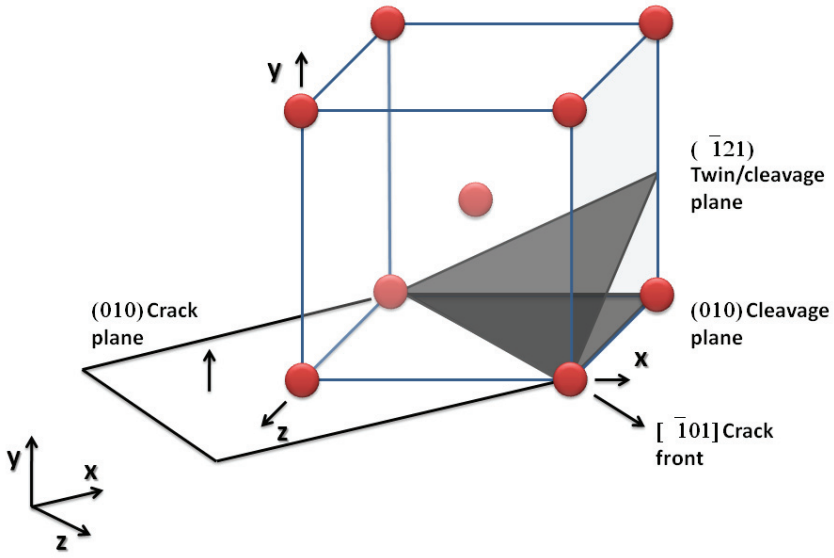

Figure 4.1: A typical crack orientation in fracture simulations, with crack plane (010) and an [101] crack front. Figure made by Inga Vatne, used with permission.

4.3 Through-thickness and penny-shaped cracks

As mentioned in Section 4.1.2, the stress-intensity factor of a through-thickness crack can be estimated as $K_I = \sigma\sqrt{\pi a}$. For a penny-shaped crack, the corresponding expression will be $K_I = \frac{2}{\pi}\sigma\sqrt{\pi a} \approx 0.6\sigma\sqrt{\pi a}$. This means that the crack geometry should make the penny-shaped crack able to withstand a larger external load than the through-thickness crack.

Figure 4.2 shows sketches of the systems simulated in Paper II (and the penny-shaped crack in Paper I), and we notice that the through-thickness crack can be simulated as a thin, semi-2D system, which greatly limits the crack's possible growth directions. The penny-shaped crack, on the other hand, is a full 3D system where the crack is more free to choose an energetically favored direction to grow or emit dislocations.

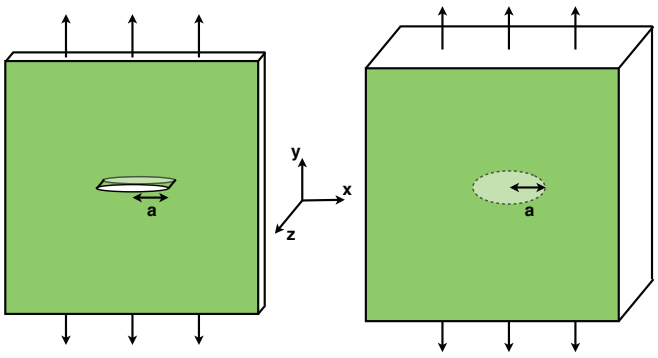

Figure 4.2: System overview for a through-thickness and a penny-shaped crack, used in Paper II [2].

What we noticed when going through literature was that no one had done atomistic modeling of penny-shaped cracks before, at least not to the best of our knowledge. Several authors have studied nucleation and growth of *voids* in metals, which is of course also a 3D problem, but this is almost exclusively done on fcc materials like copper [73–77] and nickel [78]. The few studies on bcc materials have been with tantalum [79, 80], vanadium, niobium, molybdenum and tungsten [81]. Thus we could study both a new material *and* a new crack geometry by choosing a penny-shaped crack in iron. We also believe this would model typical brittle particles within a material, where the initial crack might be flat and semi-circular.

The six crack geometries described in the previous section were used in through-thickness crack simulations, while for penny-shaped cracks only the three crack planes are needed, since all possible crack growth directions are available along the circular crack-tip. The results of this study can be found in full in Paper II, and in addition one of the penny-shaped crack plane simulations was further studied and compared with multiscale crack simulations in Paper I. We observed interesting shape-changing mechanisms of the crack front in the penny-shaped case, which is something that cannot be seen in regular semi-2D simulations.

Chapter 5

Iron nanopillars

After several studies of cracks in iron, it is now time to look at deformation of iron nanostructures. Almost a decade ago Uchic et al. [82] investigated material strength by using a focused ion beam (FIB) to make pillars in a variety of sizes and subsequently compressing them using a nanoindenter tip. It was found that the smaller pillars had markedly higher yield strength values, and this has since gained a lot of attention by researchers both in the experimental and simulation communities.

Micro- and nanopillar compression testing has been further developed and used to investigate a variety of materials at the micron and sub-micron scale. With FIB milling as the most important technique [83–86], small circular pillars can be made on various material surfaces. The pillars are then tested in a nanoindenter by using a hard flat tip to compress the pillars. This enables researchers to, in a precise manner, study material properties at points of interest in a complicated microstructure, which for metals include single grains, grain boundaries, multigrain and multiphase structures.

5.1 Experiments on fcc and bcc pillars

A well-known expression within this type of research is "smaller is stronger", which points at the strengthening in materials with increasingly small dimensions. The yield stress σ_y is said to be following a trend $\sigma_y \propto D^{-\alpha}$, where D is the pillar diameter. In Paper III [3] a thorough literature review on this topic is given, so only a brief summary is given here.

The size-strengthening effect has been observed in both fcc [82, 87–90] and bcc [60, 83, 86, 91, 92] materials, normally with fcc having α-values $3-4$ times larger than for bcc. One exception is [57], where two different size regimes in bcc pillars were found. As the pillar diameter was reduced below ≈ 200 nm, an α-value close to the one for fcc was found.

It is also known that strain rate affects the yield strength in nanostructures [59, 61] as well as temperature [61, 91, 93]. The initial dislocation density also influences material behavior. In an

almost dislocation-free nanopillar a strength approaching the theoretical limit was shown [94]. In our MD simulations the pillars are made of perfect, dislocation-free material, so we would naturally expect high material strength.

Figure 5.1 shows an example of experimental nanopillar compression, performed on high-strength low alloy steel (HSLA) here at NTNU [84]. This lab activity was what originally sparked the idea for us to try modeling the same procedure, and we hope in the future to see compression of extremely small pure iron samples with well-defined crystallographic orientations, so we can compare simulations and experiments one-to-one, at least in size.[1]

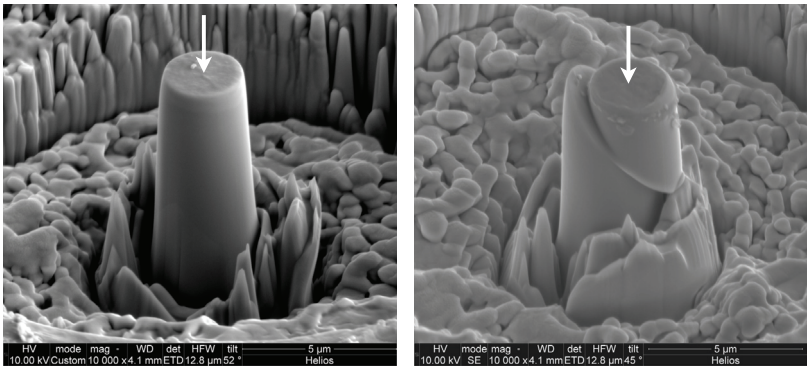

Figure 5.1: Example of experimental nanopillar compression. Images from a high-strength low alloy (HSLA) steel sample of diameter 3.1 µm before (left) and after (right) $\sim 15\%$ compression, where it is clearly seen that slip has occurred along specific planes in the structure. From [84], used with permission from Bjørn Rune Rogne.

5.2 Nanopillar simulations

Numerous molecular dynamics (MD) and dislocation dynamics (DD) simulations of nanopillar and nanowire compression have been performed the past few years [61, 93, 95–103], studying the effects mentioned above, but have also given a lot of attention to how dislocations behave in very small structures.

There seems to be a profound difference in how dislocations move and eventually multiply in fcc and bcc materials. Fcc materials exhibit an effect of *dislocation starvation*, which means that existing and nucleated dislocations quickly escape to the material surface and disappear [88, 104]. This mechanism is proposed to be mainly responsible for increased strength at the nanoscale. Bcc materials, on the other hand, has *dislocation multiplication* taking place, where a single dislocation loop might curl around itself and create more dislocations as it moves through the

[1] As mentioned in Section 3.1 there is still a large gap when it comes to strain rates.

metal. This results in only a modest strengthening effect. Bcc micropillars are thus unlikely to become "dislocation-starved", and would allow further plastic deformation.

Only a limited number of simulations of iron nanopillars could be found in the literature. Paper III [3] extends this research by studying nanopillars located on a solid surface. The reader is referred to Paper III for further details and results from this study.

Acknowledgments

To work on a PhD is a strange yet wonderful experience, which is easily comparable to a long, adventurous journey. In the beginning you have a starting point, a direction and a vague impression of the goal somewhere beyond the horizon. As you start exploring the field and dive into the unknown, there is an overwhelming feeling of knowing little, or nothing at all, compared to everything that is out there. But as time goes by, you learn to navigate the landscape and find your way around. The goal might change from time to time, and the path takes many twists and (dangerous?) turns before arriving there, but every day you move further, always picking at the boundaries of knowledge. Finally, the day comes when you reach your destination. You might feel exhausted, but when looking back you see all the wonders and experiences that was along the way, and you know it was worth it.

Now for some new adventures!

I would like to thank some of the people who has been following me on my journey these last couple of years. First and foremost, I would like to thank my supervisor Prof. Christian Thaulow for guiding me in the right direction and always being such an enthusiastic and creative person. When all I could see was limitations and difficulties, Christian saw possibilities and new things to explore. His positive attitude affects everyone around him, and I really appreciate him being there.

I have had the pleasure of having Dr. Erling Østby as my co-supervisor, and I would like to thank him for all his invaluable input to my papers, many great discussions about new and old music, and for showing me how to properly party at a "julebord".

Prof. Diana Farkas also stands out as one of the people that has truly helped me in reaching my goals through these last years. She has been extraordinary helpful and welcoming during my two stays at Virginia Tech. She also has an incredible experience with MD simulations, and provided me with significant help and input.

My simulation results would not have been much, had it not been for the wonderful Ovito software made by Alexander Stukowski. I have had a lot of correspondence with him over the years, and he has been able to implement everything I have asked about in his software. I am amazed by the work he has put down in making this tool, both for himself and for all the metal simulation researchers out there.

Bjørn Lindi, Arve Dispen, Jan Christian Meyer and Lars Eilertsen at the IT department has been extremely helpful when it comes to teaching me about running simulations on the supercomputer, installing software and finding ways of making my simulations faster and more efficient. Universities all around the world should be jealous of NTNU for having an HPC team like them.

The everyday scientific and social company of my colleagues is something I value highly, and I wish to thank the following people for discussions, parties, research input, movie nights, company at the weekly "Friday porridge lunch" and much more (in no particular order): Knut S. Gjerden, Fredrik Widerøe, Antonio Alvaro (ciao!), Jørn Skogsrud, Gaute Kolstad, Bjørg Granly, Håkon Gundersen, Martin Gudem, Bjørn Rune Rogne, Adina Başa and anyone who feel that they should have been on this list.

One person that deserves extra thanks is Inga Vatne, with whom I have shared an office since day one of my PhD. We have had many discussions, trips and a lot of fun together, and it has been a joy working with her.

I wish to thank my girlfriend Stine for sticking with me these last couple of years, even though I am not always the easiest to live with. You make my every day brighter!

Last, but certainly not least, I would like to thank my family for all their support, both then and now. Especially, I would like to thank my mom Eva and dad Hasse for all their hard work and tough prioritizing which has given me all the possibilities in life I could ever dream of. Thank you for always being there!

Christer H. Ersland

Some of the people that have filled the workdays with fun and discussions the last couple of years.

Bibliography

[1] C. H. Ersland, C. Thaulow, I. R. Vatne, E. Østby, Atomistic modeling of micromechanisms and T-stress effects in fracture of iron, **79** (2012) 180 – 190. doi:10.1016/j.engfracmech.2011.10.012.

[2] C. H. Ersland, I. R. Vatne, C. Thaulow, Atomistic modeling of penny-shaped and through-thickness cracks in bcc iron, Submitted to Modelling and Simulation in Materials Science and Engineering.

[3] C. H. Ersland, C. Thaulow, Modeling of size and strain rate effects in compression tests of iron nanopillars, Submitted to Computational Materials Science.

[4] E. Kuramoto, Y. Aono, K. Kitajima, Thermally activated slip deformation of high purity iron single crystals between 4.2 K and 300 K, **13** (11) (1979) 1039 – 1042. doi:10.1016/0036-9748(79)90199-6.

[5] D. M. Clatterbuck, D. C. Chrzan, J. W. Morris, The ideal strength of iron in tension and shear, **51** (8) (2003) 2271 – 2283. doi:10.1016/S1359-6454(03)00033-8.

[6] J. W. Morris, C. R. Krenn, D. Roundy, M. L. Cohen, Deformation at the limit of elastic stability, **309-310** (2001) 121 – 124. doi:10.1016/S0921-5093(00)01735-4.

[7] R. W. K. Honeycombe, The plastic deformation of metals, Edward Arnold (Publishers) Ltd., 1968.

[8] N. P. Allen, B. E. Hopkins, J. E. McLennan, The tensile properties of single crystals of high-purity iron at temperatures from 100 to -253 degrees C, **234** (1197) (1956) 221–246. doi:10.1098/rspa.1956.0029.

[9] W. Biggs, P. Pratt, The deformation and fracture of alpha-iron at low temperatures, **6** (11) (1958) 694 – 703. doi:10.1016/0001-6160(58)90060-9.

[10] J. Nohava, P. Haušild, M. Karlík, P. Bompard, Electron backscattering diffraction analysis of secondary cleavage cracks in a reactor pressure vessel steel, **49** (3) (2002) 211 – 217. doi:10.1016/S1044-5803(02)00360-1.

[11] P. Błoński, A. Kiejna, Structural, electronic, and magnetic properties of bcc iron surfaces, **601** (1) (2007) 123–133. doi:10.1016/j.susc.2006.09.013.

[12] T. L. Anderson, Fracture mechanics: fundamentals and applications, 3rd edition, CRC Press, New York, USA, 2005.

[13] D. Hull, D. Bacon, Introduction to dislocations, 4th Edition, Butterworth-Heinemann, 2001.

[14] D. Caillard, TEM in situ straining experiments in Fe at low temperature, **89** (8) (2009) 517–526. doi:10.1080/09500830903127518.

[15] D. Caillard, Kinetics of dislocations in pure Fe. part I. in situ straining experiments at room temperature, **58** (9) (2010) 3493–3503. doi:10.1016/j.actamat.2010.02.023.

[16] D. Caillard, Kinetics of dislocations in pure Fe. part II. in situ straining experiments at low temperature, **58** (9) (2010) 3504–3515. doi:10.1016/j.actamat.2010.02.024.

[17] A. Latapie, D. Farkas, Molecular dynamics simulations of stress-induced phase transformations and grain nucleation at crack tips in Fe, **11** (5) (2003) 745. doi:10.1088/0965-0393/11/5/303.

[18] K. Kadau, T. C. Germann, P. S. Lomdahl, B. L. Holian, Atomistic simulations of shock-induced transformations and their orientation dependence in bcc Fe single crystals, **72** (2005) 064120. doi:10.1103/PhysRevB.72.064120.

[19] I. R. Vatne, E. Østby, C. Thaulow, D. Farkas, Quasicontinuum simulation of crack propagation in bcc-Fe, **528** (15) (2011) 5122 – 5134. doi:10.1016/j.msea.2011.03.006.

[20] Y. Ivanisenko, I. MacLaren, R. Valiev, H.-J. Fecht, The first observation of a shear-induced bcc $\rightarrow$ fcc transformation in nanocrystalline ferrite, **7** (11) (2005) 1011–1014. doi:10.1002/adem.200500152.

[21] Y. Ivanisenko, I. MacLaren, X. Sauvage, R. Valiev, H.-J. Fecht, Shear-induced $\alpha \rightarrow \gamma$ transformation in nanoscale Fe-C composite, **54** (6) (2006) 1659 – 1669. doi:10.1016/j.actamat.2005.11.034.

[22] Z. Nishiyama, X-ray investigation of the mechanism of the transformation from face centered cubic lattice to body centered cubic lattice, **23** (1934) 638.

[23] G. Wassermann, Über den Mechanismus der $\alpha \rightarrow \gamma$ Umwandlung des Eisens, **17** (1935) 149.

[24] A. J. Bogers, W. G. Burgers, Partial dislocations on the {110} planes in the B.C.C. lattice and the transition of the F.C.C. into the B.C.C. lattice, **12** (2) (1964) 255–261. doi:10.1016/0001-6160(64)90194-4.

[25] G. Kurdjumow, G. Sachs, Über den Mechanismus der Stahlhärtung, **64** (1930) 325–343. doi:10.1007/BF01397346.

[26] S. J. Plimpton, Fast parallel algorithms for short-range molecular dynamics, **117** (1995) 1–19.

[27] L. Verlet, Computer "experiments" on classical fluids. I: Thermodynamical properties of Lennard-Jones molecules, **159** (1) (1967) 98.

[28] D. Frenkel, B. Smit, Understanding molecular simulation. From algorithms to applications, 2nd Edition, Academic Press, San Diego, 2002.

[29] W. C. Swope, H. C. Andersen, P. H. Berens, K. R. Wilson, A computer simulation method for the calculation of equilibrium constants for the formation of physical clusters of molecules: Application to small water clusters, **76** (1982) 637.

[30] S. Nosé, A molecular dynamics method for simulations in the canonical ensemble, **100** (1) (2002) 191–198.

[31] W. G. Hoover, Canonical dynamics: Equilibrium phase-space distributions, **31** (1985) 1695–1697. doi:10.1103/PhysRevA.31.1695.

[32] W. Shinoda, M. Shiga, M. Mikami, Rapid estimation of elastic constants by molecular dynamics simulation under constant stress, **69** (2004) 134103. doi:10.1103/PhysRevB.69.134103.

[33] M. Parrinello, A. Rahman, Polymorphic transitions in single crystals: A new molecular dynamics method, **52** (1981) 7182. doi:10.1063/1.328693.

[34] M. S. Daw, M. I. Baskes, Semiempirical, quantum mechanical calculation of hydrogen embrittlement in metals, **50** (17) (1983) 1285–1288. doi:10.1103/PhysRevLett.50.1285.

[35] M. S. Daw, M. I. Baskes, Embedded-atom method: Derivation and application to impurities, surfaces, and other defects in metals, **29** (12) (1984) 6443–6453. doi:10.1103/PhysRevB.29.6443.

[36] J. Tersoff, New empirical approach for the structure and energy of covalent systems, **37** (12) (1988) 6991–7000.

[37] K. Albe, K. Nordlund, R. S. Averback, Modeling the metal-semiconductor interaction: Analytical bond-order potential for platinum-carbon, **65** (19) (2002) 195124. doi:10.1103/PhysRevB.65.195124.

[38] M. I. Mendelev, S. Han, D. J. Srolovitz, G. J. Ackland, D. Y. Sun, M. Asta, Development of new interatomic potentials appropriate for crystalline and liquid iron, **83** (35) (2003) 3977–3994.

[39] M. Ruda, D. Farkas, G. Garcia, Atomistic simulations in the Fe-C system, **45** (2) (2009) 550–560. doi:10.1016/j.commatsci.2008.11.020.

[40] T. T. Lau, C. J. Först, X. Lin, J. D. Gale, S. Yip, K. J. van Vliet, Many-body potential for point defect clusters in Fe-C alloys, **98** (21) (2007) 215501.

[41] M. W. Finnis, J. E. Sinclair, A simple empirical N-body potential for transition metals, **50** (1) (1984) 45–55.

[42] G. J. Ackland, D. J. Bacon, A. F. Calder, T. Harry, Computer simulation of point defect properties in dilute Fe-Cu alloy using a many-body interatomic potential, **75** (3) (1997) 713–732.

[43] G. J. Ackland, M. I. Mendelev, D. J. Srolovitz, S. Han, A. V. Barashev, Development of an interatomic potential for phosphorus impurities in α-iron, **16** (2004) S2629–S2642.

[44] H. Chamati, N. Papanicolaou, Y. Mishin, D. Papaconstantopoulos, Embedded-atom potential for Fe and its application to self-diffusion on Fe(1 0 0), **600** (9) (2006) 1793–1803. doi:10.1016/j.susc.2006.02.010.

[45] D. J. Hepburn, G. J. Ackland, Metallic-covalent interatomic potential for carbon in iron, **78** (16) (2008) 165115. doi:10.1103/PhysRevB.78.165115.

[46] A. Ramasubramaniam, M. Itakura, E. A. Carter, Interatomic potentials for hydrogen in α-iron based on density functional theory, **79** (17) (2009) 174101. doi:10.1103/PhysRevB.79.174101.

[47] M. Ruda, D. Farkas, J. Abriata, Interatomic potentials for carbon interstitials in metals and intermetallics, **46** (5) (2002) 349–355.

[48] M. Müller, P. Erhart, K. Albe, Analytic bond-order potential for bcc and fcc iron - comparison with established embedded-atom method potentials, **19** (2007) 326220.

[49] K. O. E. Henriksson, K. Nordlund, Simulations of cementite: An analytical potential for the Fe-C system, **79** (14) (2009) 144107. doi:10.1103/PhysRevB.79.144107.

[50] M. Mrovec, D. Nguyen-Manh, C. Elsässer, P. Gumbsch, Magnetic bond-order potential for iron, **106** (2011) 246402. doi:10.1103/PhysRevLett.106.246402.

[51] C. H. Ersland, C. Thaulow, D. Farkas, E. Østby, Atomistic studies and comparison of α-Fe potentials in mode I fracture, in: Proceedings of the 18th European Conference on Fracture, 2010.

[52] P. A. Gordon, T. Neeraj, M. J. Luton, D. Farkas, Crack-tip deformation mechanisms in α-Fe and binary Fe alloys: an atomistic study on single crystals, **38A** (2007) 2191–2202.

[53] C. Engin, L. Sandoval, H. M. Urbassek, Characterization of Fe potentials with respect to the stability of the bcc and fcc phase, **16** (3) (2008) 035005.

[54] S. L. Frederiksen, K. W. Jacobsen, Density functional theory studies of screw dislocation core structures in bcc metals, **83** (3) (2003) 365–375. doi:10.1080/0141861021000034568.

[55] C. Domain, G. Monnet, Simulation of screw dislocation motion in iron by molecular dynamics simulations, **95** (21) (2005) 215506. doi:10.1103/PhysRevLett.95.215506.

[56] C. H. Ersland, C. Thaulow, E. Østby, Atomistic simulations of semi-infinite cracks in bcc iron using an analytic bond-order potential, in: Proceedings of the Twenty-first (2011) International Offshore and Polar Engineering Conference, International Society of Offshore and Polar Engineers (ISOPE), 2011, pp. 432–437.

[57] L. Huang, Q.-J. Li, Z.-W. Shan, J. Li, J. Sun, E. Ma, A new regime for mechanical annealing and strong sample-size strengthening in body centred cubic molybdenum, **2**. doi:10.1038/ncomms1557.

[58] D. Brunner, J. Diehl, Temperature and strain-rate dependence of the tensile flow stress of high-purity α-iron below 250 K I. stress/temperature regime III, **124** (1991) 455–464. doi:10.1002/pssa.2211250117.

[59] A. T. Jennings, J. Li, J. R. Greer, Emergence of strain-rate sensitivity in Cu nanopillars: Transition from dislocation multiplication to dislocation nucleation, **59** (14) (2011) 5627 – 5637. doi:10.1016/j.actamat.2011.05.038.

[60] A. Schneider, B. Clark, C. Frick, P. Gruber, E. Arzt, Effect of orientation and loading rate on compression behavior of small-scale Mo pillars, **508** (1 - 2) (2009) 241 – 246. doi:10.1016/j.msea.2009.01.011.

[61] T. Zhu, J. Li, A. Samanta, A. Leach, K. Gall, Temperature and strain-rate dependence of surface dislocation nucleation, **100** (2) (2008) 025502. doi:10.1103/PhysRevLett.100.025502.

[62] A. Stukowski, Visualization and analysis of atomistic simulation data with OVITO – the open visualization tool, **18** (1) (2010) 015012.

[63] D. Faken, H. Jónsson, Systematic analysis of local atomic structure combined with 3D computer graphics, **2** (1994) 279–286.

[64] H. Tsuzuki, P. S. Branicio, J. P. Rino, Structural characterization of deformed crystals by analysis of common atomic neighborhood, **177** (6) (2007) 518 – 523. doi:10.1016/j.cpc.2007.05.018.

[65] A. Stukowski, K. Albe, Extracting dislocations and non-dislocation crystal defects from atomistic simulation data, **18** (8) (2010) 085001.

[66] G. E. Dieter, Mechanical metallurgy, 3rd Edition, McGraw-Hill Science Engineering, Singapore, 1986.

[67] M. L. Williams, On the stress distribution at the base of a stationary crack, **24** (1957) 109–114.

[68] P. Błoński, A. Kiejna, Calculation of surface properties of bcc iron, **74** (2) (2004) 179–183, proceedings of the International Workshop on Surface Physics: Metals on Solid Surfaces. doi:10.1016/j.vacuum.2003.12.118.

[69] J. R. Rice, Dislocation nucleation from a crack tip: an analysis based on the peierls concept, **40** (2) (1992) 239–271.

[70] A. Machová, G. E. Beltz, Ductile-brittle behavior of (0 0 1)[1 1 0] nano-cracks in bcc iron, **387-389** (2004) 414–418, 13th International Conference on the Strength of Materials. doi:10.1016/j.msea.2003.11.089.

[71] P. Hora, V. Pelikán, A. Machová, A. Spielmannová, J. Prahl, M. Landa, O. Červená, Crack induced slip processes in 3D, **75** (2008) 3612–3623.

[72] V. Shastry, D. Farkas, Molecular statics simulation of fracture in α-iron, **4** (1996) 473–492.

[73] J. Belak, On the nucleation and growth of voids at high strain-rates, **5** (1998) 193–206. doi:10.1023/A:1008685029849.

[74] E. M. Bringa, S. Traiviratana, M. A. Meyers, Void initiation in fcc metals: Effect of loading orientation and nanocrystalline effects, **58** (13) (2010) 4458 – 4477. doi:10.1016/j.actamat.2010.04.043.

[75] L. P. Dávila, P. Erhart, E. M. Bringa, M. A. Meyers, V. A. Lubarda, M. S. Schneider, R. Becker, M. Kumar, Atomistic modeling of shock-induced void collapse in copper, **86** (2005) 161902.

[76] S. Traiviratana, E. M. Bringa, D. J. Benson, M. A. Meyers, Void growth in metals: Atomistic calculations, **56** (15) (2008) 3874–3886. doi:10.1016/j.actamat.2008.03.047.

[77] R. Rudd, E. Seppälä, L. Dupuy, J. Belak, Void coalescence processes quantified through atomistic and multiscale simulation, **14** (2007) 425–434. doi:10.1007/s10820-007-9054-0.

[78] M. Q. Chandler, M. Horstemeyer, M. Baskes, P. Gullett, G. Wagner, B. Jelinek, Hydrogen effects on nanovoid nucleation in face-centered cubic single-crystals, **56** (1) (2008) 95 – 104. doi:10.1016/j.actamat.2007.09.012.

[79] J. Marian, J. Knap, G. Campbell, A quasicontinuum study of nanovoid collapse under uniaxial loading in Ta, **56** (10) (2008) 2389 – 2399. doi:10.1016/j.actamat.2008.01.050.

[80] Y. Tang, E. M. Bringa, B. A. Remington, M. A. Meyers, Growth and collapse of nanovoids in tantalum monocrystals, **59** (4) (2011) 1354 – 1372. doi:10.1016/j.actamat.2010.11.001.

[81] R. E. Rudd, Void growth in BCC metals simulated with molecular dynamics using the Finnis-Sinclair potential, arXiv.org (2009) 0906.0619v1.

[82] M. D. Uchic, D. M. Dimiduk, J. N. Florando, W. D. Nix, Sample dimensions influence strength and crystal plasticity, **305** (5686) (2004) 986–989. doi:10.1126/science.1098993.

[83] S. Brinckmann, J.-Y. Kim, J. R. Greer, Fundamental differences in mechanical behavior between two types of crystals at the nanoscale, **100** (15) (2008) 155502. doi:10.1103/PhysRevLett.100.155502.

[84] B. R. S. Rogne, C. Thaulow, Investigation of nanomechanical test methods on arctic steels, in: Proceedings of the Twenty-first (2011) International Offshore and Polar Engineering Conference, International Society of Offshore and Polar Engineers (ISOPE), 2011, pp. 426–431.

[85] M. Dietiker, S. Buzzi, G. Pigozzi, J. Löffler, R. Spolenak, Deformation behavior of gold nano-pillars prepared by nanoimprinting and focused ion-beam milling, **59** (5) (2011) 2180 – 2192. doi:10.1016/j.actamat.2010.12.019.

[86] S. M. Han, T. Bozorg-Grayeli, J. R. Groves, W. D. Nix, Size effects on strength and plasticity of vanadium nanopillars, **63** (12) (2010) 1153 – 1156. doi:10.1016/j.scriptamat.2010.08.011.

[87] J. R. Greer, W. C. Oliver, W. D. Nix, Size dependence of mechanical properties of gold at the micron scale in the absence of strain gradients, **53** (6) (2005) 1821 – 1830. doi:10.1016/j.actamat.2004.12.031.

[88] J. R. Greer, W. D. Nix, Nanoscale gold pillars strengthened through dislocation starvation, **73** (2006) 245410. doi:10.1103/PhysRevB.73.245410.

[89] D. Dimiduk, M. Uchic, T. Parthasarathy, Size-affected single-slip behavior of pure nickel microcrystals, **53** (15) (2005) 4065 – 4077. doi:10.1016/j.actamat.2005.05.023.

[90] C. A. Volkert, E. T. Lilleodden, Size effects in the deformation of sub-micron Au columns, **86** (33-35) (2006) 5567–5579. doi:10.1080/14786430600567739.

[91] A. S. Schneider, D. Kaufmann, B. G. Clark, C. P. Frick, P. A. Gruber, R. Mönig, O. Kraft, E. Arzt, Correlation between critical temperature and strength of small-scale bcc pillars, **103** (10) (2009) 105501. doi:10.1103/PhysRevLett.103.105501.

[92] J.-Y. Kim, J. R. Greer, Size-dependent mechanical properties of molybdenum nanopillars, **93** (10) (2008) 101916. doi:10.1063/1.2979684.

[93] A. Cao, E. Ma, Sample shape and temperature strongly influence the yield strength of metallic nanopillars, **56** (17) (2008) 4816 – 4828. doi:10.1016/j.actamat.2008.05.044.

[94] M. Lowry, D. Kiener, M. LeBlanc, C. Chisholm, J. Florando, J. Morris Jr., A. Minor, Achieving the ideal strength in annealed molybdenum nanopillars, **58** (15) (2010) 5160 – 5167. doi:10.1016/j.actamat.2010.05.052.

[95] J. Brown, N. Ghoniem, Reversible-irreversible plasticity transition in twinned copper nanopillars, **58** (3) (2010) 886 – 894. doi:10.1016/j.actamat.2009.10.003.

[96] F. Sansoz, Atomistic processes controlling flow stress scaling during compression of nanoscale face-centered-cubic crystals, **59** (9) (2011) 3364 – 3372. doi:10.1016/j.actamat.2011.02.011.

[97] J. Senger, D. Weygand, P. Gumbsch, O. Kraft, Discrete dislocation simulations of the plasticity of micro-pillars under uniaxial loading, **58** (7) (2008) 587 – 590. doi:10.1016/j.scriptamat.2007.11.031.

[98] E. Rabkin, H.-S. Nam, D. Srolovitz, Atomistic simulation of the deformation of gold nanopillars, **55** (6) (2007) 2085 – 2099. doi:10.1016/j.actamat.2006.10.058.

[99] Y. Gao, Z. Liu, X. You, Z. Zhuang, A hybrid multiscale computational framework of crystal plasticity at submicron scales, **49** (3) (2010) 672 – 681. doi:10.1016/j.commatsci.2010.06.010.

[100] C. Zhou, S. B. Biner, R. LeSar, Discrete dislocation dynamics simulations of plasticity at small scales, **58** (5) (2010) 1565 – 1577. doi:10.1016/j.actamat.2009.11.001.

[101] L. A. Zepeda-Ruiz, B. Sadigh, J. Biener, A. M. Hodge, A. V. Hamza, Mechanical response of freestanding Au nanopillars under compression, **91** (10) (2007) 101907. doi:10.1063/1.2778761.

[102] D. Weygand, M. Poignant, P. Gumbsch, O. Kraft, Three-dimensional dislocation dynamics simulation of the influence of sample size on the stress – strain behavior of fcc single-crystalline pillars, **483-484** (2008) 188 – 190. doi:10.1016/j.msea.2006.09.183.

[103] C. R. Weinberger, W. Cai, The stability of Lomer-Cottrell jogs in nanopillars, **64** (6) (2011) 529 – 532. doi:10.1016/j.scriptamat.2010.11.037.

[104] W. D. Nix, J. R. Greer, G. Feng, E. T. Lilleodden, Deformation at the nanometer and micrometer length scales: Effects of strain gradients and dislocation starvation, **515** (6) (2007) 3152 – 3157. doi:10.1016/j.tsf.2006.01.030.

Paper I

Atomistic modeling of micromechanisms and T-stress effects in fracture of iron

Engineering Fracture Mechanics, **79**, 180-190 (2012)

Engineering Fracture Mechanics 79 (2012) 180–190

Contents lists available at SciVerse ScienceDirect

Engineering Fracture Mechanics

journal homepage: www.elsevier.com/locate/engfracmech

Atomistic modeling of micromechanisms and *T*-stress effects in fracture of iron

C.H. Ersland [a,*], C. Thaulow [a], I.R. Vatne [a], E. Østby [b]

[a] Department of Engineering Design and Materials, Norwegian University of Science and Technology (NTNU), NO-7491 Trondheim, Norway
[b] SINTEF Materials and Chemistry, Department of Applied Mechanics and Corrosion, NO-7465 Trondheim, Norway

ARTICLE INFO

Article history:
Received 10 January 2011
Received in revised form 1 August 2011
Accepted 19 October 2011

Keywords:
Fracture
Atomistic modeling
Iron
T-stress
Dislocations

ABSTRACT

In this paper we explore a possible method to couple atomistic modeling of initiation of fracture in iron with displacement constraints taken from continuum considerations. Molecular dynamics is used to examine the effect of a penny-shaped crack, and the quasicontinuum method is used as a platform for performing multiscale analysis. The modified boundary layer approach enables us to examine the influence of constraint (geometry, crack size and mode of loading) on the fracture mechanisms by changing the *T*-stress (the constant term in the stress series expansion). The results are discussed in relation to how constraint influences upon the crack initiation toughness.

1. Introduction

In this paper we apply atomistic and multiscale material modeling to investigate the influence of constraint and crystallographic orientation on fracture in bcc-Fe.

Traditional fracture mechanics approaches are limited by the stress singularity dominated zones, while the micromechanical events responsible for the initiation of fracture usually takes place close to the crack tip, within the damage or process zones. The philosophy in the continuum mechanics treatment has been that the results from small scale fracture mechanics testing can be transferred to larger geometries as long as the same stress intensity is obtained just outside the process zone. Even though we do not know the actual stresses inside this zone, the argument is that as long as the surrounding *K*-field is the same in both geometries, the same stress distribution will result in equal damage within the zone.

This philosophy was successfully demonstrated in the 1970s and 1980s with 3D elastic–plastic finite element modeling (FEM) [2]. At that time there was a lot of skepticism with respect to FEM and the simulations had to be verified by large scale testing. One such example is from the laboratory at NTNU/SINTEF, where a full scale tensile testing rig with a tensile load capacity of 100 MN was constructed. The test rig was inaugurated in 1989 and several big wide plate test programs on steel and aluminum alloys for offshore applications were conducted. Semi-elliptical surface cracks were positioned in typically 50 mm thick weldments. Evidently we and the industry gained trust in 3D FEM [3–5]. Comparison between experiments and simulations was also performed elsewhere, and has validated the results from FEM [6–8].

As we now move to smaller scales and approach the atomistic level, we again meet challenges in the development of the modeling techniques and to prove the realism of the calculations. The leap from large scale testing with 100 MN to the typically 10 pN loads at the nanoscale, and the reduction of time window from 10 min to 1 femtosecond is enormous, in the range of 10^{18}.

* Corresponding author.
E-mail address: christer.h.ersland@ntnu.no (C.H. Ersland).

0013-7944/$ - see front matter © 2011 Elsevier Ltd. All rights reserved.
doi:10.1016/j.engfracmech.2011.10.012

Nomenclature

a	crack size
bcc	body-centered cubic
BDT	brittle-to-ductile transition
C_{ij}	elastic constants
E	Young's modulus
EAM	embedded-atom method
FEM	finite element modeling
$\mathcal{G}$	energy release rate
K_{cleave}	critical stress-intensity factor for cleavage
K_{disl}	critical stress-intensity factor for dislocation emission
K_I	Mode I stress-intensity factor
MBL	modified boundary layer
QC	quasicontinuum
S_{ij}	compliance constants
T	T-stress – the constant term in the Williams [1] stress series expansion
β	biaxiality ratio, which relates T to the stress-intensity
γ_{eff}	effective surface energy
γ_s	surface energy
γ_{us}	unstable stacking fault energy
ν	Poisson ratio
σ_c	critical local stress at cleavage

The most characteristic feature of the fracture behavior in steels is the *brittle-to-ductile transition* (*BDT*), as depicted by the curve in Fig. 1. Even though the fracture properties at low temperatures have been known for more than a century, the fundamental mechanisms that control the transition temperature have not yet been fully explained. In order to improve the safety and utilize the materials it is therefore important to understand the controlling mechanisms leading to a sudden brittle behavior. This transition has been studied for iron and steels through experiments and simulations for decades (see e.g. [9–14]). For silicon, another brittle material, BDT has recently been studied through atomistic simulations using reactive force fields (ReaxFF) [15,16], giving detailed information about the change in mechanisms as the temperature is increased.

Looking at the BDT curve in Fig. 1, we see that at low temperatures the material behaves very brittle and cleavage fracture is the controlling failure mode. This is often referred to as the *lower shelf* of the BDT curve. As the temperature increases the fracture toughness is increasing, and we enter the *transition region*, which can further be divided into "lower" and "upper" parts. In the *lower transition region* the cleavage fracture is only preceded by limited plasticity at the crack tip. In the *upper transition region* significant plasticity and also ductile tearing may precede the initiation of cleavage fracture. At even higher temperatures we reach the *upper shelf*, where the material behaves ductile and fracture is controlled by ductile tearing. Once

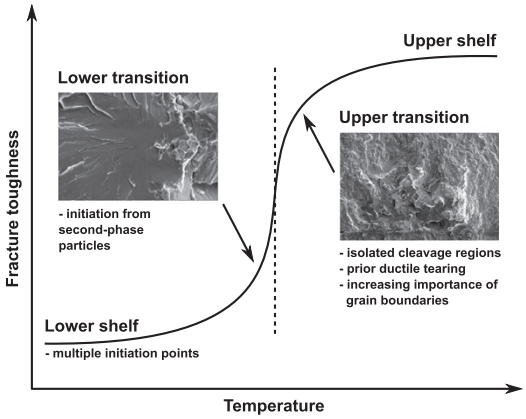

Fig. 1. The brittle-to-ductile (BDT) transition curve of iron and steel, showing examples from real fracture surfaces in steel.

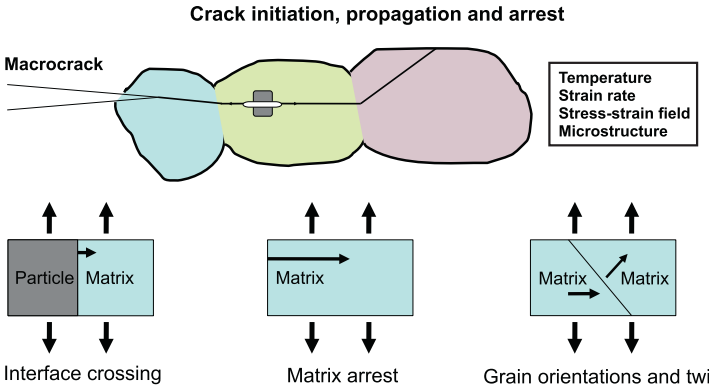

Fig. 2. Critical steps in initiation and propagation of cleavage fracture in steels. The figure indicates areas, where atomistic modeling can be very helpful in the understanding of the critical micromechanisms and the interplay with parameters such as temperature, strain rate, stress – strain field (constraint) and microstructures.

the upper shelf has been reached, only a small temperature effect on the ductile fracture toughness is usually observed when increasing temperature further.

The cleavage fracture event in iron and steel is separated into several critical steps that have to be fulfilled in order to obtain a macroscopic brittle fracture [17]. The critical steps include: (i) nucleation of a microcrack from a particle or brittle microstructure constituent, (ii) propagation of the microcrack over the phase-boundary to the matrix and (iii) propagation of the microcrack across high angle grain boundaries. Fig. 2 indicates areas, where atomistic modeling can be very helpful in the understanding of the critical micromechanisms and the interplay with crucial parameters such as temperature, strain rate, stress–strain field (constraint) and microstructures.

New demands have now been put on steels as the oil and gas industry moves towards the arctic regions. Design temperatures down to −60 °C, combined with harsh weather conditions and icebergs, ice-loads, thaw settlement and landslides are challenging the existing materials, and there is a strong demand to understand the material behavior under these severe conditions. We now introduce atomistic and multiscale material modeling to gain insight in the BDT mechanisms in bcc-Fe and steels.

The outline for the paper is first to relate the atomistic approach to the historical development of fracture mechanics, including a short review of micromechanisms. We then model a penny-shaped embedded crack to gain insight into the first steps of crack intitiation and propagation. The penny-shaped crack can be associated with initiation from an embrittled microconstituent, such as carbides of martensite/austenite (MA) islands in steels. We then apply the *modified boundary layer* (*MBL*) approach on a multiscale model using the *quasicontinuum* (*QC*) method. The introduction of MBL enables us to examine the influence of constraint (geometry, crack size and mode of loading) on the fracture mechanisms by changing the *T*-stress. The results are discussed with respect to the effective fracture energies and the influence of constraint on the critical stress calculations.

2. An atomistic view on fracture

Introductory textbooks on fracture mechanics frequently start with "an atomistic view" on fracture. Since fracture involves the breaking of bonds, the stress at the atomistic level are set equal to the cohesive stress. Atoms held together by springs is used to illustrate the breaking of bonds. For small displacements under linear elastic conditions, the fracture stress is $\sigma_c = E/\pi$. For single crystal iron the Young's modulus E for the (1 1 0) plane is about 220 GPa, resulting in a critical fracture stress of 70 GPa.

By introducing a small defect, the fracture stress is typically reduced by two decades. Inglis was the first to calculate stresses that arises from a sharp notch, and by equating his macroscopic calculations with the atomistic model, the crack size was related to the fracture stress as $\sigma = \sqrt{E\gamma_s/4a}$ [18]. The surface energy γ_s for the (1 1 0) plane of iron is typically around 2 N/m. For a minor defect of say $2a = 0.001$ mm, the theoretical fracture stress is reduced by two orders of magnitude, from the previous 70 GPa to 0.46 GPa.

The early atomistic approach was, however, soon replaced with the linear elastic energy concept introduced by Griffith [19] and later extended by Irwin [20]. The crack extension force approach, $\mathcal{G}$, laid the foundation for the development of the linear elastic stress-intensity fracture mechanics by Willams [1], and closed form equations which then evolved to account for limited crack-tip yielding. The next step was the development of nonlinear approaches with the introduction of *crack-tip opening displacement* (*CTOD*) by Wells [21] and the *J*-integral by Rice [22]. The *J*-integral and CTOD are interrelated through the modulus of elasticity and work hardening exponent, as described by Shih [23]. The more recent advances, incorporating

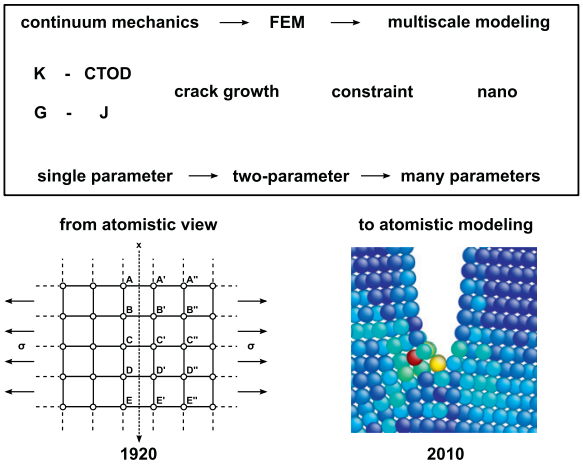

Fig. 3. Overview of the development in fracture mechanics, from continuum based models to atomistic models with an increasing number of interplaying parameters.

ductile crack growth and constraint corrections (T-stress and Q-parameter) extends the number of parameters to be determined. In parallel with these theoretical developments the nonlinear FE methods have been improved, and complex 3D systems can now be treated within reasonable computational cost. The historical journey is illustrated in Fig. 3.

In the same way as the FEM analysis has made it possible to gain completely new insight into relevant continuum parameters, the emergence of atomistic mechanics and multiscale material modeling provides insight to the fracture process zone and paves the way for understanding and quantifying the material failure mechanisms from a fundamental perspective. The atomistic modeling relates detailed microstructural constituents and morphologies associated with the failure mechanisms, and hence support the development of new generations of materials with tailored properties. In relation to iron there has been extensive research using atomistic and multiscale modeling throughout the last decades, including simulation of various fracture scenarios (the effect of crystallographic orientations, loading rates, interatomic potentials) [24–27]; nanoindentation simulations [28,29]; and pure dislocation studies [30–33]. For a broader background on atomistic modeling, specifically linked to materials failure, see e.g. the book by Buehler [34].

3. Micromechanisms

At the atomistic level, a brittle or ductile response of an atomically sharp crack tip to externally applied stresses can be viewed as a competition between initiating a cleavage fracture and the emission of dislocations through the shearing of adjacent atomic layers. Rice proposed a dislocation nucleation criterion based on the Peierls concept [35], and for Mode I plane stress the critical stress intensity factor for dislocation emission is given as

$$K_{\text{disl}} = \sqrt{2\gamma_{us}\mu(1+\nu)Y}, \tag{1}$$

where μ is the shear modulus, ν is Poisson's ratio, Y is a geometric factor given by the angle of dislocation emission (slip plane and direction of sliding) and γ_{us} is the -unstable stacking energy+. The latter is defined as the maximum energy barrier encountered when two semi-infinite blocks of material are sheared relative to each other, and is thus a measure of the theoretical shear strength of the material. For simple lattices, the maximum energy barrier corresponds to a relative displacement of $\vec{b}/2$ between the blocks, where $\vec{b}$ is the Burgers vector.

K_{disl} is then compared with the Griffith stress intensity for brittle cleavage fracture, K_{cleave}, which is directly related to the surface energy γ_s and Young's modulus E. The cracking takes place through the expression

$$K_{\text{cleave}} = \sqrt{2\gamma_s E}. \tag{2}$$

Accordingly, the crack should be expected to emit dislocations and thereby blunt the crack tip, when $K_{\text{disl}} < K_{\text{cleave}}$. Both γ_{us} and γ_s can be directly computed by the atomistic calculations. In the literature the theoretical surface energies γ_s for the cleavage planes in iron are calculated to be in the range of 1.5–2 N/m, while the unstable stacking fault energies γ_{us} vary from 0.7 to 2 N/m for various slip systems (see for example [24,36]).

Iron, with its body-centred cubic unit cell, represents a complicated picture with respect to micromechanisms. The bcc cell has multiple slip planes, but in general they all slip in the close packed directions $\langle 1\,1\,1\rangle$. The literature indicates that while $\{1\,1\,0\}$ planes are common slip planes, the $\{1\,1\,2\}$ and $\{1\,2\,3\}$ planes are also operative. The multiplicity of possible slip

systems is sometimes reflected in a wavy appearance of slip bands. The most pronounced cleavage planes are {1 0 0}, {2 1 1} and {1 1 0}.

The mechanism of brittle fracture of iron is usually regarded as an elastic extension of atomic bonds up to the point of final separation. The total amount of energy which must be expended in producing the fracture is 2γ, "work of fracture" per unit area. For a perfect elastic fracture γ is taken to be the surface energy of the material.

In order to incorporate local plastic deformation and irreversible work the energy release rate $\mathcal{G}_c$ could be expressed as

$$\mathcal{G}_c = 2\gamma_{\text{eff}}, \tag{3}$$

where γ_{eff}, the *effective surface energy* or *work of fracture*, is the sum of all contributions such as dislocations, local heating, surface roughness such as cleavage steps, local phase transformations and any other mechanism. With the atomistic approach we now have the possibility to examine the crack tip mechanisms and estimate the contributions to the work of fracture.

4. Atomistic modeling of a penny-shaped crack

In this section we present an overview of the evolution of crack extension and dislocations from an initially penny-shaped crack embedded in a cube of perfect bcc iron loaded in Mode I tension. The embedded crack could simulate a flat brittle micro-constituent, such as MA-phases in weldments of steel. The simulation is performed for one crack size, i.e. for a given constraint, and one crystallographic orientation, using the software LAMMPS [37].

Fig. 4 shows a schematic overview of the simulated model. The crack is atomistically sharp, lies in the {1 1 0} plane, and is loaded symmetrically normal to this crack plane. The potential used in this simulation is an embedded-atom method (EAM) potential by Ruda and Farkas [38], and the cube length is approximately 600 Å in all directions. Periodic boundary conditions are used within the crack plane, while the boundaries in the loading directions are assigned a certain velocity perpendicular to the crack plane and can not move freely. The evolution of the crack-shape viewed from above (looking down at the crack plane) during crack extension can be seen in Fig. 5, and the same evolution viewed from the side (with the $[1\,\bar{1}\,0]$ direction out of the plane) can be seen in Fig. 6. Descriptions and further details of the steps follow in the sections below. All figures show only atoms with high potential energy, and the atoms are colored by their potential energy value, from blue (low) to red (high). Visualization is done using the software Ovito [39].

Initially, the penny-shaped crack is introduced in the cube by turning off the interactions between two circular layers of atoms, creating an atomistically sharp crack. Fig. 5a shows the crack before any extension has occurred, with the crystallographic directions displayed as well.

The first event in this tensile simulation is that the crack extends by breaking atom bonds in the directions 45° relative to the coordinate axes in the {1 1 0} plane, thus giving the crack a more square-shaped look. This happens at a strain of about 3.1%. The strain is calculated as $\varepsilon = (L - L_0)/L_0$, where L_0 and L is the original and current system length in the loading direction, respectively. Fig. 7a shows an overview over the change in shape due to crack extension, with the original crack shape shown as a dashed ring for comparison. In Fig. 8 the details of the first crack extension event are shown using a slice through

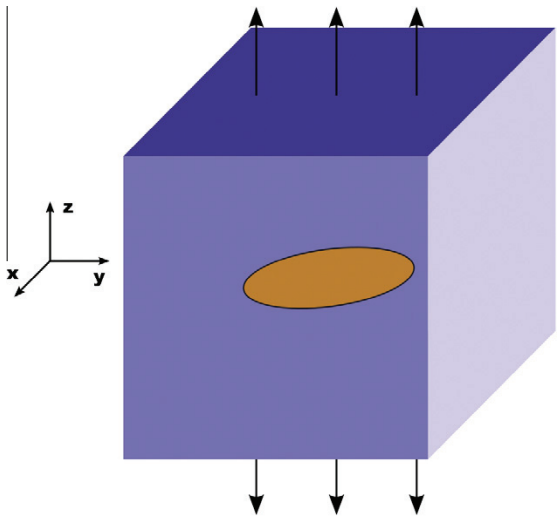

Fig. 4. Overview of the atomistic model a the penny-shaped crack embedded in a cube of single crystal bcc iron.

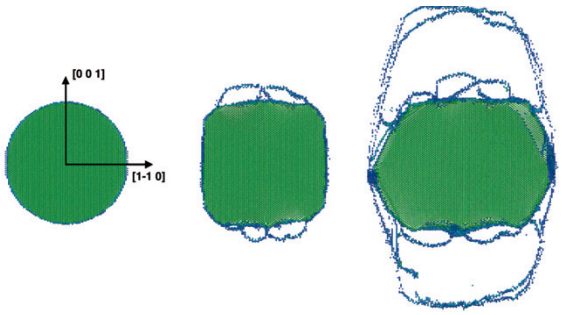

Fig. 5. The evolution of the penny-shaped crack upon loading, with the crack located on the {1 1 0} plane. From initially circular, the crack turns almost square-shaped before evolving further into a six-edged shape as the crack extends in various directions. The development of dislocation loops are visualized. Only atoms with a high potential energy are shown, in order to only see the crack surfaces and high-energy atoms (e.g. dislocations).

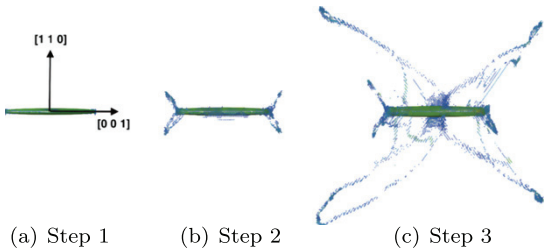

Fig. 6. The evolution of the penny-shaped crack upon loading, looking at the crack shape from the side, with the $[1\,\bar{1}\,0]$ direction out of the plane. We see dislocations emitted as loops, in the $\{2\,1\,1\}\langle 1\,1\,1\rangle$ slip system. Only atoms with a high potential energy are shown, in order to only see the crack surfaces and high-energy atoms (e.g. dislocations).

the crack-plane in the ±45° directions, and we can see how a few atom bonds are broken before a dislocation blunts the crack-tip.

After the small crack extension described above, dislocation loops appear at an angle of about ±55° out of the crack plane in $\langle 1\,1\,1\rangle$ directions, following $\{2\,1\,1\}$ planes. These planes and directions are common slip systems in bcc materials. Due to the change in shape of the crack into a more quadratic form, a larger part of the crack front has "access" to the $\{2\,1\,1\}\langle 1\,1\,1\rangle$ slip system, and can contribute to the dislocations. This is first observed at a strain $\varepsilon = 3.2\%$, but dislocations continue to be emitted as the model is strained further. In Fig. 7b the dislocations and directions are shown.

Due to the dislocation emission, the crack fronts in the $\langle 1\,0\,0\rangle$ directions in the crack plane get blunted. The crack fronts in the non-close-packed $\langle 1\,1\,0\rangle$ directions, however, do not produce dislocations, and at a strain $\varepsilon = 3.5\%$ the crack starts

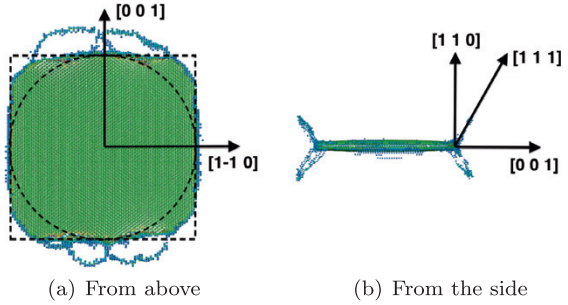

Fig. 7. (a) A closer look at Step 2 from Figs. 5 and 6 of the penny-shaped crack. This is the first crack extension event, taking place at angles ≈45° with respect to the coordinate axes, creating a square-shape. The original crack is shown by the dashed circle, and the dashed square is displayed in order to compare the crack with this shape. (b) The penny-shaped crack viewed from the side. Dislocations are emitted in $\langle 1\,1\,1\rangle$ directions from the $\langle 0\,0\,1\rangle$ tips of the crack, blunting the crack-tips in these directions.

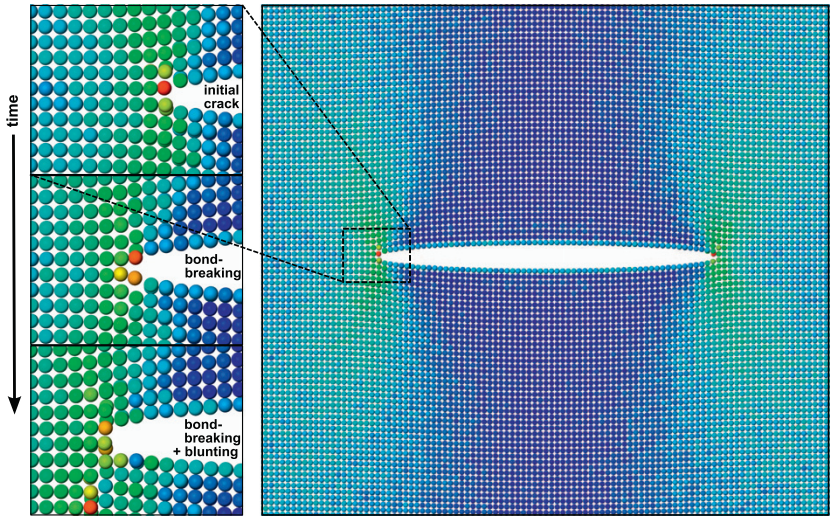

Fig. 8. Details of the crack-tip evolution in the directions ±45° relative to the coordinate axes in the {1 1 0} plane. First, a few atom bonds are broken, given rise to the change in shape from circular to square. Then, as larger parts of the crack front have access to the $\{2\,1\,1\}\langle 1\,1\,1\rangle$ slip system, dislocations reach this point and blunts the crack-tip.

advancing in these directions by bond breaking. As a result, the crack shape change from almost square to more six-edged, which is shown in Fig. 9a. We see that the dislocation loops now emit from the whole crack front, still in the $\{2\,1\,1\}\langle 1\,1\,1\rangle$ slip system, but with an edged crack front. Upon further straining of the system, dislocations continue to be emitted along the whole crack front. In Fig. 9b the viewport has been rotated and changed to perspective mode in order to clearly see the dislocation loops.

From the strain ε, Hooke's law is applied to find the stress $\sigma = E\varepsilon$. Using this stress and the initial crack radius a we calculate the stress intensity factor K_I

$$K_I = 2\sigma\sqrt{\frac{a}{\pi}} \tag{4}$$

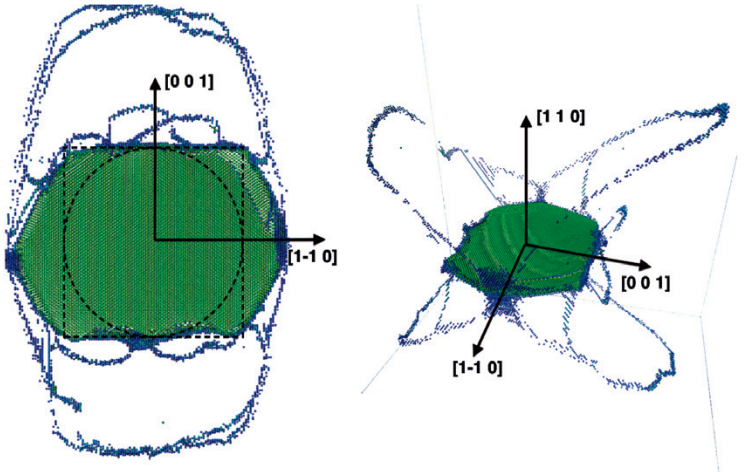

(a) From above (b) From the side

Fig. 9. (a) A closer look at Step 3 from Figs. 5 and 6, where the penny-shaped crack starts extending in $\langle 1\,1\,0\rangle$ directions on the $(1\,1\,0)$ crack plane, creating a six-edged crack shape. The dashed circle and square are displayed in order to compare with earlier stages of the crack evolution. (b) The same figure rotated and view in perspective mode, in order to clearly see the dislocation loops emitting in the $\{2\,1\,1\}\langle 1\,1\,1\rangle$ slip system.

Table 1
Calculated stress-intensity values and effective fracture energy from the strains of different events during the simulation.

Event	Strain (%)	Stress (MPa)	K_I (MPa $\sqrt{\text{m}}$)	γ_{eff} (N/m)
Extension at 45°	3.1	6930	0.72	1.06
First dislocations	3.2	7153	0.74	1.13
First extension in ⟨1 1 0⟩	3.5	7719	0.80	1.31

for a penny-shaped crack embedded in an infinite medium with an external applied stress [40]. The Young's modulus E used in these calculations is specific for the ⟨110⟩ loading direction, due to the anisotropic nature of iron, and it is found using the elastic constants C_{11}, C_{12} and C_{44} from the potential and the expression

$$\frac{1}{E} = S_{11} - 2\left[(S_{11} - S_{12}) - \frac{1}{2}S_{44}\right](l^2m^2 + m^2n^2 + l^2n^2) \tag{5}$$

from [41]. Here l, m and n are direction cosines for the different orientations, and S_{ij} are the compliance constants corresponding to the elastic constants. The stress intensities at different stages of the penny-shaped crack evolution are listed in Table 1.

When knowing the value of K_I, the energy release rate $\mathcal{G}$ can be found through the usual expression

$$\mathcal{G} = \frac{K_I^2}{E}(1 - \nu^2),$$

where the anisotropic value for E in the ⟨1 1 0⟩ direction is used, and a value of 0.3 is used for the Poisson ratio ν. Further, the energy release rate is linked to the effective fracture energy γ_{eff} via Eq. (3).

The calculated values for γ_{eff} are shown in Table 1. We see that all of these values lie *below* the theoretically predicted value of γ_s for the (1 1 0)-plane for brittle fracture in Fe, which is in the range of 1.4–1.6 N/m [24,36].

5. Constraint effects using multiscale modeling

Pioneering work on the influence of the elastic T-stress in atomistic modeling of bcc-Fe have been reported [42,43], where a central crack was embedded in a rectangular atomistic sample using Mode I and biaxial loading. Crystal orientations and crack sizes were examined as a function of T-stress. By varying the T-stress, a transition from dislocation nucleation to bond-breaking was observed as the T-stress changed from large negative to positive values.

In order to systematically examine the influence of the T-stress we introduce the *modified boundary layer* (*MBL*) *method* embedded in the *quasicontinuum* (*QC*) calculation procedure [44]. The MBL approach means that the analytic solution for the stress field around the crack-tip is applied as boundary conditions, and it has been extensively used in continuum fracture mechanics to examine the effect of constraint under controlled conditions. In this study, multiscale simulations have been performed using the MBL approach to test the effect of varying T-stress all the way down to the atomistic level. The QC

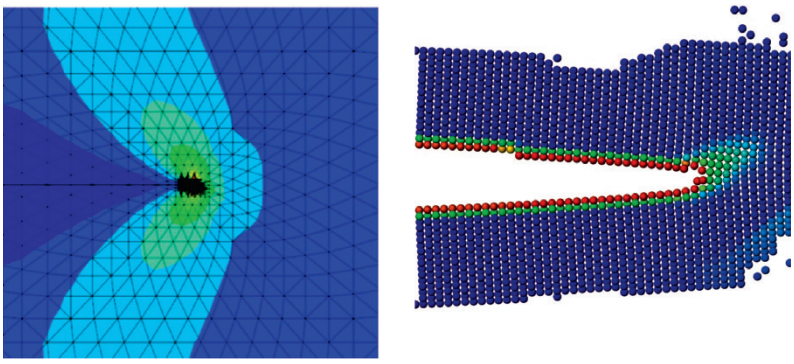

(a) The MBL model with the FE mesh, showing the von Mises stress. The crack tip is in the middle of the model.

(b) Zoom-in at the crack tip, visualizing atoms and nodes using the software Ovito [39].

Fig. 10. An overview of the MBL model simulated with the QC method. The nodes and atoms are colored by their strain energy density, ranging from low (blue) to high (red) values. (For interpretation of the references to colour in this figure legend, the reader is referred to the web version of this article.)

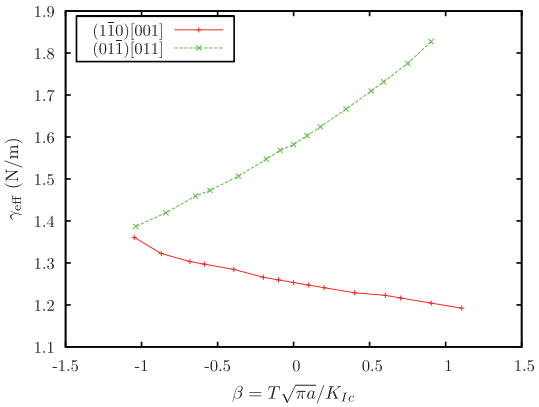

Fig. 11. The surface energy calculated from the stress intensity factor applied plotted against the *T*-stress for two crystallographic orientations. An almost linear relation is found between γ_{eff} and β in these orientations, but with different slopes.

method uses an atomistic description in areas, where high accuracy is needed (i.e. close to the crack tip), and a finite element description in the rest of the model. Fig. 10 gives an overview of the model that has been used, showing both the elements far away from the crack-tip and the atomistic region close to the crack-tip.

Results from the QC simulations are shown in Fig. 11, where the effective surface energy γ_{eff} calculated from the applied stress intensity factor is plotted against the *T*-stress (or rather the biaxiality ratio $\beta = T\sqrt{\pi a}/K_{Ic}$) for two crystallographic orientations. Orientation $(1\,\bar{1}\,0)[0\,0\,1]$ (notation referring to (crack plane) and [crack front direction]) gives brittle fracture on the $(1\,\bar{1}\,0)$ plane. This orientation shows a linear relationship between the surface energy and the *T*-stress, with γ_{eff} decreasing from about 1.35 to 1.2 N/m when β goes from -1.2 to +1.2. Orientation $(0\,1\,\bar{1})[0\,1\,1]$ also shows a linear dependency between γ_{eff} and *T*-stress, and the effect of constraint is even stronger than for orientation $(1\,\bar{1}\,0)[0\,0\,1]$. The critical event in orientation $(0\,1\,\bar{1})[0\,1\,1]$ is dislocation emission on the $\{1\,1\,2\}\langle 1\,1\,1\rangle$ slip system; no brittle fracture was observed. We see that the value of γ_{eff} is *increasing* from about 1.4 to 1.8 N/m when β increase from -1 to +1. The influence of the *T*-stress has been investigated further in [45].

6. Discussion and conclusion

We conclude that atomistic simulations will be a very useful tool in understanding the brittle-to-ductile transition in steels, i.e. the transition from bond-breaking to nucleation of dislocations.

The initial penny-shaped microcrack in our atomistic simulations revealed an interesting sequence of events in order to align the crack front with the most favorable crystallographic orientation for generating dislocations. The crack shape changed from circular to almost quadratic to allow for generation of dislocations in the $\{2\,1\,1\}\langle 1\,1\,1\rangle$ slip system. As the first loops of dislocations were emitted, the crack front further changed to a six-edged shape by bond breaking in $\langle 1\,1\,0\rangle$ directions on the original $\{1\,1\,0\}$ crack plane. This results in an extension of the first dislocation loops to cover almost the whole crack front, as seen in Fig. 9.

We observe that the resulting γ_{eff} for the above sequence of processes is lower than theoretically expected for brittle fracture, as presented in Section 3. What we see in the simulation is, however, *not* a brittle fracture, but rather very localized regions of *bond-breaking* in order to make the $\{2\,1\,1\}\langle 1\,1\,1\rangle$ slip system available to an ever increasing part of the crack front. The 3D nature of the penny-shaped crack enables a change in crack shape to find the "easiest" way to blunt and extend the original crack.

From the multiscale simulations using the QC method and MBL approach we found that the *T*-stress does indeed have an effect on the effective fracture energy γ_{eff} in two orientations relevant to our penny-shaped crack simulation. The $(1\,\bar{1}\,0)[0\,0\,1]$ orientation showed a linear *decrease* of effective surface energy as the biaxiality ratio β went from a negative to a positive value, with bond-breaking as the relevant fracture mechanism. Orientation $(0\,1\,\bar{1})[0\,1\,1]$ however, showed a linearly *increasing* γ_{eff} when β went from -1 to 1, with a larger absolute change in value than for the $(1\,\bar{1}\,0)[0\,0\,1]$ orientation. For the $(0\,1\,\bar{1})[0\,1\,1]$ orientation dislocation emission was the observed fracture mechanism.

Our multiscale and atomistic simulations are in agreement when it comes to crack mechanisms. The two orientations in the multiscale simulations correspond to the crack fronts situated along the *x*- and *z*-axes in the penny-shaped crack simulations. In $\{1\,1\,0\}\langle 0\,0\,1\rangle$ orientations we get bond-breaking in the crack-plane, and in $\{1\,1\,0\}\langle 1\,\bar{1}\,0\rangle$ orientations we get blunting of the crack-tip by dislocation emission in the $\{2\,1\,1\}\langle 1\,1\,1\rangle$ slip system.

The local critical stress level at initiation of cleavage fracture, σ_c, can be expressed as

$$\sigma_c = \sqrt{\frac{2E\gamma_{\text{eff}}}{Ca}}, \tag{6}$$

where E is the Young's modulus, γ_{eff} is the effective surface energy, a is the microcrack size and C is a numerical constant depending on the microcrack shape. According to the multiscale analyses above the critical stress intensity, and thus the effective surface energy, is a function of the T-stress level. Eq. (6) should then be modified to account for this by writing

$$\sigma_c = \sqrt{\frac{2E\gamma_{\text{eff}}(T)}{Ca}}, \tag{7}$$

where γ_{eff} is now a function of T-stress. Such a modification would represent an interesting way forward in coupling atomistic and continuum based approaches, and would represent important steps in reaching a multiscale approach in modeling of brittle fracture initiation in steels. It is recognized that the work presented here only represents a first step in conceptually outlining how this could be done, and several development steps would be needed for further progress. Despite this, this approach seems promising and could aid in arriving at more physics based approaches in modeling of cleavage fracture in steels.

Acknowledgements

We acknowledge the support from NTNU, the Research Council of Norway (Arctic Materials project supported through the Petromaks programme, Contract No.187389/S30) and the industry consortium behind the Arctic Materials project. Also the support from Norwegian High Performance Computing (NOTUR) with the generous computation quota and the support from Lars Eilertsen are highly acknowledged.

References

[1] Williams ML. On the stress distribution at the base of a stationary crack. J Appl Mech 1957;24:109–14.
[2] Zienkiewicz OC, Taylor RL. The finite element method for solid and structural mechanics. New York: McGraw-Hill; 1967.
[3] Zhang ZL, Thaulow C, Hauge M. Effects of crack size and weld metal mismatch on the has cleavage toughness of wide plates. Eng Fract Mech 1997;57(6):653–64.
[4] Thaulow C, Zhang ZL, Ranestad Ø, Hauge M. J–Q–M approach for failure assessment of fusion line cracks: two material and three material models. In: ASTM STP 1360, fatigue and fracture mechanics: 30th Volume, St. Louis, 1998.
[5] Thaulow C, Hauge M, Zhang ZL, Ranestad Ø, Fattorini F. On the interrelationship between fracture toughness and material mismatch for cracks located at the fusion line of weldments. Eng Fract Mech 1999;64(4):367–82.
[6] Dodds Jr RH, Anderson TL, Kirk MT. A framework to correlate a/W ratio effects on elastic-plastic fracture toughness (J_c). Int J Fract 1991;48:1–22.
[7] Kirk MT, Dodds Jr RH. An analytical and experimental comparison of J_i-values for shallow through and part-through surface cracks. Eng Fract Mech 1991;39(3):535–51.
[8] Sumpter J, Hancock J. Shallow crack toughness of HY80 welds: An analysis based on T stresses. Int J Press Vess Pip 1991;45(2):207–21.
[9] Tanaka M, Wilkinson AJ, Roberts SG. Ductile–brittle transition of polycrystalline iron and iron–chromium alloys. J Nucl Mater 2008;378:305–11.
[10] Tanaka M, Tarleton E, Roberts S. The brittle–ductile transition in single-crystal iron. Acta Mater 2008;56(18):5123–9.
[11] Spielmannová A, Landa M, Machová A, Haušild P, Lejček P. Influence of crack orientation on the ductile–brittle behavior in Fe-3 wt.% Si single crystals. Mater Charact 2007;58(10):892–900.
[12] Spielmannová A, Machová A, Hora P. Crack orientation versus ductile–brittle behavior in 3D atomistic simulations. Mater Sci Forum 2007;567–568:61–4.
[13] Prahl J, Machová A, Spielmannová A, Karlík M, Landa M, Haušild P, et al. Ductile-brittle behavior at the (1 1 0)[0 0 1] crack in bcc iron crystals loaded in mode I. Eng Fract Mech 2010;77(2):184–92.
[14] Pineau A. Modeling ductile to brittle fracture transition in steels – micromechanical and physical challenges. Int J Fract 2008;150:129–56.
[15] Sen D, Thaulow C, Schieffer SV, Cohen A, Buehler MJ. Atomistic study of crack-tip cleavage to dislocation emission transition in silicon single crystals. Phys Rev Lett 2010;104(23):235502.
[16] Thaulow C, Schieffer SV, Vatne IR, Sen D, Østby E. Crack tip opening displacement in atomistic modeling of fracture of silicon. Comput Mater Sci 2011;50(9):2621–7.
[17] Lambert-Perlade A, Sturel T, Gourgues A, Besson J, Pineau A. Mechanisms and modeling of cleavage fracture in simulated heat-affected zone microstructures of a high-strength low alloy steel. Metall Mater Trans A 2004;35:1039–53.
[18] Inglis CE. Stresses in a plate due to the presence of cracks and sharp corners. Trans Inst Naval Architects 1913;55:219–41.
[19] Griffith AA. The phenomena of rupture and flow in solids. Philos Trans, Ser A 1920;221:163–98.
[20] Irwin GR. Fracture dynamics. In: Fracturing of metals. Cleveland (OH): American Society for Metals; 1948. p. 147–66.
[21] Wells AA. Unstable crack propagation in metals: cleavage and fast fracture. In: Proceedings of the crack propagation symposium, Vol. 1, Cranfield (UK); 1961.
[22] Rice JR. A path independent integral and the approximate analysis of strain concentration by notches and cracks. J Appl Mech 1968;35:379–86.
[23] Shih CF. Relationship between the J-integral and the crack opening displacement for stationary and extending cracks. J Mech Phys Solids 1981;29:305–26.
[24] Gordon PA, Neeraj T, Luton MJ, Farkas D. Crack-tip deformation mechanisms in α-Fe and binary Fe alloys: an atomistic study on single crystals. Metall Mater Trans A 2007;38A:2191–202.
[25] Guo Y-F, Zhao D-L. Atomistic simulation of structure evolution at a crack tip in bcc-iron. Mater Sci Eng: A 2007;448(1–2):281–6.
[26] Hora P, Pelikán V, Machová A, Spielmannová A, Prahl J, Landa M, et al. Crack induced slip processes in 3D. Eng Fract Mech 2008;75:3612–23.
[27] Spielmannová A, Machová A, Hora P, stress Crack-induced. dislocations and acoustic emission by 3-D atomistic simulations in bcc iron. Acta Mater 2009;57(14):4065–73.
[28] Christopher D, Smith R, Richter A. Atomistic modelling of nanoindentation in iron and silver. Nanotechnology 2001;12(3):372.
[29] Njeim E, Bahr D. Atomistic simulations of nanoindentation in the presence of vacancies. Scripta Mater 2010;62(8):598–601.
[30] Domain C, Monnet G. Simulation of screw dislocation motion in iron by molecular dynamics simulations. Phys Rev Lett 2005;95(21):215506.
[31] Chaussidon J, Fivel M, Rodney D. The glide of screw dislocations in bcc Fe: Atomistic static and dynamic simulations. Acta Mater 2006;54(13):3407–16.
[32] Noronha SJ, Farkas D. Effect of dislocation blocking on fracture behavior of Al and α-Fe: a multiscale study. Mater Sci Eng A 2004;365:156–65.

[33] Heinisch H, Gao F, Kurtz R. Atomic-scale modeling of interactions of helium, vacancies and helium–vacancy clusters with screw dislocations in alpha-iron. Philos Mag 2010;90(7-8):885–95.
[34] Buehler MJ. Atomistic modeling of materials failure. Springer; 2008.
[35] Rice JR. Dislocation nucleation from a crack tip: an analysis based on the Peierls concept. J Mech Phys Solids 1992;40(2):239–71.
[36] Müller M, Erhart P, Albe K. Analytic bond-order potential for bcc and fcc iron – comparison with established embedded-atom method potentials. J Phys: Condens Mat 2007;19:326220.
[37] Plimpton SJ. Fast parallel algorithms for short-range molecular dynamics. J Comput Phys 1995;117:1–19.
[38] Ruda M, Farkas D, Garcia G. Atomistic simulations in the Fe–C system. Comput Mater Sci 2009;45(2):550–60.
[39] Stukowski A. Visualization and analysis of atomistic simulation data with OVITO – the open visualization tool. Modell Simul Mater Sci Eng 2010;18(1):015012.
[40] Murakami Y, editor. Stress intensity factors handbook, vol. 2. New York: Pergamon Press; 1987.
[41] Meguid SA. Engineering fracture mechanics. Elsevier Applied Science; 1989.
[42] Beltz GE, Machová A. Reconciliation of continuum and atomistic models for the ductile versus brittle response of iron. Modell Simul Mater Sci Eng 2007;15(2):65.
[43] Beltz GE, Machová A. Effect of T-stress on dislocation emission in iron. Scripta Mater 2004;50(4):483–7.
[44] Miller RE, Tadmor EB. The quasicontinuum method: Overview, applications and current directions. J Comput-Aided Mater Des 2002;9(3):203–39.
[45] Vatne IR, Østby E, Thaulow C, Farkas D. Quasicontinuum simulation of crack propagation in bcc-Fe. Mater Sci Eng: A 2011;528(15):5122–34.

Paper II

Atomistic modeling of penny-shaped and through-thickness cracks in bcc iron

Submitted to Modelling and Simulation in Materials Science and Engineering

Atomistic modeling of penny-shaped and through-thickness cracks in bcc iron

C H Ersland, I R Vatne, and C Thaulow

Department of Engineering Design and Materials, Norwegian University of Science and Technology (NTNU), NO-7491 Trondheim, Norway

E-mail: christer.h.ersland@ntnu.no

Abstract.

Atomistic simulations of penny-shaped embedded cracks in bcc iron are performed using molecular dynamics. The results reveal that the original circular crack geometry can change shape gradually upon loading, depending on the crystallographic orientation. This new geometry generally favors emission of dislocation loops instead of unstable fracture. Comparison is made between through-thickness cracks in six different orientations and penny-shaped cracks on the same crack planes. We find that changes in crack shape and the interaction of events in different directions play an important part in how fracture mechanisms evolve when cracks in full 3D simulations extend, and that dislocation emission and mechanical twins "win" over unstable crack-growth by bond-breaking.

1. Introduction

Iron and steels are materials of high importance to our society, and to understand how they crack and fail is essential to safely and sensibly utilize them in structures. After more than a century of research, the exact mechanisms leading to failure are still not fully understood, and as we now reach the atomic and sub-atomic scales, many secrets of materials behavior are uncovered.

α-iron is a body-centered cubic (bcc) metal, and for this type of structure we have several important possible deformation mechanisms. Slip in bcc occurs in $\langle 111 \rangle$ directions, which are the closest packed. The most common slip planes are $\{110\}$, $\{112\}$ and $\{123\}$ [1]. Twinning can also occur in bcc metals, and this usually happens on the $\{112\}$ planes in $\langle 111 \rangle$ directions. There is an increased tendency for twinning to occur with increasing deformation rate and decreasing temperature. The above slip systems are also found experimentally to be the most active in pure iron and low-alloy steels [2, 3]. In experiments, $\{100\}$ planes are most common to cleave, but also $\{110\}$, $\{112\}$ and $\{123\}$ planes produce cracks [4]. Theoretically favored cleavage planes in bcc, due to ranking of surface energies, are the $\{110\}$, $\{100\}$ and $\{112\}$ planes [5].

During the last decades many investigations of Mode I loading of cracks in α-iron on the atomistic level have been performed. Various crack orientations have been examined, but the most thoroughly studied are cracks on $\{110\}$ and $\{100\}$ planes with different crack front directions. In the following, (...) and $\{...\}$ denote crack planes, while [...] and $\langle ... \rangle$ denote the *crack front direction* (normal to the crack growth direction).

The (110) plane was studied by Shastry and Farkas [6] by embedding a central crack on this plane in a cylindrical simulation cell at 0 K. Crack front directions [100], [110] and $[1\bar{1}1]$ were tested, and an embedded atom method (EAM) potential was used in the simulations. With a [100] crack front the crack extended in a brittle manner, while for [110] and $[1\bar{1}1]$ fronts dislocations were emitted in $\{112\}\langle 111\rangle$ and $\{110\}\langle 111\rangle$ slip systems, respectively. This clearly showed evidence for ductile response for cracks on a (110) plane, even at 0 K.

Hora et al. [7] simulated two cracks on a (001) plane at temperatures of 0 K and 300 K using an N-body Finnis-Sinclair (F-S) potential. A central (001)[010] crack was found to extend in a brittle manner at 0 K, but at 300 K slip occured on $\{101\}$ planes at angles $\pm 45°$ in front of the crack-tip and, at higher loads, on $\{112\}$ planes at angles $\pm 26.565°$. For a (001)[110] edge crack there was also some crack extension, followed by twinning in $\{112\}\langle 111\rangle$ slip systems – the so called "easy twinning" directions located at $\pm 35.26°$ with respect to the crack plane.

A (001)[110] crack was also simulated by Machová and Beltz [8] using an F-S potential at 0 K – here they got crack extension by bond-breaking along the original crack plane. Two crack lengths were tested, and while the longest showed pure cleavage, the shortest produced twinning in the "easy twinning" slip system $\{112\}\langle 111\rangle$, accompanying a slow, subcritical crack growth. This suggests that twinning is an important mechanism responsible for slowing down cracks, and that T-stress levels resulting from shorter crack lengths will reduce the critical shear stress needed for twin formation. Guo et al. [9] also found twinning in this orientation at low temperatures.

Five crack configurations were examined by Gordon et al. [10] comparing four recently developed F-S and EAM potentials at 0 K, and a high sensitivity to crack orientation was found. Cracks with $\{001\}\langle 110\rangle$ and $\{110\}\langle 001\rangle$ orientations produced brittle fracture in all cases, while $\{110\}\langle 110\rangle$ and $\{111\}\langle 112\rangle$ orientations resulted in a ductile behavior in all cases but one (the $\{110\}\langle 110\rangle$ produced brittle behavior using one of the EAM potentials tested). The dislocations were emitted in the $\{112\}\langle 111\rangle$ slip system for the $\{110\}\langle 110\rangle$ crack and in the $\{110\}\langle 111\rangle$ slip system for the $\{111\}\langle 112\rangle$ crack. One of the potentials also resulted in a dislocation being emitted in the $\{123\}\langle 111\rangle$ slip system for the $\{111\}\langle 112\rangle$ crack. The last orientation tested was $\{111\}\langle 112\rangle$, where twinning at $-90°$ was observed together with small crack growth on a $\{110\}$ plane, at an angle 35.3° with respect to the original crack plane.

In a recent publication by Vatne et al. [11] some of the same orientations as the publications above were simulated using the *quasicontinuum (QC) method* with an EAM potential. For crack orientations (010)[101] and $(1\bar{1}0)[001]$ crack propagation within the original crack plane was observed, accompanied by blunting of the crack-tip and bcc $\rightarrow$ fcc transformation in a region close to the crack-tip. The same type of events occurred also with a (010)[001] orientation, but now the crack started growing on a $(1\bar{1}0)$ plane, 45° with respect to the original crack plane. A $(01\bar{1})[011]$ crack was also tested, and they observed dislocations in a $\{112\}\langle 111\rangle$ slip system, in accordance with [6, 10]. A systematic investigation of the influence of T-stress was also performed, together with isotropic versus anisotropic boundary conditions with a modified boundary layer (MBL) approach.

Some studies take into account elevated temperatures and the brittle-to-ductile (BDT) transition, e.g. [12, 13, 14]. The main result from these examinations is that the material deforms more easily and the crack-tip blunts more when the temperature increases, and that a transition from brittle to ductile behavior can be shown using

molecular dynamics, at least for the orientations tested in these references. Also, there is a greater tendency for twinning and stacking faults at low temperatures, which seem to favor bond breaking at the crack-tip.

Common for all the simulations mentioned above is that they consider straight crack fronts, making the modeled systems effectively two-dimensional, or semi-three-dimensional. Real cracks in metals are, however, not straight, and this three-dimensional nature should be taken into account when studying fracture mechanisms and predict how the materials fail.

Several authors have studied the nucleation and/or evolution of *voids* in metals, which is a 3D problem, but most of these are fcc materials like copper [15, 16, 17, 18, 19] and nickel [20] and the ones for bcc materials are for tantalum [21, 22], vanadium, niobium, molybdenum and tungsten [23] – not iron. To our knowledge no one else has previously studied penny-shaped cracks using molecular dynamics. We believe it is important to study this geometry as it could model typical brittle particles within a material, where the initial crack might be flat and semi-circular. Since the initial crack is circular it has access to all possible growth directions – the crack can choose which direction(s) to extend depending on which wins the competition between different energetically favorable possibilities of cleavage, slip, twinning, phase transformation and dislocation emission.

2. Computational methods

All simulations have been performed using the molecular dynamics software LAMMPS [24] run on a supercomputer. The potential used for the simulations is the iron part of the EAM potential by Ruda et al. [25], which is nothing but the so-called "extended Mendelev II" [26] that builds upon the original "Mendelev II" potential [27]. The Mendelev potential is one of the very few to correctly predict the sixfold symmetry of screw dislocation cores, as calculated by DFT calculations [28, 29], so we choose this since screw dislocations are known to be important in the plasticity of bcc metals.

Two different specimen geometries have been investigated: a through-thickness crack and an embedded penny-shaped crack, both depicted in Figure 1. Simulations have been performed with the crack located on three crystallographic planes, namely the {100}, {110} and {111} planes of the iron bcc lattice. In the through-thickness specimen, two orientations of the crack front has been studied for each of the three crack planes, in order to see the effect this has on the crack mechanisms. In the penny-shaped crack specimen, however, only one simulation has been run on each crack plane, since the circular embedded crack has access to all crack growth directions and can grow in whichever direction is energetically favorable. In Table 1 an overview of all the tested orientations is given, together with an overview of favorable cleavage planes and twinning/slip systems in the different cases.

The through-thickness cracks all have a half-length a of about 60 Å, and the penny-shaped cracks correspondingly have a radius a of approximately 60 Å. All specimens have lengths L in x- and y-directions of about 600 Å. The through-thickness specimens have a thickness of only three lattice unit cells in the z-direction, so this is only a "semi-3D" system. The penny-shaped cases, on the contrary, are 600 Å also in the z-direction, making them full 3D simulations. These configurations result in simulations with approximately $400,000$ atoms for the through-thickness cases and approximately 18.5 million atoms in the penny-shaped cases. The initial cracks are introduced by *switching off* the interactions between two regions of atoms, thus

Table 1. Overview of possible slip systems, twin directions and preferred cleavage planes in the orientations considered in the simulations. The angle given is the angle between the initial crack plane and the cleavage plane/slip system in question, normal to the crack front direction.

No.	Crack orientation (plane)[front direction]	System/plane	Type	Angle (deg)
1	(010)[101]	(010)	cleavage	0
		$\{112\}\langle 111\rangle$	twin/slip	± 35.3
2	(010)[001]	(010)	cleavage	0
		(110)	cleavage	± 45
3	(110)[001]	(110)	cleavage	0
4	(110)[$\bar{1}$10]	(110)	cleavage	0
		$\{112\}\langle 111\rangle$	twin/slip	± 54.7
		$\{112\}\langle 111\rangle$	twin/slip	± 125.3
5	(111)[$\bar{1}\bar{1}$2]	$\{110\}\langle 111\rangle$	slip	± 90
6	(111)[$\bar{1}$10]	(110)	cleavage	35.3
		$\{112\}\langle 111\rangle$	twin/slip	± 90

creating atomistically sharp cracks.

The systems are periodic in all directions in order to prevent free surfaces, and they are loaded in Mode I normal to the crack plane by linearly rescaling the system length in y-direction according to a strain rate of $5 \cdot 10^8$ s^{-1}. The deformation is performed with a time-step size of 1 fs until the systems are strained about 8 %. Before any deformation is applied, the systems are relaxed at 1 K with zero pressure in all directions until a stable state is reached. During deformation the systems are also kept at 1 K, and with zero pressure applied in the crack plane directions.

3. Results

This section is divided as follows: first the crack mechanisms in the through-thickness cracks are presented; then the effects of different crystallographic orientations of the penny-shaped cracks are described. All figures from the simulations are produced using the Open Visualization Tool (OVITO) [30], and coloring of atoms is due to common neighbor analysis (CNA) [31, 32].

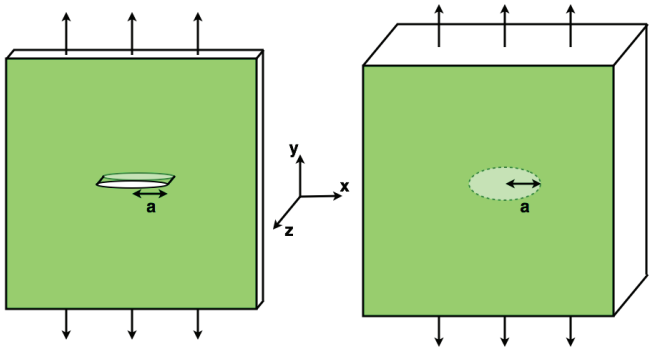

Figure 1. Simulated systems: through-thickness crack (left) and penny-shaped embedded crack (right), both loaded in Mode I.

Table 2. Through-thickness crack – overview of the first events to take place in the orientations considered. The type of mechanism, the strain when the mechanism is first observed and the calculated K_I values are given.

No.	Crack orient. (plane)[front dir.]	System/plane	Mechanism	Strain (%)	K_I (MPa$\sqrt{\text{m}}$)
1	(010)[101]	(010)	fcc formation	3.8	0.80
		$\{112\}\langle 111\rangle$	twinning	4.4	0.91
2	(010)[001]	(010)	fcc formation	4.2	0.88
		(110)	bond-breaking	5.4	1.09
3	(110)[001]	(110)	fcc formation	3.4	0.94
		(110)	bond-breaking	4.3	1.15
4	(110)[$\bar{1}$10]	$\{112\}\langle 111\rangle$	dislocation	3.4	0.94
5	(111)[$\bar{1}\bar{1}$2]	$\{110\}\langle 111\rangle$	dislocation	3.6	1.04
6	(111)[$\bar{1}$10]	(110)	bond-breaking	3.2	0.97
		$\{112\}\langle 111\rangle$	twinning	3.4	1.00
		$\{112\}\langle 111\rangle$	dislocation	4.3	0.97

3.1. Simulations of through-thickness cracks

Fracture mechanisms for through-thickness cracks on three crack planes are studied. Two crack front directions are chosen for each crack plane, corresponding to interesting crack directions to compare with the penny-shaped crack simulations. All figures show only one tip of the through-thickness crack in order to study the mechanisms more closely, yet the whole system has two crack fronts which show the same kind of mechanisms. Stress – strain curves for all the through-thickness crack simulations are shown in Figure 2, where stress is calculated as the negative of the p_{yy} pressure tensor component from the simulations, and strain is calculated from the current time-step multiplied by the strain rate. Also, Table 2 gives an overview of the first events and mechanisms for each orientation, together with the strain as well as the stress-intensity at which the event takes place. The strain is calculated from the current time-step multiplied by the strain rate, while the Mode I stress-intensity K_I is calculated from the standard expression for a through-thickness crack [33],

$$K_I = \sigma\sqrt{\pi a} \tag{1}$$

where σ is the stress at the strain of the event, read from the stress – strain curve, and a is the half crack-length.

3.1.1. Orientations on the (100) *crack-plane* The behavior changes quite drastically with crack front orientation, as seen in Figure 3. In the (010)[101] orientation (Figure 3(a)) fcc structure is created at approximately 35.3° close to the crack-tip at a strain of 3.8%, followed by twinning in the same direction starting at a strain of about 4.4%. This corresponds to the point of the stress – strain curve where the stress flattens out and start to decrease (see Figure 2). The twinning occur on a (121)-plane, which is an expected twin/slip plane in bcc [34]. At later stages of the loading the crack extends slightly (3-4 broken atom bonds), but at this point the twinned regions have reached the boundaries of our system and might influence the crack behavior.

The (010)[001] orientation (Figure 3(b)) also shows formation of fcc structure - the first sign of fcc is at a strain of about 4.2%. In this case, however, the fcc regions are symmetrically placed ±45° with respect to the crack-plane, on {110} planes, and

no twinning is observed. The fcc regions extend, first in length but later also in width, as the loading is increased. Looking at the stress – strain curve in Figure 2, the slope starts deviating from its linear trend at about the same time as the fcc formation starts, and the curve starts flattening out at about 5.2% strain, which is when the fcc regions starts to get wider.

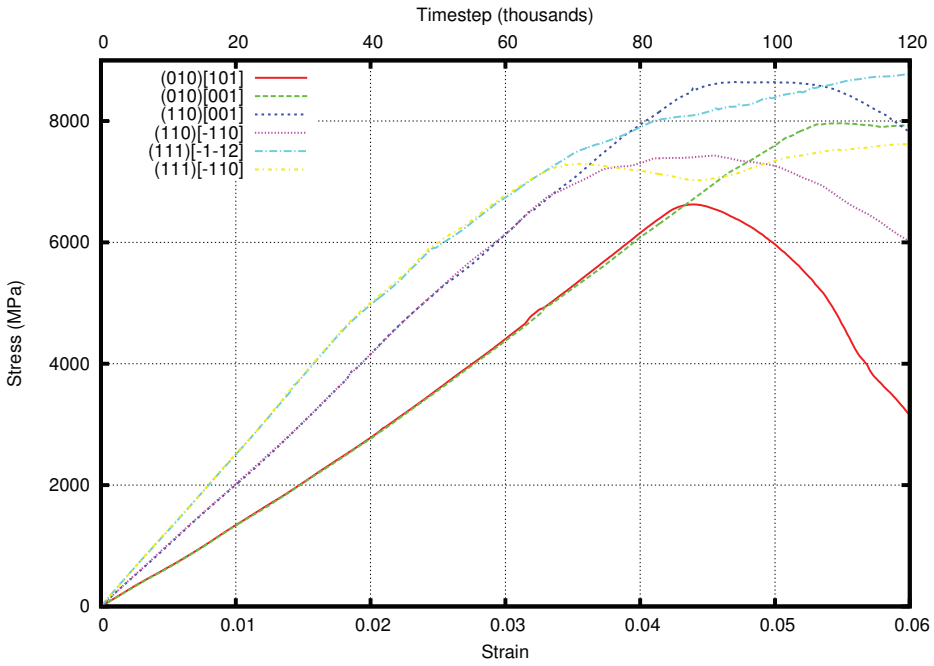

Figure 2. Stress – strain curves for all six orientations in the through-thickness crack simulations. Stress is calculated as the negative of the p_{yy} pressure tensor component from the simulations, and strain is calculated from the current time-step multiplied by the strain rate. (Color online.)

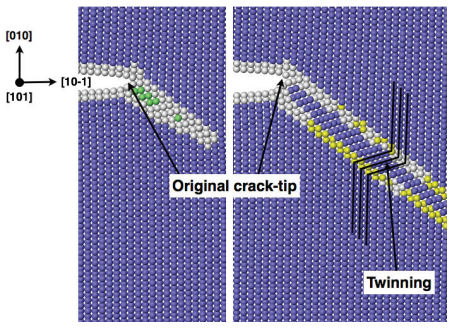

(a) The (010)[101] crack.

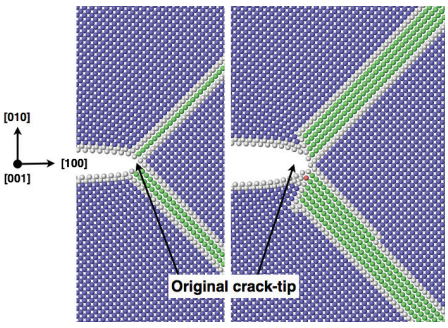

(b) The (010)[001] crack.

Figure 3. The two through-thickness cracks simulated in the (010)-plane. Atoms colored due to CNA, where blue is bcc, green is fcc, yellow is bcc twin and white is unknown structure. (Color online.)

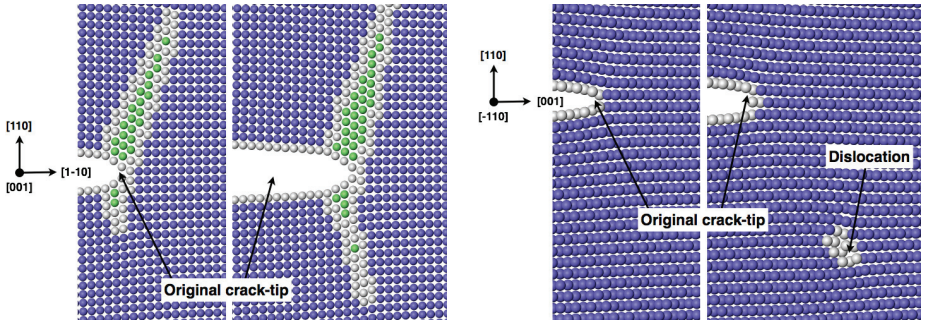

(a) The (110)[001] crack. (b) The (110)[$\bar{1}$10] crack.

Figure 4. The two through-thickness cracks simulated in the (110)-plane. Atoms colored due to CNA, where blue is bcc, green is fcc, yellow is bcc twin and white is unknown structure. (Color online.)

3.1.2. Orientations on the (110) *crack-plane* The (110)[001] orientation (Figure 4(a)) produce crack extension through bond-breaking, starting at a strain of about 4.3%. Both before and during crack extension there are regions of fcc almost perpendicular to the crack-plane, and these regions follow the crack as it grows. The first sign of fcc is seen at a strain of about 3.4% – from a size of only a few atoms, the fcc regions grow until the crack starts growing, and they continue to grow further as they follow the crack-tip through the material.

The (110)[$\bar{1}$10] crack orientation (Figure 4(b)) does not result in crack extension, but rather blunts the crack-tip by emitting edge dislocations in the $\{112\}\langle 111\rangle$ slip system, starting at a strain of 3.4 %. This corresponds very well with the stress – strain curve in Figure 2, where we see a noticeable change in the slope of the curve as this strain is reached. As loading continues, more dislocations are emitted in this slip system, at angles $\pm 54.7^\circ$ with respect to the crack plane, and the stress – strain curve continues to flatten out and finally decrease. No fcc formation or twinning occurs in this orientation.

3.1.3. Orientations on the (111) *crack-plane* The (111)[$\bar{1}\bar{1}$2] system (Figure 5(a)) has a $\{110\}\langle 111\rangle$ slip system available at $\pm 90^\circ$ with respect to the crack plane, and this is exactly where we observe emission of dislocations in this case, starting at a strain of 3.6 %. No crack extension, fcc formation or twinning occurs in this orientation – only edge dislocations are emitted and the crack-tip blunts.

The last through-thickness crack orientation investigated, (111)[$\bar{1}$10] (Figure 5(b)), reveals a more complex fracture behavior. Here we first observe crack growth *away* from the original crack plane, then twinning and finally dislocation emission. The crack starts growing away from the original crack plane at a strain of 3.2 %, on the (110)-plane, shown to the left in Figure 5(b). As the crack grows a twinning region is formed around the crack tip in a direction normal to the original crack plane, as shown from left to right in Figure 5(b). At a strain of about 4.4 % the crack extension stops, and edge dislocations are now emitted from the crack tip. As loading continues more dislocations are emitted, and they all go in the opposite direction of the twinning, in a $\{112\}\langle 111\rangle$ slip system. As the crack moves away from the original crack plane, the situation becomes the same as the (110)[$\bar{1}$10] crack orientation (Figure

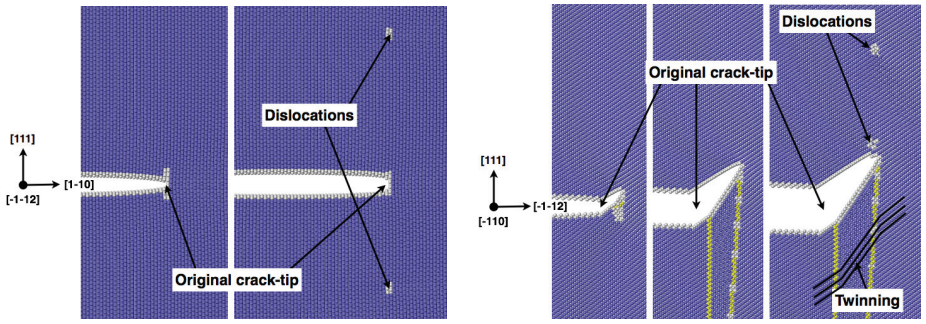

(a) The (111)[$\bar{1}\bar{1}2$] crack. (b) The (111)[$\bar{1}10$] crack.

Figure 5. The two through-thickness cracks simulated in the (111)-plane. Atoms colored due to CNA, where blue is bcc, green is fcc, yellow is bcc twin and white is unknown structure. (Color online.)

4(b)), except that the loading is now a mix between Mode I and II for the crack-tip. The dislocations follow the same slip system as they did in the (110)[$\bar{1}10$] case, which is as expected. When looking at the stress – strain curve in Figure 2, we can actually see the stress decreasing when the crack extends, before flattening out and slowly increasing when dislocation emission starts.

3.2. Simulations of penny-shaped cracks

Penny-shaped cracks located on three crack planes have been studied, and fracture mechanisms at the initial stages of crack extension are presented in this section. Stress – strain curves for all the through-thickness crack simulations are shown in Figure 6. Also, Table 3 gives an overview of the first events and mechanisms for each crack plane, together with the strain as well as the stress-intensity at which the event takes place. The strain is calculated from the current time-step multiplied by the strain rate, while the Mode I stress-intensity K_I is calculated from the standard expression for a penny-shaped crack [33],

$$K_I = \frac{2}{\pi}\sigma\sqrt{\pi a} \tag{2}$$

where σ is the stress at the strain of the event, read from the stress – strain curve, and a is the crack radius.

3.2.1. The (100) *crack-plane* When loading the penny-shaped crack normal to a {100} plane, the first event to happen is that the crack goes from circular to almost quadratic. The crack does not extend at all in the ⟨100⟩ directions during this period, but grows in the ⟨110⟩ directions by bond-breaking, creating "corners" of the crack as shown in Figure 7(a). After fully straightening the crack fronts along ⟨100⟩ directions, the crack does not keep its straight crack fronts, and it also grows slightly out of the original plane. This more "messy" crack growth happens, however, after the point where we can no longer neglect boundary effects, as the region containing high-energy non-bcc atoms has reached our system boundaries. A full overview of the regions with non-bcc atoms is shown in Figure 7(b).

In order to study the crack tip mechanisms more closely, two cuts have been made to view the same orientations as in the through-thickness crack case, see Figure

Table 3. Penny-shaped crack – overview of the first events to take place in the orientations considered. The type of mechanism, the strain when the mechanism is first observed and the calculated K_I values are given.

Crack plane	System/plane	Mechanism	Strain (%)	K_I (MPa$\sqrt{\text{m}}$)
(100)	(100)	fcc formation	4.8	0.80
	$\{112\}\langle 111\rangle$	twinning	6.0	0.91
(110)	$\{112\}\langle 111\rangle$	dislocation	4.7	0.88
	(110)[001]	bond-breaking	4.95	1.09
(111)	(110)$[\bar{1}10]$	bond-breaking	5.5	0.94
	(111)$[\bar{1}\bar{1}2]$	bond-breaking	5.6	1.15
	$\{110\}\langle 111\rangle$	dislocation	5.7	0.94
	$\{112\}\langle 111\rangle$	dislocation	5.8	1.04

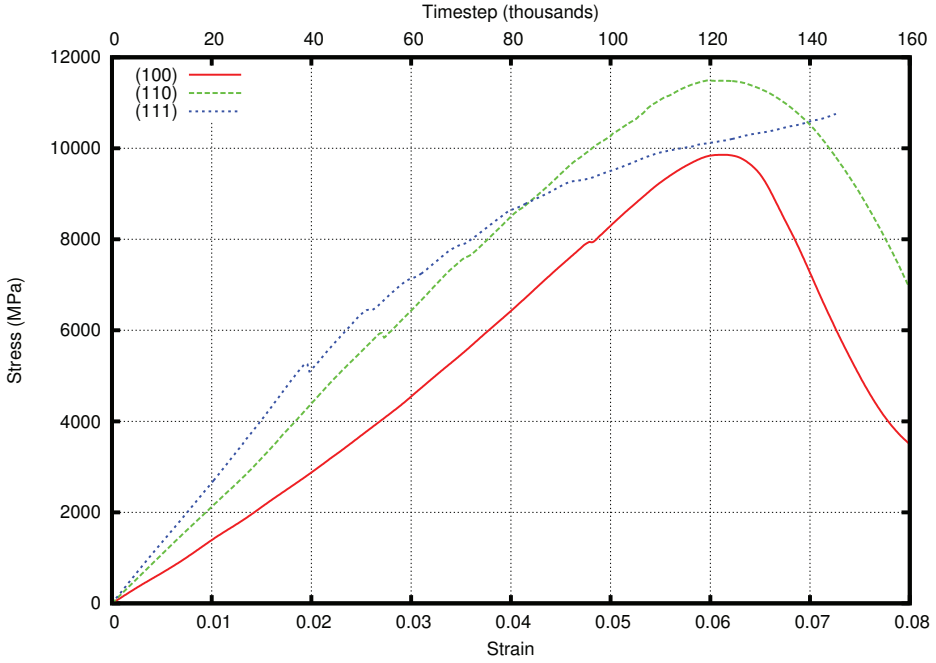

Figure 6. Stress – strain curves for the three crack plane orientations in the penny-shaped crack simulations. Stress is calculated as the negative of the p_{yy} pressure tensor component from the simulations, and strain is calculated from the current time-step multiplied by the strain rate. (Color online.)

8. To the left, in Figure 8(a), the (010)[101] crack system is depicted, and we see that a region of fcc atoms appears in front of the crack tip. This happens at a strain of about 5.2 %, right before the crack extends straight ahead by breaking 3-4 atom bonds. After this small crack extension, regions of non-bcc atoms form symmetrically in front of the crack at about $\pm 35.3°$ – regions that turn into pure twinning at about 6.0 % strain. This corresponds to the point on the stress – strain curve (Figure 7(a)) where the stress drops rapidly.

Figure 8(b) shows the (010)[001] system, where we observe fcc formation symmetrically at $\pm 45°$ in front of the crack tip, starting at about 5.3 % strain. As

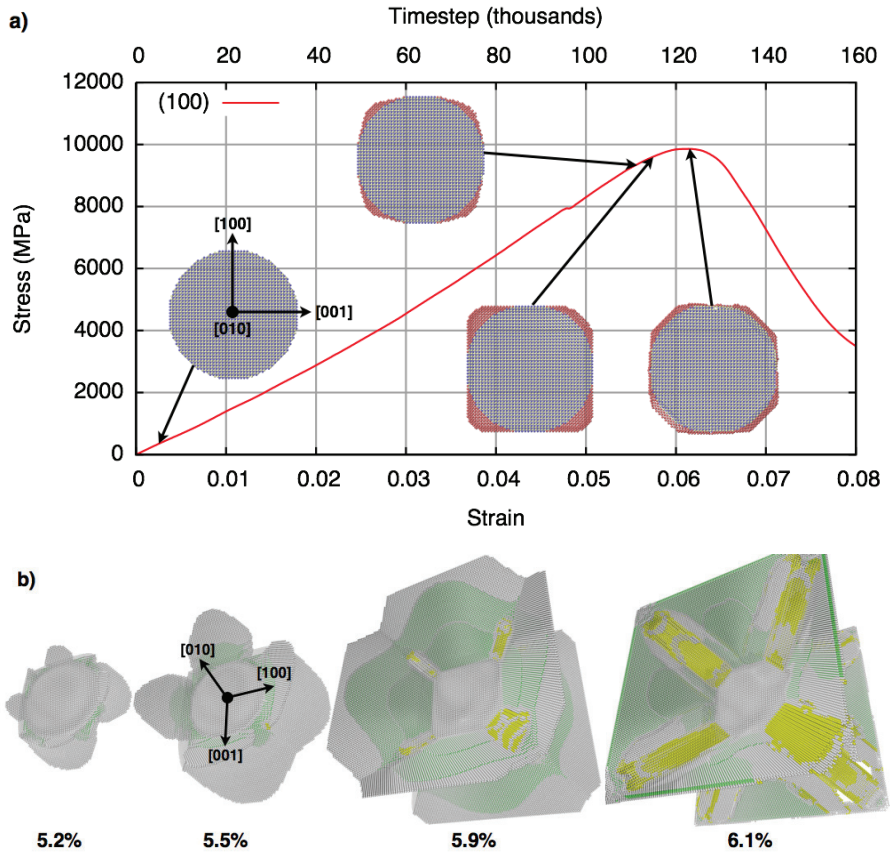

Figure 7. Evolution of the penny-shaped crack in the case with loading normal to a {100} plane, with increasing strain (in percentage) denoted under each figure. In a) the stress – strain curve for the simulation is shown, together with the crack shape at selected points. The blue atoms show the initial crack, and the red atoms show where the crack has grown. b) shows only non-bcc atoms at selected strain values. Formation of fcc structure is seen, as well as twinning in the corners when the fcc regions meet. Atoms colored due to CNA, where green is fcc, yellow is bcc twin and white is unknown structure. (Color online.)

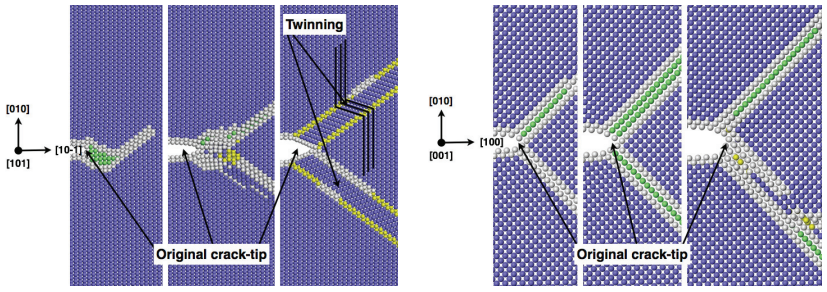

(a) A (010)[101] cut.

(b) A (010)[001] cut.

Figure 8. Cuts through the penny-shaped crack simulated on the (100)-plane. Atoms colored due to CNA, where blue is bcc, green is fcc, yellow is bcc twin and white is unknown structure. (Color online.)

loading continues the fcc regions get slightly broader, and stretches further out in the sample. The crack never grows in this direction, but at 6.0 % strain it suddenly blunts, and the fcc regions turn into a mixture dominated by fcc and twin regions. Again, this happens at the point on the stress – strain curve (Figure 7(a)) where the stress drops rapidly.

3.2.2. The (110) *crack-plane* The crack on the (110)-plane exhibits a mixture of crack extension, dislocations, fcc formation and twinning, see Figure 9(b). Dislocation loops are emitted in $\{112\}\langle 111\rangle$ slip systems symmetrically on both sides of the original crack-plane, resembling butterfly wings (see Figure 10). The loops consist of an edge

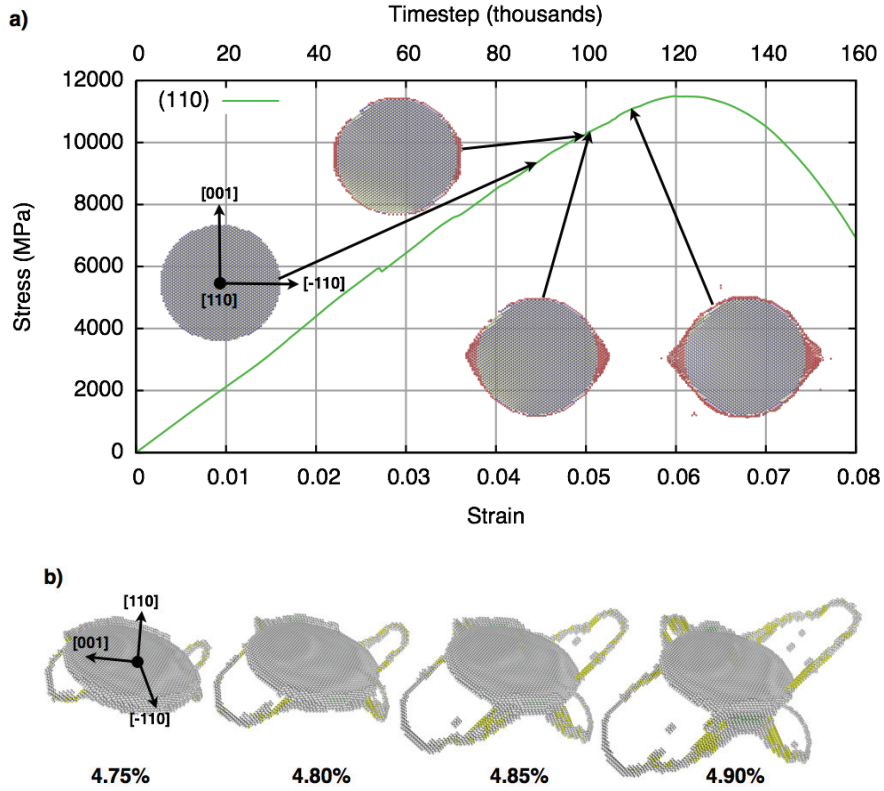

Figure 9. Evolution of the penny-shaped crack in the case with loading normal to a {110} plane, with increasing strain (in percentage) denoted under each figure. In a) the stress – strain curve for the simulation is shown, together with the crack shape at selected points. The blue atoms show the initial crack, and the red atoms show where the crack has grown. b) shows only non-bcc atoms at selected strain values. Crack extension happens in the $[1\bar{1}0]$ and $[\bar{1}10]$ directions, while edge dislocation loops are emitted in $\{112\}\langle 111\rangle$ slip systems at an angle $\pm 54.7^\circ$ with respect to the crack plane, and they have screw dislocations on the sides. The dislocations move normal to the crack plane, and the loops follow the crack-tip around the circular crack until they meet each other. As the edge and screw dislocations move away from the crack, they leave twinning (yellow) and debris behind in the bcc structure. Atoms colored due to CNA, where green is fcc, yellow is bcc twin and white is unknown structure. (Color online.)

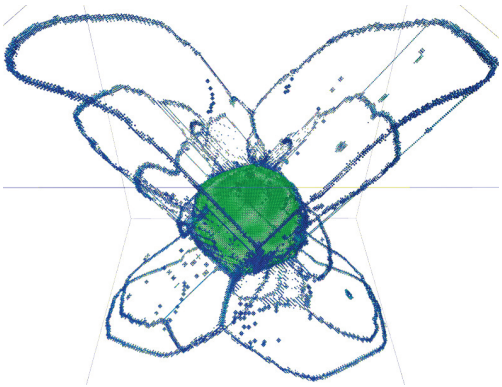

Figure 10. Snapshot from a simulation of the penny-shaped crack in a {110} plane, clearly showing how the dislocation loops emitted in $\{112\}\langle 111\rangle$ slip systems resemble butterfly wings. The coloring of the atoms is done due to von Mises stress, where blue is low and green is high stress, respectively. (Color online.)

dislocation front following the $\{112\}\langle 111\rangle$ slip system, screw dislocation sides and mixed dislocations connecting them. The originally circular crack extends slightly, changing its shape to an octagon. Edge dislocations are then emitted from the $\langle 011\rangle$ crack fronts and screw dislocations from the $\langle 111\rangle$ fronts of the octagon. The crack then grows further, turning the octagon into a hexagon. This is happening as the screw dislocations emitted from the $\langle 111\rangle$ crack front, moving on the $\{112\}\langle 111\rangle$ slip system, turns into twinning as the stress increases. The twinning is also in the $\{112\}\langle 111\rangle$ slip system, and is going from the dislocation loop down to the crack plane. This causes the crack to grow so that the crack front is the intersection vector, which will be $\langle 011\rangle$ directions. Both the screw and edge dislocation parts of the loops are gliding, but the edge dislocations are moving faster than the screw dislocations. An overview of the evolution of non-bcc regions due to increasing strain is shown in Figure 9(b).

Figure 11 shows two slices through the penny-shaped crack, corresponding to the through-thickness orientations. In the (110)[001] crack system, Figure 11(a), we observe some crack growth combined with a region of fcc almost normal to the crack

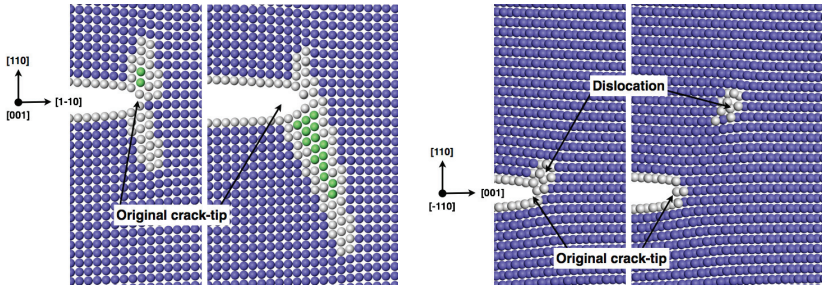

(a) A (110)[001] cut. (b) A (110)[$\bar{1}$10] cut.

Figure 11. Cuts through the penny-shaped crack simulated on the (110)-plane. Atoms colored due to CNA, where blue is bcc, green is fcc, yellow is bcc twin and white is unknown structure. (Color online.)

plane. The crack starts growing at a strain of about 4.95 %, right after the first sign of fcc formation. After crack growth by the breaking of 6-7 atom bonds the crack stops again and the fcc regions disappear and are replaced by twinning.

For the (110)[$\bar{1}$10] orientation, Figure 11(b), we see dislocation emission in the {112}⟨111⟩ slip system, starting at a strain of 4.7 %. Several dislocations are emitted as loading continues, at angles ±54.7° with respect to the crack plane. Looking at the stress – strain curve in Figure 9(a) we can see the curve starting to flatten around the point of the first dislocation, and continuing this trend as more dislocations are emitted later in the simulation.

3.2.3. The (111) *crack-plane* In the case of loading normal to the {111} crack-plane, almost no crack extension happens. Instead, dislocations looking like smoke-rings (see Figure 12) are produced all along the crack front, moving in the loading direction (see Figure 13(b)). No dislocations appear until a strain of 5.7 % is reached, but after the first dislocation is generated more are released in discrete bursts. Before the first dislocation is emitted, the circular crack-front straightens slightly along six ⟨110⟩ directions in the crack-plane, thus enabling dislocation emission in {110}⟨111⟩ slip systems. The crack fronts are all ⟨112⟩, and the dislocations are therefore emitted on {110} planes in ⟨111⟩ directions.

Two slices through the penny-shaped crack are shown in Figure 14. Figure 14(a) shows the (111)[$\bar{1}\bar{1}$2] crack orientation which produces edge dislocation emission normal to the crack-plane. This corresponds to the {110}⟨111⟩ slip system, as explained above. Dislocations are emitted both in the upwards and downwards directions, with several released as loading increases. Right before the first dislocation is emitted, the crack-tip advances by the breaking of 4-5 atom bonds, at a strain of about 5.6 %. At 5.7 % strain the crack stops, and at the same time the first dislocation is emitted.

The final cut through the penny-shaped crack is the (111)[$\bar{1}$10] orientation (Figure

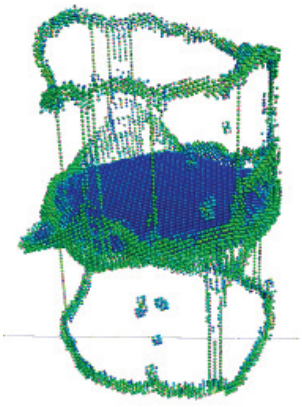

Figure 12. Snapshot from a simulation of the penny-shaped crack in a {111} plane, visualizing how the dislocation loops emitted normal to the original crack plane resemble smoke-rings sent out in discrete bursts. The coloring of the atoms is done due to von Mises stress, where blue is low and green is high stress, respectively. (Color online.)

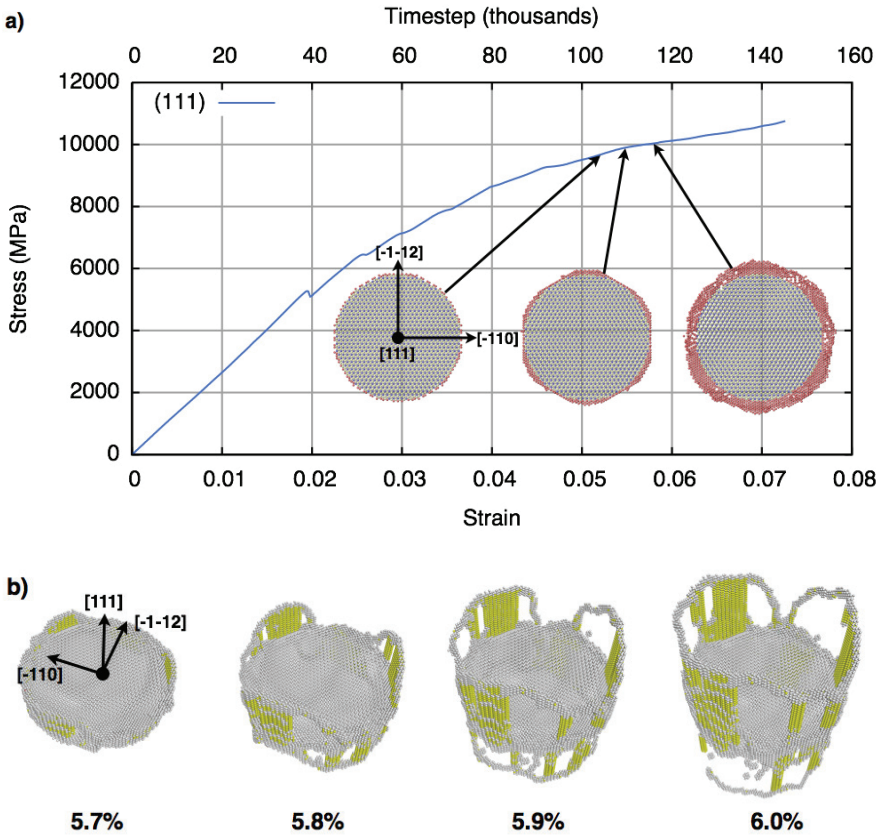

Figure 13. Evolution of the penny-shaped crack in the case with loading normal to a {111} plane, with increasing strain (in percentage) denoted under each figure. In a) the stress – strain curve for the simulation is shown, together with the crack shape at selected points. The blue atoms show the initial crack, and the red atoms show where the crack has grown. b) shows only non-bcc atoms at selected strain values. We observe how the edge dislocation loops begin emitting in $\{110\}\langle 111\rangle$ slip systems, with screw dislocations on the sides. The dislocations move normal to the crack plane, and the loops follow the crack-tip around the circular crack until they meet each other. As the edge and screw dislocations move away from the crack, they leave twinning bands (yellow) and debris behind in the bcc structure. Atoms colored due to CNA, where green is fcc, yellow is bcc twin and white is unknown structure. (Color online.)

14(b)). Here we observe crack extension away from the original crack-plane starting at 5.5 % strain, following a (110)-plane. After extension by the breaking of 8-9 atom bonds in the crack growth direction, the crack stops at a strain of 5.8 % – immediately followed by the emission of an edge dislocation normal to the original crack plane. This again corresponds to a mixed-mode case with the crack-tip now in an $(110)[\bar{1}10]$ orientation, and the dislocation emission thus corresponds to the one seen in Figure 11(b). Both during crack growth and dislocation emission a twin region is growing from the crack tip in a direction normal to the original crack-plane, and it keeps growing as loading increases and more dislocations are emitted in the opposite direction. In Figure 13(a) we present the change in crack shape together with the stress – strain

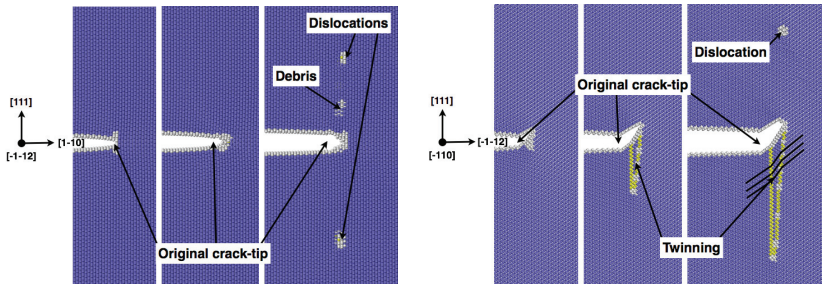

(a) A (111)[$\bar{1}\bar{1}2$] cut. (b) A (111)[$\bar{1}10$] cut.

Figure 14. Cuts through the penny-shaped crack simulated on the (111)-plane. Atoms colored due to CNA, where blue is bcc, green is fcc, yellow is bcc twin and white is unknown structure. (Color online.)

curve for this simulation, and it shows how the stress flattens out as dislocations are emitted from the crack.

4. Discussion

After presenting the results for all the through-thickness and embedded penny-shaped crack simulations in the previous section, we now compare the two crack geometries and discuss the mechanisms observed.

4.1. Comparison of penny-shaped and through-thickness cracks on a {100} *crack-plane*

Looking at Figures 3 and 8 we observe many of the same type of events in the two types of simulations. In the (010)[101] system we get formation of fcc followed by twinning in both cases, and in the (010)[001] system we only get some fcc formation. One difference is that in the (010)[101] case, we get twinning symmetrically around the crack tip in the penny-shaped simulation, while for the through-thickness crack fcc and twinning only appear on one side. Also, for the the (010)[001] system we get broader fcc regions with a through-thickness crack than a penny-shaped; yet the directions are the same.

The occurrence of twinning in the (010)[101] crack orientation is seen before [8, 9, 11], and it is a mechanism tightly linked to cleavage at low temperatures. The twinning regions do, however, quickly stretch far away from the crack-tip, making it hard to simulate large enough systems to avoid boundary influence.

What do we learn when going from semi-3D to full 3D in this case? First of all, we can see how the crack grows in specific directions in order to change into an almost quadratic shape. This results in a situation where most of the crack front has a $\{010\}\langle 001\rangle$ orientation with fcc formation at $\pm 45°$. These fcc regions grow out towards the edges of the square, and when they meet in the corners they form twinning bands. The twinning relaxes the corners, making the crack almost octagonal at this point, and the twinning regions in the $\{010\}\langle 101\rangle$ orientations become broader and stretches further out.

4.2. Comparison of penny-shaped and through-thickness cracks on a {110} *crack-plane*

From comparing only Figures 4 and 11 we see many similarities in how the crack-tip behaves in through-thickness and penny-shaped crack simulations. The (110)[001] orientations result in crack extension and formation of fcc, while the (110)[$\bar{1}$10] orientations show crack-tip blunting by emission of dislocations in {112}⟨111⟩ slip systems. This is in agreement to previous studies of the same orientations [10, 11].

What we cannot see in the through-thickness geometry, however, is how our dislocations form loops in three dimensions and leave debris and twinning bands behind. This is clearly seen in the penny-shaped crack geometry, where we also observe how the crack changes shape due to bond-breaking, mainly in the [$\bar{1}$10] and [1$\bar{1}$0] directions. With a full 3D simulation we can observe the screw and mixed dislocations that make up the sides of the edge dislocation loops, and how they turn into mechanical twins as the dislocation moves further away from the crack.

4.3. Comparison of penny-shaped and through-thickness cracks on a {111} *crack-plane*

In Figures 5 and 14 we find many similarities, and the mechanisms are in general the same in the two types of crack simulation. The (111)-plane has higher surface energy than both the (100)- and (110)-planes [5], and thus we did not expect any crack growth in the simulations where this was the initial crack plane. This was confirmed in both through-thickness and penny-shaped crack simulations, where we saw either pure edge dislocation emission or a combination of crack growth away from the original plane with twinning and dislocations.

Dislocations in a {110}⟨111⟩ slip system with a (111)[$\bar{1}\bar{1}$2] crack and a {112}⟨111⟩ twin combined with crack growth on an {110} plane with a (111)[$\bar{1}$10] crack has previously been observed by Gordon et al. [10] using several different EAM potentials. It is, however, interesting to see the same mechanisms occur even when we have a penny-shaped crack.

A thorough study of the penny-shaped crack during loading shows how the crack changes from circular to hexagonal, which creates straight crack fronts with ⟨112⟩ and ⟨110⟩ directions. This enables the dislocations and mechanical twins seen later in the simulation.

4.4. Comparison of K_I and E values

An overview of events and stress-intensity values K_I for through-thickness and penny-shaped cracks is given in Tables 2 and 3. The events are happening at larger strains and stresses with the penny-shaped cracks, but since the difference between the expressions (1) and (2) for K_I values are a factor $2/\pi \approx 0.6$, the stress-intensities for the two crack geometries end up being very similar. Comparing K_I values for the same events in the same crack orientations for different geometries reveal that they are within 10% from each other.

Also, E-moduli for the different loading directions have been estimated from all simulations, and they are presented in Table 4 together with values calculated from the interatomic potential. The Young's moduli from simulations have been estimated from the initial, linear part of the stress – strain curves up to a strain of 1.0% by fitting data to a linear function, while the literature values have been calculated from the

Table 4. *E*-moduli (in GPa) estimated from the various crack simulations performed in this study, and calculated from the elastic stiffness values C_{11}, C_{12} and C_{44} given in [10].

Type	Crack orientation/plane (plane)[front direction]	*E*-modulus (GPa)
Through-thickness	(0 1 0)[1 0 1]	132
	(0 1 0)[0 0 1]	131
	(1 1 0)[0 0 1]	202
	(1 1 0)[$\bar{1}$ 1 0]	204
	(1 1 1)[$\bar{1}$ $\bar{1}$ 2]	251
	(1 1 1)[$\bar{1}$ 1 0]	252
Penny-shaped	(1 0 0)	136
	(1 1 0)	214
	(1 1 1)	266
Literature[10]	(1 0 0)	135
	(1 1 0)	224
	(1 1 1)	286

elastic stiffness values C_{11}, C_{12} and C_{44} given in [10] for the "Mendelev II extended" potential [26]. Comparing results from through-thickness and penny-shaped crack simulations show almost no difference in *E*-value for the two geometries, and also the difference between the simulations and potential data is small (well within 10% for all values). Thus, crack geometry does not seem to affect the Young's moduli - what matters is the direction in which we measure the elastic response.

4.5. Change in crack shape and competition between mechanisms

Perhaps the most striking feature when studying penny-shaped cracks is to observe how the crack changes shape. As shown in the Results section and discussed above, we get very limited bond-breaking along the crack-tip of the initially circular crack. This rather small change in crack shape has the effect of enabling fcc formation, dislocation emission and mechanical twins along a large part of the crack front, thus suppressing unstable crack growth by bond-breaking.

When comparing specific directions in the penny-shaped cracks with the though-thickness cracks, we see that *locally* the same mechanisms take place at approximately the same stress-intensity values. But *globally*, the penny-shaped cracks ends up being more ductile – dislocation emission and mechanical twins ends up "winning" over bond-breaking when looking at the crack as a whole. It is interesting to see how nature organizes itself so that the crack ends up growing as little as possible, favoring blunting of the crack-tips.

4.6. Remarks

In these simulations a strain rate of $5{\cdot}10^8$ s^{-1} is used, which might favor transformation bcc $\rightarrow$ fcc and the creation of twinning regions. This is however, one of the limitations of molecular dynamics – there is only a short time window available to study in order for the simulations to be done within reasonable computational time. Slightly slower strain rates could be investigated by spending more time, but they would still be very far from regular experiments, which are usually performed at the order of 10^{-3} s^{-1}.

Another aspect is the potential used in the simulations. As noted in the Methods section the Mendelev potential produce results in good agreement with DFT calculations, and should be an ideal choice for simulations like these. There exists even more accurate potentials for iron, like *bond-order potentials* (BOP) [35, 36] that take into account directional bonding and magnetic properties, or one could do direct DFT calculations on a geometry. However, these approaches require a lot more computational resources and thus limit the system size. In order to investigate geometries of the size we have in this paper, the less computation-demanding EAM potential was therefore used, allowing us to study fracture mechanisms on a larger scale. In the future, faster computers, more efficient code and further development of multiscale methods could allow us to run large-scale simulations even with BOP or DFT calculations.

The simulations in this paper are performed at a temperature of 1 K. In future simulations increased temperatures and the brittle-to-ductile (BDT) transition will be interesting to investigate, to see how the penny-shaped crack changes behavior as temperature increases.

Finally, since the simulations in this study is of finite size with periodic boundary conditions, mechanisms that reach the boundaries will re-enter the simulation cell from the opposite side. This is something that cannot be avoided, but in almost all cases the most interesting simulation events take place well before any interaction with the boundaries is taking place.

5. Conclusion

Molecular dynamics simulations of through-thickness and penny-shaped cracks have been performed. The crack planes (100), (110) and (111) have been chosen and loaded in Mode I using an EAM potential. By simulating three-dimensional, penny-shaped cracks, we can observe crack-tip effects and competition between crack mechanisms that are not directly shown through the simulation of semi-3D, through-thickness cracks. More specifically, we find that the crack changes shape by bond-breaking in order to make slip systems for dislocation emission more easily accessible. This makes the penny-shaped cracks as a whole dominated by dislocation emission and mechanical twins, suppressing further unstable crack growth.

Acknowledgments

We acknowledge the support from NTNU, the Research Council of Norway (Arctic Materials project supported through the Petromaks program, Contract No.187389/S30) and the industry consortium behind the Arctic Materials project. The support from NOTUR (Norwegian High Performance Computing) with the generous computation quota is highly acknowledged.

References

[1] R. W. K. Honeycombe, The plastic deformation of metals, Edward Arnold (Publishers) Ltd., 1968.

[2] N. P. Allen, B. E. Hopkins, J. E. McLennan, The tensile properties of single crystals of high-purity iron at temperatures from 100 to -253 degrees C, Proceedings of the Royal Society of London. Series A, Mathematical and Physical Sciences 234 (1197) (1956) 221–246.

[3] W. Biggs, P. Pratt, The deformation and fracture of alpha-iron at low temperatures, Acta Metallurgica 6 (11) (1958) 694 – 703.
[4] J. Nohava, P. Haušild, M. Karlík, P. Bompard, Electron backscattering diffraction analysis of secondary cleavage cracks in a reactor pressure vessel steel, Materials Characterization 49 (3) (2002) 211 – 217.
[5] P. Błoński, A. Kiejna, Structural, electronic, and magnetic properties of bcc iron surfaces, Surface Science 601 (1) (2007) 123–133.
[6] V. Shastry, D. Farkas, Molecular statics simulation of fracture in α-iron, Modelling and Simulation in Materials Science and Engineering 4 (1996) 473–492.
[7] P. Hora, V. Pelikán, A. Machová, A. Spielmannová, J. Prahl, M. Landa, O. Červená, Crack induced slip processes in 3D, Engineering Fracture Mechanics 75 (2008) 3612–3623.
[8] A. Machová, G. E. Beltz, Ductile-brittle behavior of (0 0 1)[1 1 0] nano-cracks in bcc iron, Materials Science and Engineering A 387-389 (2004) 414–418, 13th International Conference on the Strength of Materials.
[9] Y.-F. Guo, C.-Y. Wang, Y.-S. Wang, The effect of stacking faults or twin formation on crack propagation in bcc iron, Philosophical Magazine Letters 84 (2004) 763–770.
[10] P. A. Gordon, T. Neeraj, M. J. Luton, D. Farkas, Crack-tip deformation mechanisms in α-Fe and binary Fe alloys: an atomistic study on single crystals, Metallurgical and Materials Transactions A 38A (2007) 2191–2202.
[11] I. R. Vatne, E. Østby, C. Thaulow, D. Farkas, Quasicontinuum simulation of crack propagation in bcc-Fe, Materials Science and Engineering: A 528 (15) (2011) 5122 – 5134.
[12] A. Latapie, D. Farkas, Molecular dynamics simulations of stress-induced phase transformations and grain nucleation at crack tips in Fe, Modelling and Simulation in Materials Science and Engineering 11 (5) (2003) 745.
[13] K. S. Cheung, S. Yip, A molecular-dynamics simulation of crack-tip extension: the brittle-to-ductile transition, Modelling and Simulation in Materials Science and Engineering 2 (1994) 865–892.
[14] Y.-F. Guo, C.-Y. Wang, D.-L. Zhao, Atomistic simulation of crack cleavage and blunting in bcc-Fe, Materials Science and Engineering A 349 (2003) 29–35.
[15] J. Belak, On the nucleation and growth of voids at high strain-rates, Journal of Computer-Aided Materials Design 5 (1998) 193–206.
[16] E. M. Bringa, S. Traiviratana, M. A. Meyers, Void initiation in fcc metals: Effect of loading orientation and nanocrystalline effects, Acta Materialia 58 (13) (2010) 4458 – 4477.
[17] L. P. Dávila, P. Erhart, E. M. Bringa, M. A. Meyers, V. A. Lubarda, M. S. Schneider, R. Becker, M. Kumar, Atomistic modeling of shock-induced void collapse in copper, Applied Physics Letters 86 (2005) 161902.
[18] S. Traiviratana, E. M. Bringa, D. J. Benson, M. A. Meyers, Void growth in metals: Atomistic calculations, Acta Materialia 56 (15) (2008) 3874–3886.
[19] R. Rudd, E. Seppälä, L. Dupuy, J. Belak, Void coalescence processes quantified through atomistic and multiscale simulation, Journal of Computer-Aided Materials Design 14 (2007) 425–434.
[20] M. Q. Chandler, M. Horstemeyer, M. Baskes, P. Gullett, G. Wagner, B. Jelinek, Hydrogen effects on nanovoid nucleation in face-centered cubic single-crystals, Acta Materialia 56 (1) (2008) 95 – 104.
[21] J. Marian, J. Knap, G. Campbell, A quasicontinuum study of nanovoid collapse under uniaxial loading in Ta, Acta Materialia 56 (10) (2008) 2389 – 2399.
[22] Y. Tang, E. M. Bringa, B. A. Remington, M. A. Meyers, Growth and collapse of nanovoids in tantalum monocrystals, Acta Materialia 59 (4) (2011) 1354 – 1372.
[23] R. E. Rudd, Void growth in BCC metals simulated with molecular dynamics using the Finnis-Sinclair potential, arXiv.org (2009) 0906.0619v1.
[24] S. J. Plimpton, Fast parallel algorithms for short-range molecular dynamics, Journal of Computational Physics 117 (1995) 1–19. `http://lammps.sandia.gov/`
[25] M. Ruda, D. Farkas, G. Garcia, Atomistic simulations in the Fe-C system, Computational Materials Science 45 (2) (2009) 550–560.
[26] G. J. Ackland, M. I. Mendelev, D. J. Srolovitz, S. Han, A. V. Barashev, Development of an interatomic potential for phosphorus impurities in α-iron, Journal of Physics: Condensed Matter 16 (2004) S2629–S2642.
[27] M. I. Mendelev, S. Han, D. J. Srolovitz, G. J. Ackland, D. Y. Sun, M. Asta, Development of new interatomic potentials appropriate for crystalline and liquid iron, Philosophical Magazine 83 (35) (2003) 3977–3994.
[28] S. L. Frederiksen, K. W. Jacobsen, Density functional theory studies of screw dislocation core structures in bcc metals, Philosophical Magazine 83 (3) (2003) 365–375.

[29] C. Domain, G. Monnet, Simulation of screw dislocation motion in iron by molecular dynamics simulations, Physical Review Letters 95 (21) (2005) 215506.
[30] A. Stukowski, Visualization and analysis of atomistic simulation data with OVITO – the open visualization tool, Modelling and Simulation in Materials Science and Engineering 18 (1) (2010) 015012.
[31] J. D. Honeycutt, H. C. Andersen, Molecular dynamics study of melting and freezing of small Lennard-Jones clusters, The Journal of Physical Chemistry 91 (19) (1987) 4950–4963.
[32] H. Tsuzuki, P. S. Branicio, J. P. Rino, Structural characterization of deformed crystals by analysis of common atomic neighborhood, Computer Physics Communications 177 (6) (2007) 518 – 523.
[33] T. L. Anderson, Fracture mechanics: fundamentals and applications, 3rd edition, CRC Press, New York, USA, 2005.
[34] D. Hull, D. Bacon, Introduction to dislocations, 4th Edition, Butterworth-Heinemann, 2001.
[35] M. Müller, P. Erhart, K. Albe, Analytic bond-order potential for bcc and fcc iron - comparison with established embedded-atom method potentials, Journal of Physics: Condensed Matter 19 (2007) 326220.
[36] M. Mrovec, D. Nguyen-Manh, C. Elsässer, P. Gumbsch, Magnetic bond-order potential for iron, Physical Review Letters 106 (2011) 246402.

Modeling of size and strain rate effects in compression tests of iron nanopillars

Submitted to Computational Materials Science

Paper III

Modeling of size and strain rate effects in compression tests of iron nanopillars

C. H. Ersland[a,*], C. Thaulow[a]

[a]*Department of Engineering Design and Materials, Norwegian University of Science and Technology, NO-7491 Trondheim, Norway*

Abstract

The size and strain rate effect on the deformation behavior of defect-free bcc-Fe nanopillars is investigated through molecular dynamics simulations. Three crystallographic orientations, four pillar sizes and two strain rates have been simulated in displacement-controlled compression. It is found that deformation mechanisms and stress – strain behavior is highly dependent on the crystallographic orientation in the single crystal. For (100) and (110) pillar orientations there is a clear size-strengthening effect found to be caused by a lack of space to emit dislocations inside the pillars, while for a (111) orientation the effect is less profound. Lower strain rates are found to result in lower stresses and strains before deformation begins.

Keywords: deformation, molecular dynamics, iron, size effect, nanostructure

1. Introduction

In the last decades micropillar compression testing has been developed and used to investigate a variety of materials at the micron and sub-micron scale. Using focused ion beam (FIB) milling [1–4], nanoimprinting [3], chemical etching [5] or other techniques [6], material can be removed from a sample surface to produce small pillars. The pillars are subsequently tested in a nanoindenter by using a hard flat tip to compress the pillars. They may be located with high precision at a point of interest in a complicated microstructure, which for metals includes single grains, grain boundaries, multigrain and multiphase structures.

A well-known expression within this type of research is "smaller is stronger", which points at the strengthening in materials with increasingly small dimensions, where the yield stress σ_y is said to be following a trend $\sigma_y \propto D^{-\alpha}$, where D is the pillar diameter. Numerous experimental studies have confirmed this size-strengthening effect, both for fcc [7–11] and bcc [1, 4, 12–14] materials, with bcc generally showing the smallest values of α. Bei et al. [5], on the other hand, did not observe any size effect when performing indents on micron-sized Mo pillars.

One of the most recent studies on bcc [15] investigated sample-size strengthening in Mo pillars with diameters as low as 75 nm. Surprisingly, two different size regimes were found, with α becoming approximately three times larger for $D < 200$ nm, resulting in the same size-strengthening as for fcc at these small diameters.

The strain-rate used during nanopillar compression is also known to influence the measured material strength. Experimentally, this was investigated by e.g. Jennings et al. in Cu pillars [16], and it was found that in their strain rate range ($10^{-3} - 10^{-1}$ s^{-1}), faster loading gave higher strength. Zhu et al. [17] found through MD simulations and analytic derivations a strain rate and temperature dependence of the dislocation nucleation stress in a copper nanowire. The strain rate affected the stress more at elevated temperatures, but was still noticeable at low temperatures.

Numerous molecular dynamics (MD) and dislocation dynamics (DD) simulations of nanopillar and nanowire compression have been performed the past few years [17–27], studying the effects mentioned above, but have also given a lot of attention to how dislocations behave in very small structures.

In fcc the effect of *dislocation starvation* [8, 28] is proposed to be the mechanism mainly responsible for increased strength at the nanoscale, since existing and nucleated dislocations are quickly escaping to the material surface, without multiplying. Bcc materials, however, shows instead that *dislocation multiplication* is taking place, resulting in only a modest strengthening effect. Weinberger and Cai [29] studied multiplication of a mixed $(01\bar{1})[111]$ dislocation in a compressed nanopillar along a $\langle 100 \rangle$ direction. This dislocation quickly changed into a pure screw dislocation, followed by formation of a cusp that turned into a dislocation loop, moving on both {110} and {112} planes. This mechanism showed that bcc micropillars are unlikely to become "dislocation-starved", and would allow further plastic deformation.

In this paper we are investigating nanopillar compression of body-centered cubic (bcc) iron, and for this type of structure we have some important possible deformation mechanisms. Slip in bcc normally occurs in $\langle 111 \rangle$ directions, which are the closest packed. The most common slip planes are {110}, {112} and {123} [30]. Twinning can

*Corresponding author
Email address: christer.h.ersland@ntnu.no (C. H. Ersland)

also occur, and this usually happens on the {112} planes in ⟨111⟩ directions. There is an increased tendency for twinning to occur with increasing deformation rate and decreasing temperature. The above slip systems are also found experimentally to be the most active in pure iron and low-alloy steels [31, 32].

Lowry et al. [33] were able to experimentally approach the theoretical material strength for molybdenum by annealing nanopillars so they became dislocation-free. In our MD simulations the pillars are made of perfect, dislocation-free material, so we would expect high material strength.

The aim of this paper is to understand the size effect and deformation mechanisms in iron nanopillars at low temperatures. Effects concerning crystallographic lattice orientation and strain rate sensitivity are also investigated. The Results section shows qualitatively how the pillars deform due to compression and their stress – strain behavior, while in Discussion we investigate how the above mentioned parameters affect material strength and behavior.

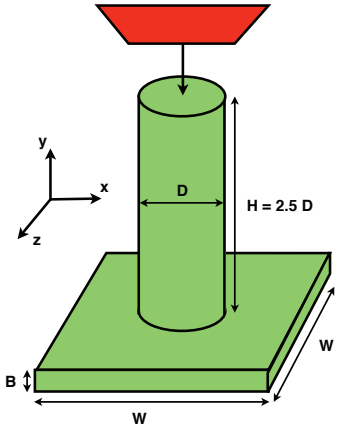

Figure 1: Schematic overview of the system we are simulating, with pillar diameter D and height L, as well as coordinate system and bulk/surface thickness B indicated.

2. Methods

Molecular dynamics (MD) simulations have been performed using the software LAMMPS [34] run on a supercomputer. Our simulated system is shown schematically in Figure 1, where the most important system lengths are marked. Cylindrical pillars with a diameter D and a pillar height $L = 2.5D$ are used in all simulations. The pillars are standing on a quadratic base large enough for the pillars not to interfere with the system boundaries, and with a thickness of about $B = 25$ Å for all simulations. The two bottom atom layers of the base are kept fixed during indentation, resembling a rigid bulk material below. Periodic conditions are used in-plane (in x- and z-directions), thus in each case we effectively simulate an array of free-standing nanopillars. Interatomic forces were calculated using an iron EAM potential by Mendelev et al. [35] – the so-called "Mendelev II" potential. This potential is one of the few known to correctly predict the sixfold symmetry of screw dislocation cores, as calculated by DFT calculations [36, 37], so we choose this since screw dislocations are expected to be important in the plastic deformation of the nanopillars. The bcc lattice was initially created with a lattice parameter of $a_0 = 2.85532$ Å, and the system was then relaxed at a temperature of 5 K and zero pressure in the periodic directions using an NPT scheme. The flat punch indenter tip was simulated as a flat, hard plane parallel to the pillar top, compressing the pillar with a constant velocity. This velocity is calculated for each simulation using the pillar height, in order to use the same *strain rate* across the different pillar sizes. Two strain rates $\dot{\varepsilon} = 5 \cdot 10^7$ s^{-1} and $5 \cdot 10^8$ s^{-1} are used for all pillar orientations and sizes, and will sometimes be referred to as the "slow" and "fast" loading in the text. A timestep of 1.5 fs is used throughout the simulations.

Four diameters have been simulated: $D = 50$, 100, 200 and 400 Å. For each pillar size, three crystallographic orientations were investigated. The orientations correspond to the indentation plane punching parallel to the (100), (110) and (111) planes of the bcc lattice. The number of atoms in a single simulation varies from around 30,000 up to about 12 millions, depending on pillar diameter and orientation.

In order to further test the strain rate sensitivity, we selected the pillar of diameter 100 Å with (110) orientation to be tested at two additional strain rates, namely $\dot{\varepsilon} = 5 \cdot 10^6$ s^{-1} and $5 \cdot 10^9$ s^{-1}.

3. Results

In the following sections, the results of the simulations are shown, divided with respect to the crystallographic orientations that have been tested. All simulation figures are made using the software OVITO [38]. Some figures have coloring due to the von Mises stress per atom, with blue and red as low and high stresses, respectively. In some of these figures, all the atoms in the simulation are included, while in others only atoms with high potential energy are shown, in order to highlight dislocation movement. In certain figures, common neighbor analysis (CNA) [39, 40] is used, and atoms are colored such that white is "unknown" lattice structure, while red/pink is bcc twin or screw dislocation atoms. These figures show only non-bcc atoms, and the surface atoms are removed in order to see the dislocations inside. In analyzing the dislocations and determining Burgers vectors, the Dislocation Extraction Algorithm (DXA) [41] has been used.

There are distinct differences in how pillars with different orientations deform. A representative overview of

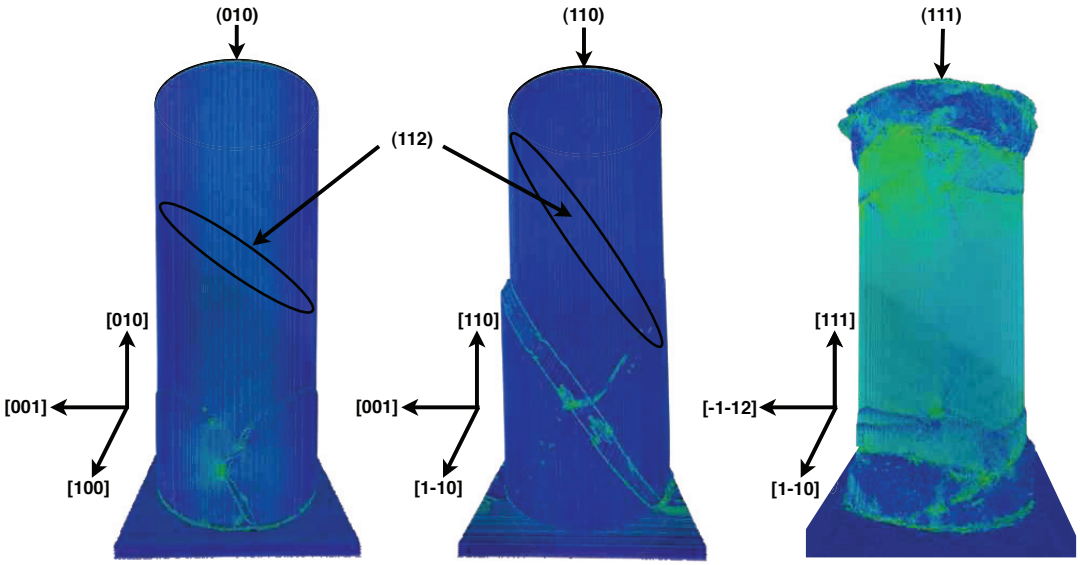

Figure 2: Overview of the three pillar orientations simulated with $D = 400$ Å, after a fair amount of deformation has occurred. To the left is the (010) orientation, where dislocation loops emit in four $\{112\}\langle 111\rangle$ slip systems at the base of the pillar. A (112) plane is indicated on the figure for comparison. In the middle is the (110) orientation, where dislocation loops follow two crossing $\{112\}\langle 111\rangle$ slip systems starting from the base of the pillar. Also here a (112) plane is indicated in the pillar. To the right is the (111) orientation, showing deformation at both top and bottom of the pillar. (Color online.)

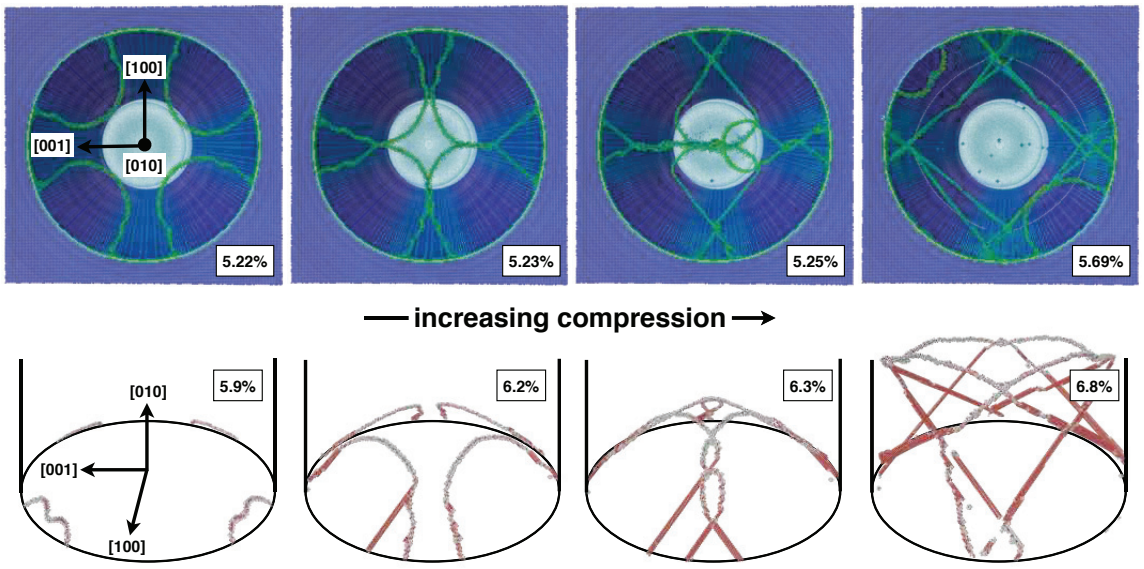

Figure 3: Dislocation details from the largest ($D = 400$ Å) pillar indented on the (010) plane, shown at different compression levels. The top row shows results for a strain rate $\dot{\varepsilon} = 5 \cdot 10^7$ s^{-1}, and we view the pillar from below, looking up at the dislocation loops. Only atoms with high potential energy are shown, in order to see the dislocations, and the atoms are colored according to their von Mises stress. The bottom row shows results for a strain rate $\dot{\varepsilon} = 5 \cdot 10^8$ s^{-1}, and we view the pillar from the side, showing only non-bcc atoms inside the pillar (surface atoms removed). Here, atoms are colored according to CNA. (Color online.)

how the pillars look after some deformation has occurred, is given in Figure 2. In the following section we present the general deformation mechanisms for the three orientations studied; specific differences between pillar sizes and strain rates will be presented in the Discussion section.

3.1. Mechanisms – compression on a {010} plane

The {010} crystallographic orientation shows stable compression of the pillar until a point where suddenly dislocation loops appear at the bottom of the pillar, consisting of edge dislocation fronts and screw/mixed dislocation sides (see Figure 3). They nucleate from one or more out of four symmetric points at the pillar surface, in the ⟨101⟩ directions where the pillar is attached to the base, and have a $1/2\langle 111\rangle$ Burgers vector. The loops move upwards and across the pillar in ⟨111⟩ directions on {112} planes, at angles of 35.3° with respect to the base, and they cross paths approximately in the middle of the pillar.

After the edge dislocation fronts have passed each other, they continue moving through the pillar and finally reach the surface on the other side, resulting in the pillar becoming wider at the bottom. The screw dislocation "arms" of the loops, however, get locked into each other after the collision, and they stay inside the pillar as loading continues. At a later stage, more loops are emitted in the same slip systems, and the pillar keeps getting wider at the bottom.

3.2. Mechanisms – compression on a {110} plane

For the pillars compressed on a {110} plane, the first deformation event is one or two dislocation loops with $1/2\langle 111\rangle$ Burgers vectors emitted from two symmetrically placed sites at the base of the pillar. These points are in the ⟨001⟩ directions on the pillar surface, and after being emitted, the dislocations move in $\{112\}\langle 111\rangle$ slip systems upwards and towards the middle of the pillar, at angles 54.7° with respect to the base. The dislocation movement is shown in Figure 4, where in the first figure on each row we observe the first signs of the dislocation loops. They move towards the center and also up inside the pillar, cross each other and finally reaches the surface of the pillar further up.

As the loops reach the free surface on the far side of the pillar, a twinning region is spreading backwards along the dislocation path, making two crossing {112} twin planes. In many cases, only one of these "survives" as the pillar is further compressed, and we observe that the twinned region keeps on expanding (two twin planes moving further away from each other). Yet in other cases, the two twin regions stay there locked into each other, as the loading continues. No deformation happens in the $[1\bar{1}0]$ and $[\bar{1}10]$ directions as the pillar is compressed; only the [001] and $[00\bar{1}]$ directions slide out along the twin planes.

For the largest pillars, in addition to the regular dislocation loop motion and twin planes, we observe *dislocation multiplication* as loading continues. This occurs from sites along the screw and mixed dislocations following on the sides of the edge dislocation fronts that cut through the pillar, and is often associated with vacancies and debris where the multiplication starts to happen. The "arms" of a dislocation multiplication follow $\{112\}\langle 111\rangle$ slip systems, but on two parallel {112} planes slightly separated. In Figure 4, dislocation multiplication loops are clearly seen in the two last frames of the top row.

3.3. Mechanisms – compression on a {111} plane

The last orientation tested has compression on a {111} plane. For small pillars with high deformation rate, the deformation of the pillar happens almost exclusively at the *top* of the pillar, where material "peels away" as the indenter moves down. In larger pillars with smaller $\dot{\varepsilon}$, this deformation is accompanied by dislocation emission from up to three symmetrically placed sites in ⟨112⟩ directions on the surface at the bottom of the pillar, but the top keeps on deforming as the pillar is compressed. The dislocation activity in the bottom of the pillar is shown in Figure 5. The largest and most slowly loaded pillars show no or almost no deformation at the top of the pillar, while there is extensive dislocation emission at the bottom of the pillar

As shown in Figure 5, the loops at the bottom of the pillar move through the pillar, and often collide along the way. The loops have $1/2\langle 111\rangle$ Burgers vectors, and they move up and across the pillar at angles approximately 20° with respect to the base. As seen in the last two frames on each row in the figure, the dislocations occasionally leave behind trails of straight screw dislocations from discrete sites on the edge dislocation front. These are shown as straight red lines in the bottom frames of Figure 5, and we observe that many of them stay in the material as straining continues.

The largest pillars with (111) orientation also give rise to many dislocation multiplications, in the same way as described for the (110) pillar. This can be clearly seen in the last frame on the top row in Figure 5.

3.4. Stress – strain relations

Stress – strain plots for the simulations with a strain rate of $5 \cdot 10^7$ s^{-1} are given in Figures 6, 7 and 8, where the stress experienced by the indenter is plotted against the strain it imposes on the system. The stress is found by dividing the indenter force by the area the indenter is pushing on (a circle on the top of the pillar), thus normalizing the plots with respect to pillar size. The strain is calculated by the expression $\varepsilon = (H - H_0)/H_0$, where H is the current system height and H_0 is the system height at the beginning of the loading.

A fitting to a linear function $f(x) = ax + b$ has been performed on the initial part of the stress – strain curves, in the range $1-5\%$, where they are most linear. The fitted values of a are estimates of the Young's moduli E_{ijk} for the different planes $\{ijk\}$ that have been tested. An overview of the resulting E-values is given in Table 1.

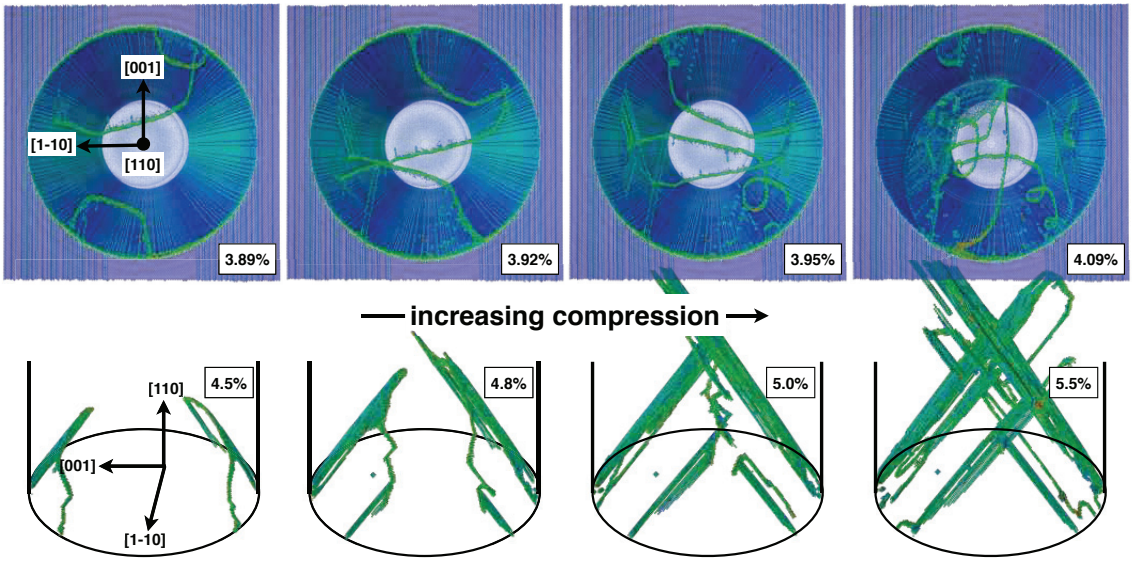

Figure 4: Dislocation details from the largest ($D = 400$ Å) pillar indented on the (110) plane, shown at different compression levels. The top row shows results for a strain rate $\dot{\varepsilon} = 5 \cdot 10^7$ s^{-1}, and we view the pillar from below, looking up at the dislocation loops. Only atoms with high potential energy are shown, in order to see the dislocations. The bottom row shows results for a strain rate $\dot{\varepsilon} = 5 \cdot 10^8$ s^{-1}, and we view the pillar from the side, showing only non-bcc atoms inside the pillar (surface atoms removed). The atoms in both rows are colored according to their von Mises stress (Color online.)

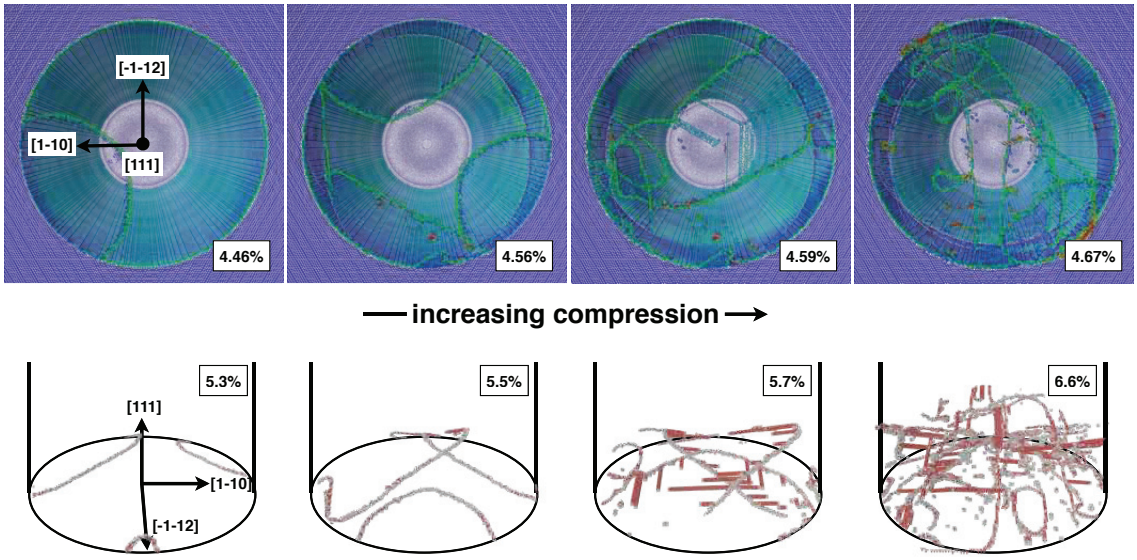

Figure 5: Dislocation details from the largest ($D = 400$ Å) pillar indented on the (111) plane, shown at different compression levels. The top row shows results for a strain rate $\dot{\varepsilon} = 5 \cdot 10^7$ s^{-1}, and we view the pillar from below, looking up at the dislocation loops. Only atoms with high potential energy are shown, in order to see the dislocations, and the atoms are colored according to their von Mises stress. The bottom row shows results for a strain rate $\dot{\varepsilon} = 5 \cdot 10^8$ s^{-1}, and we view the pillar from the side, showing only non-bcc atoms inside the pillar (surface atoms removed). Here, atoms are colored according to CNA. (Color online.)

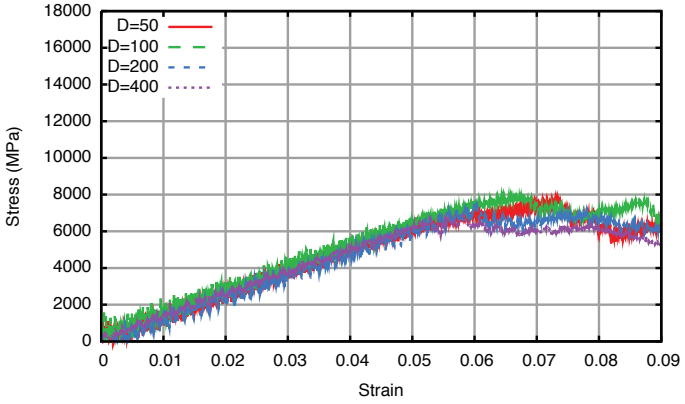

Figure 6: Stress – strain curves for the simulations of pillar indentation on the (100) plane, at a strain rate of $5 \cdot 10^7$ s^{-1}.

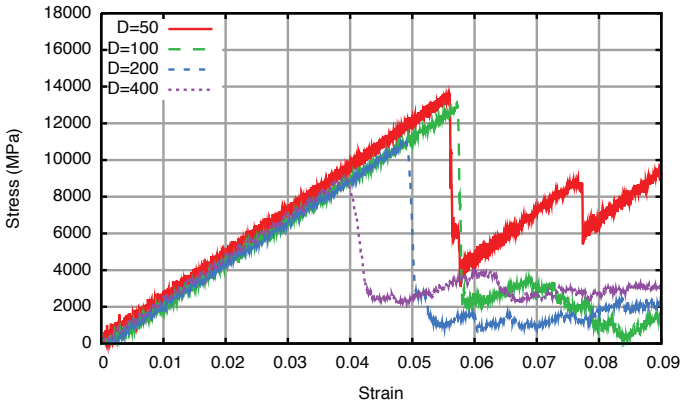

Figure 7: Stress – strain curves for the simulations of pillar indentation on the (110) plane, at a strain rate of $5 \cdot 10^7$ s^{-1}.

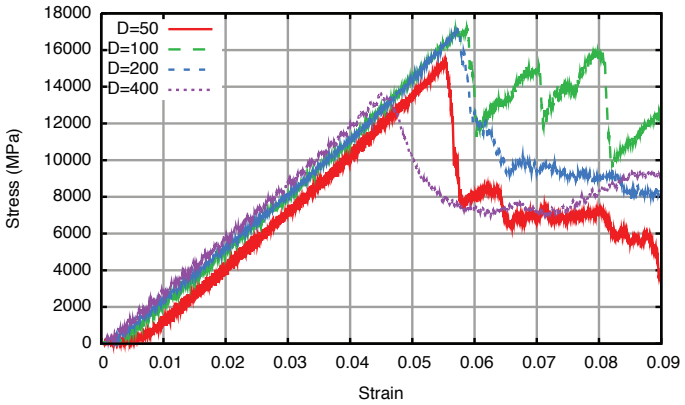

Figure 8: Stress – strain curves for the simulations of pillar indentation on the (111) plane, at a strain rate of $5 \cdot 10^7$ s^{-1}.

4. Discussion

4.1. Size and strain rate effect on Young's moduli

From the estimated E-moduli in Table 1 we see that the three pillar orientations give highly different elastic response, as expected due to the anisotropic nature of iron. For a given orientation, E-values for different sizes and strain rates differ in general very little, the maximal difference being 9%. The last columns of Table 1 show calculated E-values from the interatomic potential data given in [35] and experimental data [42], and we notice that our results do not differ significantly from these values, even though they are derived from elastic constants in a bulk material sample. This clearly shows that E is a true material constant.

In polycrystals all possible orientations will be present, contributing to the elastic response. As a crude estimate, we calculate the mean value of all E-values from our simulations, and find $E \approx 221$ GPa. This is close to the reference value of 211 GPa for bulk iron, and shows that our simulated iron samples also correspond nicely to a real material.

4.2. Effect of pillar size on stress

The main deformation mechanisms of pillars as a function of size are not significantly different when considering the three orientations separately. But, what *do* differ is the maximum stresses and strains the pillars can withstand, and the points at which the first deformation events starts to happen. In Figure 10 the stress at the first deformation event is plotted against the pillar diameter on a log – log scale, and we observe a strong orientation dependence. We define the first deformation event as the first dislocation loop emission or the first visible squeezing on the top (for the (111) pillars), whichever comes first. This is found by visual inspection of the simulation data, where there is a strain difference of 0.015% between each data point (0.15% for the faster strain rate).

As seen in Figure 10, clear size strengthening trends in the deformation stress can be found for orientations (100) and (110). Fitting of the data to $\sigma_{\text{deform}} = \beta D^{-\alpha}$ has been performed, and the resulting curves are plotted together with the data points as straight lines. For the slowest and fastest strain rates on a (100) pillar, we get $\alpha = 0.1$ and 0.3, respectively, and for the (110) pillar the corresponding values are $\alpha = 0.2$ and 0.3. Most of these values are within the same range as the experimentally determined α-values between $0.22 - 0.48$ [1, 12, 13] The (111) pillar displays no clear size-strengthening: For the slowly loaded pillars the deformation stress is lower both for the smallest and the largest diameter, while the fast loaded pillar show very little sensitivity to pillar size.

4.3. Deformation mechanisms

As shown in Figures 2 - 5 and through the stress – strain curves (Figures 6 - 8) we obtain very different deformation behavior for the three orientations tested. This is, to a large extent, caused by the number of available slip systems. In the (100) pillar four symmetrical $\{112\}\langle 111\rangle$ slips systems are available, with a Schmid factor of 0.47. The easily available slip possibilities are manifested through a low deformation and maximum stress (see Figure 6).

For pillars loaded on (110) planes, the two symmetrical $\{112\}\langle 111\rangle$ slip systems also has the highest Schmid factor with a value of 0.47, hence it is reasonable that these are the ones activated. The (110) pillars all have edge dislocation loops with screw and mixed dislocations on the sides. As the loops collide with each other and the opposite pillar surface, the screw dislocations produce debris, twinning regions and twin planes. Upon further loading these planes move further apart, making a wider twinned region. This is the same behavior studied by Marian et al. [43] and previously theoretically predicted in [44, 45]. The very sudden appearance of a weak twinned region along which the pillar can deform, results in a rapid drop in stress to low values (see Figure 7).

For the pillars loaded in the (111) plane, the $\{112\}\langle 111\rangle$ and $\{123\}\langle 111\rangle$ slip systems have the highest Schmid factors, so these should theoretically be the ones activated. These have, however, Schmid factors close to 0.3 – lower than for the other orientations. This is reflected in the stress levels (see Figure 8), which are the highest of the three orientations tested.

Common for all simulated pillars is that the dislocations responsible for the deformation start at the surface of the pillar, in most cases at the base of the pillar, where there is a stress concentration due the sharp boundary between the pillar and the surface it stands on. This stress concentration is an important effect to consider, since this is where we find the dislocations nucleating, but it is in many previous simulations [19–27] not included. Most of these simulations are only cylinders, in many cases periodic along the cylinder axis, thus effectively turning the simulations into nano*wire* compression simulations, not nano*pillar* simulations, and the "pillars" are also in most cases not allowed to bend/move freely in the x- and z-directions, as done here. Even though experimental pillars will not have as sharp a transition between the pillar and the base material as in our simulations, there will always be kinks on the pillar surface at the atomistic levels, which can act as dislocation nucleation points. We thus believe that this effect is important to include in simulations.

4.4. Effect of size on deformation mechanisms

The main differences in deformation mechanisms are due to crystallographic orientation. However, some important changes happen when the pillar diameter gets smaller, which affects the mechanical response of the material. We observe that as the pillar diameter is reduced, there is less volume for dislocations emitted at the same time. In the case of the (100)-pillar, the largest pillar ($D = 400$ Å) emits dislocations from all four possible nucleation sites almost simultaneously, while in the case of $D = 200$ Å the loops are emitted one at a time. As the size becomes even

E_{ijk} (GPa)	$\dot{\varepsilon}$ (s^{-1})	Diameter (Å) 50	100	200	400	Pot. data	Exp. data
E_{100}	$5 \cdot 10^7$	122.7	122.7	119.8	118.6	135.1	143.0
	$5 \cdot 10^8$	125.0	123.1	126.1	134.6		
E_{110}	$5 \cdot 10^7$	240.4	228.3	227.9	229.5	223.5	233.6
	$5 \cdot 10^8$	240.6	227.8	222.8	244.5		
E_{111}	$5 \cdot 10^7$	307.7	306.4	297.8	300.6	285.8	296.2
	$5 \cdot 10^8$	306.7	307.3	297.3	319.4		

Table 1: Values of Young's moduli E_{ijk} for the different indenter planes (ijk), pillar diameters and strain rates $\dot{\varepsilon}$ simulated, found by linear fitting of the initial parts of the stress – strain curves. The last columns show values calculated from the elastic constants given in the potential data from [35] and experimental data from [42], respectively.

smaller, some nucleation sites never emit dislocations, and the loops that are emitted appear separately from each other. In Figure 9 pillars of $D = 400$ and 100 Å are put next to each other to highlight the size difference. Dislocations inside the pillars are shown, and we observe how four loops occur at the same time in the large pillar, while the small pillar only have room for one at a time. Similar quantitative trends are also seen in the other two orientations. This shows that larger the surface/volume ratio is, the harder it is to emit dislocation loops, and they are also created from fewer sites and at different times. Another feature of reducing the pillar diameter for (110) and (111) orientations is that the dislocation multiplication process, which is observed in the large pillars, vanish. There is not enough time or space for a multiplication to take place – the dislocation loops collide into each other or reach the opposite pillar surface too quickly.

4.5. Strain rate sensitivity

For the case of (110) pillars with a diameter of 100 Å, a total of four strain rates were investigated, and the resulting stress – strain curves are shown in Figure 11. There is a clear trend that the maximum stresses and strains are reduced as the strain rate slows down, see Figure 12. What we observe from both Figures 11 and 12 is that $\dot{\varepsilon} = 10^9$ s^{-1} appears to be a too high strain rate to use in simulations – it gives a rapid increase of stress at small strains, before continuing along a more linear curve on a stress level far above all the other simulation curves.

An exponential fitting $\sigma = A\dot{\varepsilon}^{\gamma}$ is done to the data points for the three slowest loading rates in Figure 12, and a value $\gamma = 0.03$ was found.

Of course, even though we have explored a range of strain rates, they are still far from experimental values, which can be typically be of order $\dot{\varepsilon} = 10^{-1} - 10^{-3}$ s^{-1} [16]. Despite this gap in strain rate values, we have shown a stable trend as the strain rate is changed, except for the extremely fast case of $\dot{\varepsilon} = 10^9$ s^{-1}.

5. Conclusions

By performing molecular dynamics simulations of nanopillar compression, we have shown the deformation mechanisms active when compressing on different crystallographic

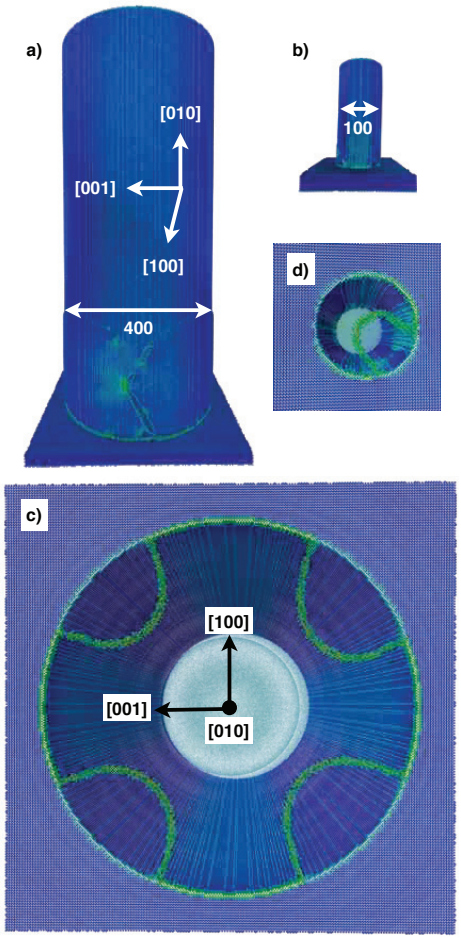

Figure 9: Size comparison of two (010)-pillars. a) and b) are the full pillars of diameter 400 and 100 Å, respectively, after some deformation has occurred. c) and d) show only atoms with high potential energy in order to see the dislocation loops, viewed from the bottom of the pillars for diameters 400 and 100 Å, respectively. All atoms are colored according to their von Mises stress. (Color online.)

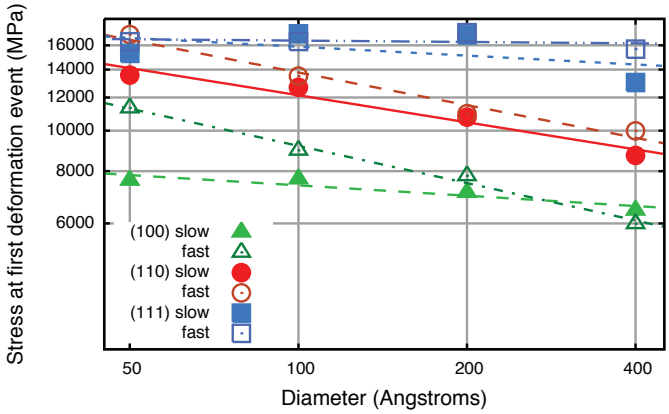

Figure 10: Stress at first deformation event plotted as a function of pillar diameter for the three orientations and two strain rates tested. Filled symbols correspond to "slow" loading, $\dot{\varepsilon} = 5 \cdot 10^7$ s^{-1}, and open symbols correspond to "fast" loading, $\dot{\varepsilon} = 5 \cdot 10^8$ s^{-1}. Lines are fitted power functions $\sigma_{\text{deform}} = \beta D^{-\alpha}$. Both axes are in log scale.

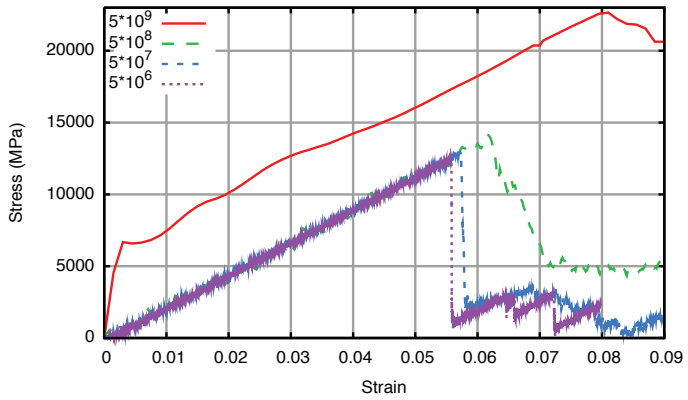

Figure 11: Stress – strain curves for the 100 Å diameter pillar compressed on the (110) plane, using strain rates varying from $5 \cdot 10^6 - 10^9$ s^{-1}.

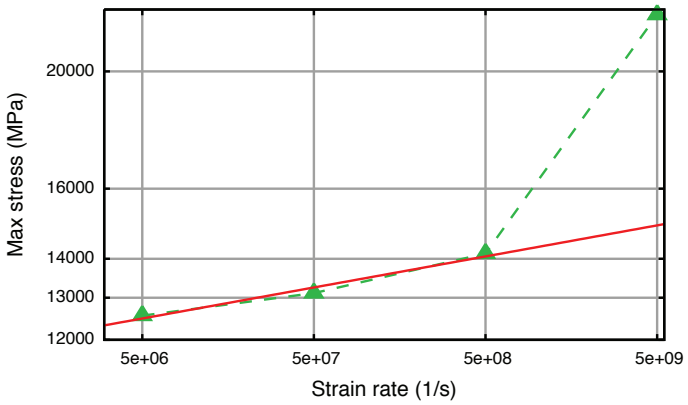

Figure 12: Maximum stress from the stress – strain curves plotted as a function of strain rate for (110) pillars of diameter 100 Å, and fitted power function for the three slowest strain rates. Both axes are in log scale.

planes in pure bcc iron. In addition, different pillar sizes and strain rates have been explored, and their influence on the maximum stress and the strain at which the pillars start deforming plastically.

The claim "smaller is stronger" holds for pillars compressed on {100} and {110} planes, while for {111} planes there is no clear strengthening trend when varying the pillar diameter. Larger pillar surface/volume ratios give less room for dislocations to be emitted in smaller pillars, and in addition the nucleation takes place from fever sites at different times.

By decreasing the strain rate, the maximum stress and the strain at the onset of plastic deformation in the pillar decrease.

Acknowledgements

We acknowledge the support from NTNU, the Research Council of Norway (Arctic Materials project supported through the Petromaks program, Contract No.187389/S30) and the industry consortium behind the Arctic Materials project. The support from NOTUR (Norwegian High Performance Computing) with the generous computation quota is highly acknowledged. Thanks to Alexander Stukowski for his work and support with the Ovito software, and thanks to Inga Vatne for help and discussions on dislocation mechanisms.

References

[1] S. Brinckmann, J.-Y. Kim, J. R. Greer, Fundamental differences in mechanical behavior between two types of crystals at the nanoscale, Physical Review Letters 100 (15) (2008) 155502. doi:10.1103/PhysRevLett.100.155502.

[2] B. R. S. Rogne, C. Thaulow, Investigation of nanomechanical test methods on arctic steels, in: Proceedings of the Twenty-first (2011) International Offshore and Polar Engineering Conference, International Society of Offshore and Polar Engineers (ISOPE), 2011, pp. 426–431.

[3] M. Dietiker, S. Buzzi, G. Pigozzi, J. Löffler, R. Spolenak, Deformation behavior of gold nano-pillars prepared by nanoimprinting and focused ion-beam milling, Acta Materialia 59 (5) (2011) 2180 – 2192. doi:10.1016/j.actamat.2010.12.019.

[4] S. M. Han, T. Bozorg-Grayeli, J. R. Groves, W. D. Nix, Size effects on strength and plasticity of vanadium nanopillars, Scripta Materialia 63 (12) (2010) 1153 – 1156. doi:10.1016/j.scriptamat.2010.08.011.

[5] H. Bei, S. Shim, E. George, M. Miller, E. Herbert, G. Pharr, Compressive strengths of molybdenum alloy micro-pillars prepared using a new technique, Scripta Materialia 57 (5) (2007) 397 – 400. doi:10.1016/j.scriptamat.2007.05.010.

[6] Q. Guo, J. R. Greer, Compressive properties of interface-containing Cu–Fe nano-pillars, Scripta Materialia 66 (5) (2012) 272 – 275. doi:10.1016/j.scriptamat.2011.11.008.

[7] J. R. Greer, W. C. Oliver, W. D. Nix, Size dependence of mechanical properties of gold at the micron scale in the absence of strain gradients, Acta Materialia 53 (6) (2005) 1821 – 1830. doi:10.1016/j.actamat.2004.12.031.

[8] J. R. Greer, W. D. Nix, Nanoscale gold pillars strengthened through dislocation starvation, Physical Review B 73 (2006) 245410. doi:10.1103/PhysRevB.73.245410.

[9] M. D. Uchic, D. M. Dimiduk, J. N. Florando, W. D. Nix, Sample dimensions influence strength and crystal plasticity, Science 305 (5686) (2004) 986–989. doi:10.1126/science.1098993.

[10] D. Dimiduk, M. Uchic, T. Parthasarathy, Size-affected single-slip behavior of pure nickel microcrystals, Acta Materialia 53 (15) (2005) 4065 – 4077. doi:10.1016/j.actamat.2005.05.023.

[11] C. A. Volkert, E. T. Lilleodden, Size effects in the deformation of sub-micron Au columns, Philosophical Magazine 86 (33-35) (2006) 5567–5579. doi:10.1080/14786430600567739.

[12] A. S. Schneider, D. Kaufmann, B. G. Clark, C. P. Frick, P. A. Gruber, R. Mönig, O. Kraft, E. Arzt, Correlation between critical temperature and strength of small-scale bcc pillars, Physical Review Letters 103 (10) (2009) 105501. doi:10.1103/PhysRevLett.103.105501.

[13] A. Schneider, B. Clark, C. Frick, P. Gruber, E. Arzt, Effect of orientation and loading rate on compression behavior of small-scale Mo pillars, Materials Science and Engineering: A 508 (1 - 2) (2009) 241 – 246. doi:10.1016/j.msea.2009.01.011.

[14] J.-Y. Kim, J. R. Greer, Size-dependent mechanical properties of molybdenum nanopillars, Applied Physics Letters 93 (10) (2008) 101916. doi:10.1063/1.2979684.

[15] L. Huang, Q.-J. Li, Z.-W. Shan, J. Li, J. Sun, E. Ma, A new regime for mechanical annealing and strong sample-size strengthening in body centred cubic molybdenum, Nature Communications 2. doi:10.1038/ncomms1557.

[16] A. T. Jennings, J. Li, J. R. Greer, Emergence of strain-rate sensitivity in Cu nanopillars: Transition from dislocation multiplication to dislocation nucleation, Acta Materialia 59 (14) (2011) 5627 – 5637. doi:10.1016/j.actamat.2011.05.038.

[17] T. Zhu, J. Li, A. Samanta, A. Leach, K. Gall, Temperature and strain-rate dependence of surface dislocation nucleation, Physical Review Letters 100 (2) (2008) 025502. doi:10.1103/PhysRevLett.100.025502.

[18] J. Brown, N. Ghoniem, Reversible-irreversible plasticity transition in twinned copper nanopillars, Acta Materialia 58 (3) (2010) 886 – 894. doi:10.1016/j.actamat.2009.10.003.

[19] F. Sansoz, Atomistic processes controlling flow stress scaling during compression of nanoscale face-centered-cubic crystals, Acta Materialia 59 (9) (2011) 3364 – 3372. doi:10.1016/j.actamat.2011.02.011.

[20] J. Senger, D. Weygand, P. Gumbsch, O. Kraft, Discrete dislocation simulations of the plasticity of micro-pillars under uniaxial loading, Scripta Materialia 58 (7) (2008) 587 – 590. doi:10.1016/j.scriptamat.2007.11.031.

[21] E. Rabkin, H.-S. Nam, D. Srolovitz, Atomistic simulation of the deformation of gold nanopillars, Acta Materialia 55 (6) (2007) 2085 – 2099. doi:10.1016/j.actamat.2006.10.058.

[22] A. Cao, E. Ma, Sample shape and temperature strongly influence the yield strength of metallic nanopillars, Acta Materialia 56 (17) (2008) 4816 – 4828. doi:10.1016/j.actamat.2008.05.044.

[23] Y. Gao, Z. Liu, X. You, Z. Zhuang, A hybrid multiscale computational framework of crystal plasticity at submicron scales, Computational Materials Science 49 (3) (2010) 672 – 681. doi:10.1016/j.commatsci.2010.06.010.

[24] C. Zhou, S. B. Biner, R. LeSar, Discrete dislocation dynamics simulations of plasticity at small scales, Acta Materialia 58 (5) (2010) 1565 – 1577. doi:10.1016/j.actamat.2009.11.001.

[25] L. A. Zepeda-Ruiz, B. Sadigh, J. Biener, A. M. Hodge, A. V. Hamza, Mechanical response of freestanding Au nanopillars under compression, Applied Physics Letters 91 (10) (2007) 101907. doi:10.1063/1.2778761.

[26] D. Weygand, M. Poignant, P. Gumbsch, O. Kraft, Three-dimensional dislocation dynamics simulation of the influence of sample size on the stress – strain behavior of fcc single-crystalline pillars, Materials Science and Engineering: A 483-484 (2008) 188 – 190. doi:10.1016/j.msea.2006.09.183.

[27] C. R. Weinberger, W. Cai, The stability of Lomer-Cottrell jogs in nanopillars, Scripta Materialia 64 (6) (2011) 529 – 532. doi:10.1016/j.scriptamat.2010.11.037.

[28] W. D. Nix, J. R. Greer, G. Feng, E. T. Lilleodden, Deformation at the nanometer and micrometer length scales: Effects of strain gradients and dislocation starvation, Thin Solid Films 515 (6) (2007) 3152 – 3157. doi:10.1016/j.tsf.2006.01.030.

[29] C. R. Weinberger, W. Cai, Surface-controlled dislocation

multiplication in metal micropillars, Proceedings of the National Academy of Sciences 105 (38) (2008) 14304–14307. doi:10.1073/pnas.0806118105.
[30] R. W. K. Honeycombe, The plastic deformation of metals, Edward Arnold (Publishers) Ltd., 1968.
[31] N. P. Allen, B. E. Hopkins, J. E. McLennan, The tensile properties of single crystals of high-purity iron at temperatures from 100 to -253 degrees C, Proceedings of the Royal Society of London. Series A, Mathematical and Physical Sciences 234 (1197) (1956) 221–246. doi:10.1098/rspa.1956.0029.
[32] W. Biggs, P. Pratt, The deformation and fracture of alpha-iron at low temperatures, Acta Metallurgica 6 (11) (1958) 694 – 703. doi:10.1016/0001-6160(58)90060-9.
[33] M. Lowry, D. Kiener, M. LeBlanc, C. Chisholm, J. Florando, J. Morris Jr., A. Minor, Achieving the ideal strength in annealed molybdenum nanopillars, Acta Materialia 58 (15) (2010) 5160 – 5167. doi:10.1016/j.actamat.2010.05.052.
[34] S. J. Plimpton, Fast parallel algorithms for short-range molecular dynamics, Journal of Computational Physics 117 (1995) 1–19.
[35] M. I. Mendelev, S. Han, D. J. Srolovitz, G. J. Ackland, D. Y. Sun, M. Asta, Development of new interatomic potentials appropriate for crystalline and liquid iron, Philosophical Magazine 83 (35) (2003) 3977–3994.
[36] S. L. Frederiksen, K. W. Jacobsen, Density functional theory studies of screw dislocation core structures in bcc metals, Philosophical Magazine 83 (3) (2003) 365–375. doi:10.1080/0141861021000034568.
[37] C. Domain, G. Monnet, Simulation of screw dislocation motion in iron by molecular dynamics simulations, Physical Review Letters 95 (21) (2005) 215506. doi:10.1103/PhysRevLett.95.215506.
[38] A. Stukowski, Visualization and analysis of atomistic simulation data with OVITO – the open visualization tool, Modelling and Simulation in Materials Science and Engineering 18 (1) (2010) 015012.
[39] J. D. Honeycutt, H. C. Andersen, Molecular dynamics study of melting and freezing of small Lennard-Jones clusters, The Journal of Physical Chemistry 91 (19) (1987) 4950–4963. doi:10.1021/j100303a014.
[40] H. Tsuzuki, P. S. Branicio, J. P. Rino, Structural characterization of deformed crystals by analysis of common atomic neighborhood, Computer Physics Communications 177 (6) (2007) 518 – 523. doi:10.1016/j.cpc.2007.05.018.
[41] A. Stukowski, K. Albe, Extracting dislocations and non-dislocation crystal defects from atomistic simulation data, Modelling and Simulation in Materials Science and Engineering 18 (8) (2010) 085001.
[42] J. A. Rayne, B. S. Chandrasekhar, Elastic constants of iron from 4.2 to 300°K, Physical Review 122 (6) (1961) 1714–1716. doi:10.1103/PhysRev.122.1714.
[43] J. Marian, W. Cai, V. V. Bulatov, Dynamic transitions from smooth to rough to twinning in dislocation motion, Nature Materials 3 (2004) 158–163. doi:10.1038/nmat1072.
[44] A. W. Sleeswyk, $\frac{1}{2}\langle 111\rangle$ screw dislocations and the nucleation of $\{112\}\langle 111\rangle$ twins in the B.C.C. lattice, Philosophical Magazine 8 (93). doi:10.1080/14786436308207311.
[45] K. Lagerlöf, On deformation twinning in b.c.c. metals, Acta Metallurgica et Materialia 41 (7) (1993) 2143 – 2151. doi:10.1016/0956-7151(93)90384-5.